UNIVERSIDADE ESTADUAL DE
CAMPINAS

Instituto de Física Gleb Wataghin

JOAO ULISES FABIÁN LIZÁRRAGA

Two problems on populations: speciation and self-organization

Dois problemas em populações: especiação e auto-organização

Campinas

2024

Joao Ulises Fabián Lizárraga

Two problems on populations: speciation and self-organization

Dois problemas em populações: especiação e auto-organização

Dissertation presented to the Institute of Physics Gleb Wataghin of the University of Campinas in partial fulfillment of the requirements for the degree of Master in Physics, in the area of Physics.

Dissertação apresentada ao Instituto de Física Gleb Wataghin da Universidade Estadual de Campinas como parte dos requisitos exigidos para a obtenção do título de Mestre em Física, na área de Física.

Supervisor: Marcus Aloizio Martinez de Aguiar

Este exemplar corresponde à versão final da Dissertação defendida pelo aluno Joao Ulises Fabián Lizárraga e orientado pelo Prof. Dr. Marcus Aloizio Martinez de Aguiar.

Campinas

2024

F112t   Fabián Lizárraga, Joao Ulises, 1996-
         Two problems on populations : speciation and self-organization / Joao Ulises Fabián Lizárraga. – Campinas, SP : [s.n.], 2024.

         Orientador: Marcus Aloizio Martinez de Aguiar.
         Dissertaçâo (mestrado) – Universidade Estadual de Campinas (UNICAMP), Instituto de Física Gleb Wataghin.

         1. Especiação. 2. Auto-organização. I. Aguiar, Marcus Aloizio Martinez de, 1960-. II. Universidade Estadual de Campinas (UNICAMP). Instituto de Física Gleb Wataghin. III. Título.

Informações Complementares

Título em outro idioma: Dois problemas nas populações : especiação e auto-organização
Palavras-chave em inglês:
Speciation
Self-organization
Área de concentração: Física
Titulação: Mestre em Física
Banca examinadora:
Marcus Aloizio Martinez de Aguiar [Orientador]
Thomas Kauê Dal'Maso Peron
Alberto Vazquez Saa
Data de defesa: 29-07-2024
Programa de Pós-Graduação: Física

Identificação e informações acadêmicas do(a) aluno(a)
- ORCID do autor: https://orcid.org/0000-0002-5408-7362
- Currículo Lattes do autor: http://lattes.cnpq.br/0535391330388748

MEMBROS DA COMISSÃO EXAMINADORA DA DISSERTAÇÃO DE MESTRADO DO ALUNO JOAO ULISES FABIÁN LIZÁRRAGA - RA 235643, APRESENTADA E APROVADA AO INSTITUTO DE FÍSICA GLEB WATAGHIN, DA UNIVERSIDADE ESTADUAL DE CAMPINAS, EM 29/07/2024.

COMISSÃO JULGADORA:

- Prof. Dr. Marcus Aloizio Martinez de Aguiar – Presidente e Orientador (IFGW/ UNICAMP)

- Prof. Dr. Thomas Kauê Dal'Maso Peron (Instituto de Ciências Matemáticas e de Computação - USP)

- Prof. Dr. Alberto Vazquez Saa (IMECC/ UNICAMP)

OBS.: Ata da defesa com as respectivas assinaturas dos membros encontra-se no SIGA/Sistema de Fluxo de Dissertação/Tese e na Secretaria do Programa da Unidade.

CAMPINAS

2024

Acknowledgements

Abstract

Populations can show emergent behaviors under specific conditions. From short to long scales, in space or time, patterns emerge as individuals' states evolve following simple rules. In this work, we explore two of these behaviors: speciation and self-organization. For the former, we consider the evolution of neutral populations in sympatric scenarios under a mating condition imposed by assortativity. In our model, individuals are represented by three chromosomes: one responsible for reproductive compatibility, one for coding the trait on which assortativity will operate, and a neutral chromosome. Reproduction is possible if individuals are genetically similar concerning the first chromosome, but among these compatible mating partners, the one with the most similar trait coded by the second chromosome is selected. We show that speciation with small genome sizes can occur if assortative mating is introduced. Moreover, this type of assortativity facilitates speciation, which can happen with a small number of genes in the first chromosome. For the latter, we study populations of hypothetical individuals where swarming and synchronization can arise and where these phenomena can also interplay. We present two analytically tractable models and explore the static and active states that emerge from these. All the regions where these states emerge are uncovered and classified. Additionally, uncommon features such as multistability and chaos, found in these models, are also studied.

Resumo

Populações podem apresentar comportamentos emergentes sob condições específicas. Em escalas curtas ou longas, no espaço ou no tempo, padrões emergem à medida que os estados dos indivíduos evoluem seguindo regras simples. Neste trabalho, exploramos dois desses comportamentos: especiação e auto-organização. Para o primeiro, consideramos a evolução de populações neutras em cenários simpátricos sob uma condição de acasalamento imposta pela assortatividade. Em nosso modelo, os indivíduos são representados por três cromossomos: um responsável pela compatibilidade reprodutiva, outro para codificar o traço sobre o qual a assortatividade atuará, e um cromossomo neutro. A reprodução é possível se os indivíduos forem geneticamente semelhantes em relação ao primeiro cromossomo, mas, entre esses parceiros compatíveis para acasalamento, é selecionado aquele com o traço mais semelhante codificado pelo segundo cromossomo. Mostramos que a especiação com pequenos tamanhos de genoma pode ocorrer se o acasalamento assortativo for introduzido. Além disso, esse tipo de assortatividade facilita a especiação, que pode ocorrer com um pequeno número de genes no primeiro cromossomo. Para o segundo comportamento, estudamos populações de indivíduos hipotéticos onde o agrupamento e a sincronização podem surgir e onde esses fenômenos também podem interagir. Apresentamos dois modelos analiticamente tratáveis e exploramos os estados estáticos e ativos que emergem desses modelos. Todas as regiões onde esses estados emergem são descobertas e classificadas. Além disso, características incomuns, como multiestabilidade e caos, encontradas nesses modelos, também são estudadas.

Contents

Introduction

Individuals, whether natural or artificial, can exhibit the emergence of several behaviors after engaging in specific processes. These manifestations, observed in time and space, can be found at different scales, ranging from populations splitting into species after thousands of generations, through murmurations of starlings forming in minutes while confined to localized regions, to the self-organization of sperm occurring at a micrometric scale. Despite the notable differences between these systems, some of the emergent phenomena undergone by their populations are qualitatively well understood. Yet, an explanation of the mechanisms behind these still lacks quantitative approaches.

Speciation, firstly, describes how a group of sexually compatible individuals splits into multiple sexually isolated ones. The process itself has been questioned and documented since the works by Charles Darwin, including his masterpiece *On the Origin of Species by Means of Natural Selection* [1, 2]. However, understanding the detailed mechanisms that lead to reproductive isolation, and therefore to speciation, is still an open problem in evolutionary biology [3]. One of the difficulties in promoting speciation in sexually reproducing populations is the constant gene flow between individuals, promoted by recombination [4]. This tends to homogenize the genetic information among all members of the population, hindering the appearance of genetically distinct groups. Gene flow can be interrupted if the population is split into two or more groups by geographical barriers. If the groups are kept isolated long enough, genetic differences will appear because of mutations, leading eventually to reproductive isolation. This is called *allopatric speciation* and is one of the most accepted mechanisms for the origin of new species. At the other extreme from geographic isolation, there is the possibility of speciation with random mating, where species emerge from a population while coexisting in the same geographic area [2], called *sympatric speciation.*

Self-organization, on the other hand, is an emergent phenomenon where ordered patterns manifest as a result of the interaction between individuals [5, 6]. Within this framework, the most evident formations happen in space. However, individuals can also self-organize in time. The spatial self-organization is called swarming and has been spotted in natural systems such as birds [7], fishes [8], and ants [9]. Studies on swarming started with computational models based on simple rules such as maintaining closeness between individuals and avoiding collisions [10]. However, the first theoretically meaningful model was introduced by Vicsek [11], which, despite its limitations, became a landmark in studying behaviors of this nature. Subsequent works, as celebrated as the Vicsek model, are those proposed by Cucker and Smale [12, 13], and Toner and Tu [14]. Another type of self-organization is that of synchronization, which occurs among individuals' internal

periodic degrees of freedom. Some examples include the flashing of fireflies [15], the clapping of a crowd [16], and the bursting of neurons [17]. Conversely to swarming, synchronization has been studied long before. One of the first models was presented by Winfree in his effort to study biological rhythms [18]. Then, Kuramoto introduced a simpler and solvable alternative to Winfree's model, which became the most famous in the field [19–21]. Given its manageability, Kuramoto's has been widely used to study synchronization in several natural systems [22]. Both self-organization categories have been widely studied independently or associated in some ways.

Here, we tackle both problems described above: speciation and self-organization. Specifically, we focus on the emergence of species in a sympatric setup and the role of assortativity in it. Likewise, we examine the emergence of self-organization in space and time of phase oscillators. We use numerical and analytical tools to understand mechanisms that drive the emergence of each phenomenon as well as their equilibrium states and associated effects.

1 Sympatric speciation and assortativity

Speciation results from the interplay of different isolating mechanisms [3, 23], such as geographic isolation [24–27], genetic incompatibilities [28], competition for resources [29–31], and temporal separation [32, 33]. Ultimately, speciation is the result of significant decrease in gene flow between groups of individuals, allowing adaptations and random changes occurring in each group to be restricted to that group. When this happens, genetic and phenotypic differences can accumulate over time, leading to reproductive isolation and possibly to hybrid incompatibility. Assortative mating has been conjectured to reinforce the speciation process by preventing individuals with different phenotypes to mate when they come into contact. Assortative mating occurs when individuals with similar phenotypes mate more often than would be expected at random. Frequent mating of dissimilar individuals would mix their genomes, eventually leading to the reversion of speciation. Evidence demonstrating the role of assortative mating in different cases has accumulated [34–36], although it might be inneffective in hybrid zones [37].

In this work we investigate the role of assortativity in a simple model of speciation. For that, we focus on sympatric speciation, i.e., the development of reproductive isolation without geographic barriers. In this case, mating is not restricted by the presence of physical barriers or by spatial proximity of individuals, but it cannot be completely random either, otherwise no reduction in gene flow can occur. Sympatric speciation, therefore, requires some form mating selection [23], such as that promoted by temporal isolation [38], genetic incompatibilities [39] or assortative mating based on phenotypic characters [36, 40–42]. Empirical evidence for sympatric speciation is reviewed in [43]. Here we explore a model of sympatric speciation driven be genetic incompatibilities and assortative mating.

From a theoretical point of view two models of sympatric speciation have stood out. The first, proposed by Dieckmann & Doebeli [29] argues that strong competition for resources could drive speciation even without any form of geographic isolation. If resources are characterized by a continuous parameter, such as seed size, the theory suggests that it might be more advantageous for individuals who have phenotypes adapted to consume extreme resources (such as very small or very large seeds, of which there are fewer) than it is for those with a more common phenotype – for which there are abundant resources but also strong competition – resulting in a disruptive selection. In this case two stable groups would emerge, adapted to the extremes of the resource distribution, whereas intermediate phenotypes would have lower fitness. The model has been criticized for requiring unrealistic high mutation rates [31].

The second theoretical model, proposed by Higgs & Derrida [44–47] (DH model), demonstrated that, even without competition, sympatric speciation may still occur if mating is restricted by genetic similarity. The model is based on the idea that genetic differences create incompatibilities between individuals and, if the number of such differences is too large, mating would not happen. The model considers hermaphrodite individuals whose genomes are described by binary chains of biallelic genes. Mating occurs only between individuals whose genetic similarity is large enough – i.e. based on prezygotic barriers. Speciation, however, only happens if the number of genes responsible for creating these incompatibilities is sufficiently large, of the order of thousands of genes, depending on the model parameters [48]. The original model considered only infinitely large genomes to avoid this limitation.

The need for very large genomes in the DH model can be circumvented by adding auxiliary mechanisms that contribute to further reduce gene flow among the individuals. One possibility is to introduce space and restrict mating not only by genetic similarity but also by spatial proximity [47, 48]. This facilitates speciation and drastically reduces the number of genes required for the formation of reproductively isolated groups. Speciation, however, is now *parapatric*, as there is isolation by distance, a weak form of geographic isolation.

Here we reexamine the DH model with finite genomes and consider the effects of assortative mating in facilitating speciation. Assortative mating has been observed in many species, especially with respect to body size, pheromones and coloration [49], and it can be a powerful driver of speciation. For instance, Puebla et al 2012 [50] found that the pairing dynamics of hermaphrodite fish of the genus *Hypoplectrus* is related to color patterns that is used as an indicator to release sperm and eggs into the water. In order to introduce assortative mating in the DH model, we split the genomes into three independent chromosomes. This division in chromosomes serves solely to identify genes that have similar roles. They differ from real chromosomes in the sense they are not physically linked during reproduction. We then have, one responsible for creating reproductive incompatibilities as in the original model, one for coding the trait on which assortativity will operate, and one neutral chromosome coding for a second trait which is not under selection by assortativity and is not responsible for reproductive incompatibilities. In this way, reproduction is possible only if individuals are genetically similar with respect to the first chromosome, but among these compatible mating partners, the one with the most similar assortativity chromosome will be chosen. We show that: (i) assortativity has a dramatic effect on speciation, greatly facilitating the process; (ii) species, classified according to reproductive isolation dictated by the first chromosome, can display different traits values, as measured by the second and the third chromosomes; (iii) this implies that species identification based on similarity of the assortativity trait or the neutral trait generally coincides with that based on reproductive isolation.

2 The Derrida-Higgs models

Derrida and Higgs proposed three models to describe the evolution of finite populations with different forms of reproduction: (i) asexual; (ii) sexual with random mating; (iii) sexual with mating constrained by genetic similarity [44, 45]. In all cases the individuals were considered hermaphrodite and haploid, with genomes represented by a single chromosome $\mathbb{S}$:

$$\mathbb{S}_F^\alpha : \{S_1^\alpha, S_2^\alpha, S_3^\alpha, \ldots, S_F^\alpha\}. \tag{2.1}$$

Here α labels the individual, F is the number of *loci* and S_i^α represents a biallelic gene at locus i, which can take the values ± 1. Gene and allele are interchangeable nomenclatures here because we are considering each *locus* as a gene and because individuals are haploid, the allele of a given gene is representing the gene itself. In the DH models the authors consider the limit $F \to \infty$, as this simplifies the simulations and the dynamics, allowing the derivation of several analytical results.

The population is characterized by a matrix $d_F^{\alpha\beta}$ containing the normalized genetic distance between all pairs of individuals α and β:

$$d_F^{\alpha\beta} = \frac{1}{F} \sum_{i=1}^{F} |S_i^\alpha - S_i^\beta|. \tag{2.2}$$

The population can also be characterized by the genetic similarity [45]

$$q_F^{\alpha\beta} = \frac{1}{F} \sum_{i=1}^{F} S_i^\alpha S_i^\beta \tag{2.3}$$

which is related to the genetic distance by

$$q_F^{\alpha\beta} = 1 - d_F^{\alpha\beta} \tag{2.4}$$

with $0 < d_F^{\alpha\beta} < 2$ and $-1 < q_F^{\alpha\beta} < 1$.

Initially, all individuals have identical genomes, with $S_i^\alpha = 1$. The evolution of a population with M individuals is performed as follows:

(i) asexual model: an individual is randomly chosen from the population to reproduce; an offspring is created, receiving an exact copy of its parent's genome;

(ii) sexual model with random mating: two individuals are randomly chosen from the population to reproduce; an offspring is created by recombining the genomes of the parents, such that the allele for each gene is received from either parent with equal probability;

(iii) sexual model with mating restriction: a first parent α is randomly chosen from the population; a second parent β is then randomly selected; if $d_F^{\alpha\beta} \leqslant g$, an offspring is created by recombining the genomes of the parents as in (ii). If $d_F^{\alpha\beta} > g$ another second parent is selected from the population. If after M trials no compatible parents can be found, the first parent is discarded and a new one is chosen, repeating the search for a compatible mate until an offspring is produced. The parameter $0 < g < F$ sets the maximum genetic distance for reproductive compatibility.

In all cases the individuals are selected with replacement, so that the same individual can be selected more than once. Also, after the offspring has been created, each of its genes is allowed to mutate with rate μ and the whole process is repeated until M offspring are created, forming the next generation.

The evolution of genetic distances between individuals can be computed considering the relationship between parents and their offspring. Consider the case of sexual reproduction: suppose $P_1(\alpha)$ and $P_2(\alpha)$ are the parents of individual α and $P_1(\beta)$ and $P_2(\beta)$ are the parents of β. If μ is the mutation rate, the probability of mutation in a unit time step (one generation) is $(1 - e^{-2\mu})/2$ and the probability that a mutation does not happen is $(1 + e^{-2\mu})/2$. If gene S_i^α is inherited from $P_1(\alpha)$, then:

$$\mathbb{P}(S_i^\alpha = S_i^{P_1(\alpha)}) = \frac{1}{2}(1 + e^{-2\mu}),$$

$$\mathbb{P}(S_i^\alpha = -S_i^{P_1(\alpha)}) = \frac{1}{2}(1 - e^{-2\mu}),$$

are the probabilities of keeping the allele of $P_1(\alpha)$ or mutating, respectively. The expected value is $E(S_i^\alpha) = e^{-2\mu}S_i^{P_1(\alpha)}$. Since the gene is inherited from either parent with equal probability, $E(S_i^\alpha) = e^{-2\mu}(S_i^{P_1(\alpha)} + S_i^{P_2(\alpha)})/2$. From Eq. (2.3) we find, for independent genes,

$$E(q^{\alpha\beta}) = \frac{e^{-4\mu}}{4}(q^{P_1(\alpha)P_1(\beta)} + q^{P_2(\alpha)P_1(\beta)} + q^{P_2(\alpha)P_1(\beta)} + q^{P_2(\alpha)P_2(\beta)}). \qquad (2.5)$$

In the limit $F \to \infty$ the expected similarity value coincides with the realized one. For finite genomes this is only an approximation. In terms of genetic distances, using Eq. (2.4), we find

$$d^{\alpha\beta} = 1 - e^{-4\mu} + \frac{e^{-4\mu}}{4}(d^{P_1(\alpha)P_1(\beta)} + d^{P_2(\alpha)P_1(\beta)} + d^{P_2(\alpha)P_1(\beta)} + d^{P_2(\alpha)P_2(\beta)}) \qquad (2.6)$$

where we have dropped the expectation symbol. In the asexual case, since the offspring comes from a single parent, we obtain $E(q^{\alpha\beta}) = e^{-4\mu}q^{P(\alpha)P(\beta)}$.

In [44] it is shown that the average genetic distance converges to the asymptotic value

$$d_0 \approx \frac{1}{1 + (4M\mu)^{-1}},$$

where the approximation holds for large M and small μ. Although this result works both for the asexual and sexual cases, the distribution of genetic distances is very different in each case, as illustrated in Fig. 1 for $M = 500$ individuals, $F = 10,000$ loci and mutation rate $\mu = 10^{-3}$. In all cases the distribution starts as a single peak at $d = 0$ in $t = 0$. For $t > 0$ the peak broadens and moves towards $d = 1$ as genomes accumulate mutations. For asexual reproduction, Fig. 1(a), the distribution breaks into several peaks representing pairs of similar genomes, or strains (peaks close to $d = 0$), pairs of genomes that are very different from each other (peaks close to $d = 1$). For the random mating sexual model, on the other hand, the distribution converges to a single peak around d_0, showing that the population does not break into clusters of similar genomes and peaks of very different genomes, suggesting the existence of a single species. Fig. 1(c) shows the distribution of genetic distances for the sexual model with mating restriction for $g = 0.05$. In this case the distribution does break into peaks, similar to the asexual model. In order to understand the population structure, it is important to introduce an appropriate concept of species for these models.

Species definition: in the context of the models discussed in this work, species are defined by reproductive mating affinity and are best visualized in terms of the *compatibility network*, which can be understood as the possible genetic flow network, as shown in Fig. 1(d). In the network, nodes represent individuals and links are drawn between sexually compatible individuals, satisfying $d \leqslant g$. Species are then the components of the resulting network. Notice that components are not necessarily fully connected, implying that within species there might be sexually incompatible individuals that are indirectly connected by other members of the species via gene flow.

The peaks in the distribution of genetic distances in Fig. 1(c) are, therefore, the result of speciation. The species at time T=1,000 are shown in Fig.1(d) for the sexual model. In this case, as time passes, the distribution moves to the right and reaches $d = g$, meaning that the population breaks into species because individuals with $d > g$ cannot mate. Peaks in the region $d < g$ represent clusters of compatible individuals, therefore belonging to the same species. Peaks with $d > g$ represent genetic distances between individuals in different species.

Two important features of the sexual model with mating restriction are: (i) in the limit $F \to \infty$ the condition $g < d_0$ is necessary and sufficient for speciation; (ii) for finite F there is a threshold F_c below which speciation does not occur even if $g < d_0$. For $F < F_c$ the distribution of genetic distances behaves similarly to the random mating model, but it equilibrates at $d = g$ instead of $d = d_0$ [48]. For the parameters of Fig. 1 we find $F_c \approx 4,000$ loci.
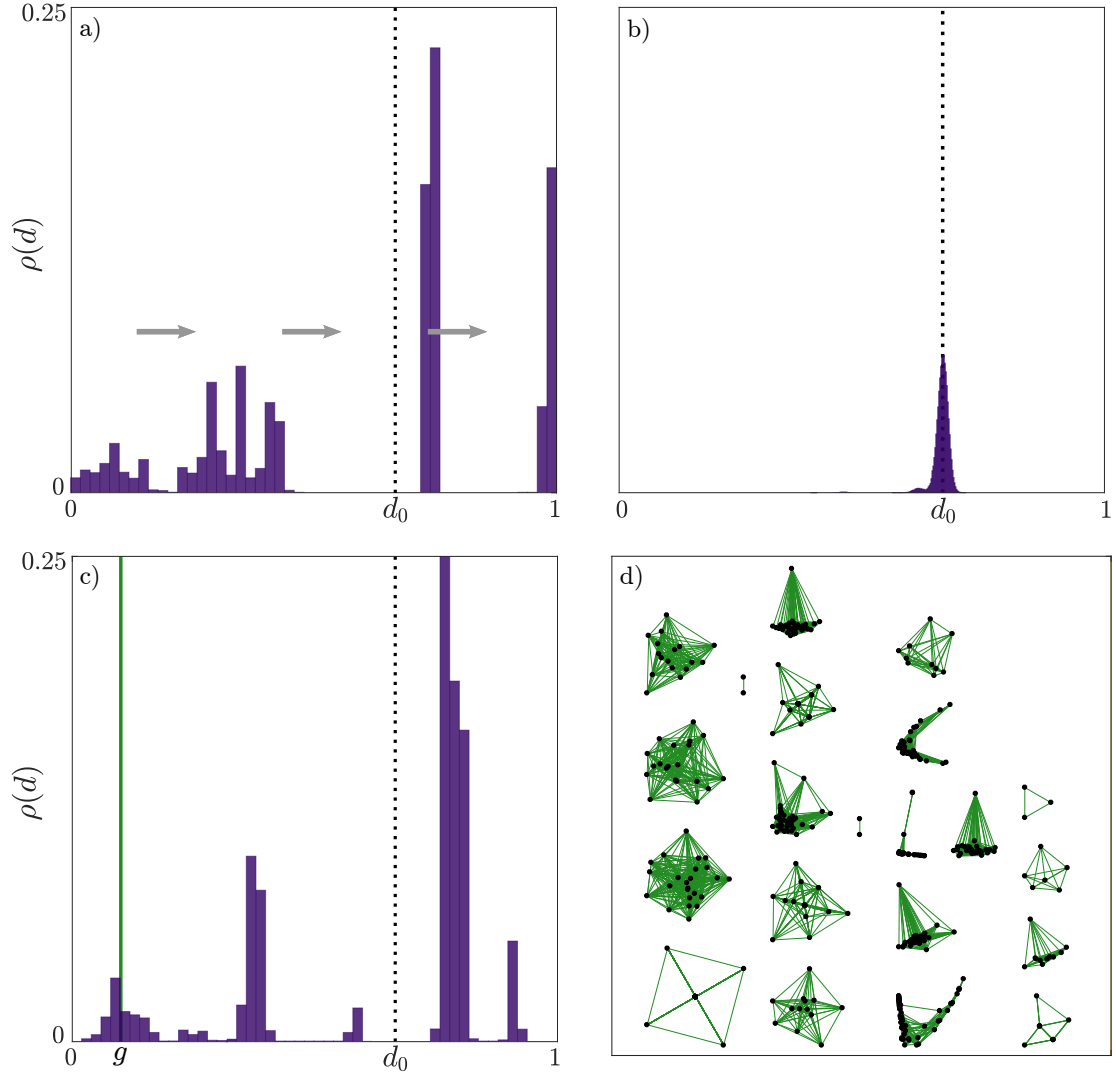
Figure 1 – Genetic distance distributions in the (a) asexual, (b) sexual with random mating, and (c) sexual with mating restriction cases of the DH models at $T = 1000$. Simulations were performed for $M = 500$, $F = 10,000$, and $\mu = 10^{-3}$. In (a), arrows represent drifting of the distribution towards 1. Dotted lines are positioned at the expected mean distance d_0. The distance threshold in the species-formation model was set at $g = 0.05$. Panel (d) show species representation in terms of components of the compatibility network, corresponding to the distribution shown in (c).

3 The three-chromosome assortativity model

To generalize the genetic structure of the individuals and include assortative mating, we extend the genetic model from one to three chromosomes. Each chromosome plays a different role which we named compatibility, assortativity, and neutral, composed by C, A, and, N *loci*, respectively. We call them chromosomes because of their role, but they could be represented in as a single set of genes since all of them are independently passed to the offsprings. Each of these chromosomes can be defined as in (2.1), changing the length F to the respective length C, A, or N. Then, we can define the full genome of an individual α, composed by $F = C + A + N$ loci, as the concatenation

$$\mathbb{S}^{F,\alpha} : \{\mathbb{S}^{A,\alpha}, \mathbb{S}^{N,\alpha}, \mathbb{S}^{C,\alpha}\}. \tag{3.1}$$

We name the model as "three chromosome assortativity Derrida-Higgs" model, or 3CADH for short. The DH models are recovered from the 3CADH by making $A = N = 0$. The genetic distance between two individuals can also be calculated with respect to each chromosome separately, adapting Eq. (2.2) to the respective chromosome length.

Evolution with assortativity is implemented in the sexual version of the model as follows:

1. a first parent α is drawn at random for reproduction;

2. the subset of individuals $\mathcal{C}$ compatible with α is selected, considering only the genetic distance between the compatibility chromosomes, i.e., satisfying the condition $d_C^{\alpha\beta} \leqslant g_C$;

3. from the set $\mathcal{C}$, potential mating partners are selected by genetic similarity in the assortative chromosome. They must satisfy the condition $d_A^{\alpha\gamma} \leqslant \delta_A^\alpha + r$ where δ_A^α is the minimum distance $d_A^{\alpha\gamma}$ between α and all individuals $\gamma \in \mathcal{C}$ and r is the choosiness parameter, measured as a fraction of the A. Among these individuals one is randomly selected for mating. Strict assortativity corresponds to $r = 0$ (mating with the most similar) whereas less stringent assortativity is obtained with $r > 0$.

A schematic summary of the 3CADH model is shown in Figure 2. Since mating compatibility between individuals in the 3CADH model concerns only the compatibility chromosome, we use such a condition to define reproductively isolated species. Genetic distance thresholds for the neutral (g_N), assortative (g_A) and full genome (g_F) can also be defined, although they have no effect in the mating dynamics and, therefore, on evolution. These thresholds can be used to group individuals according to the assortative, neutral
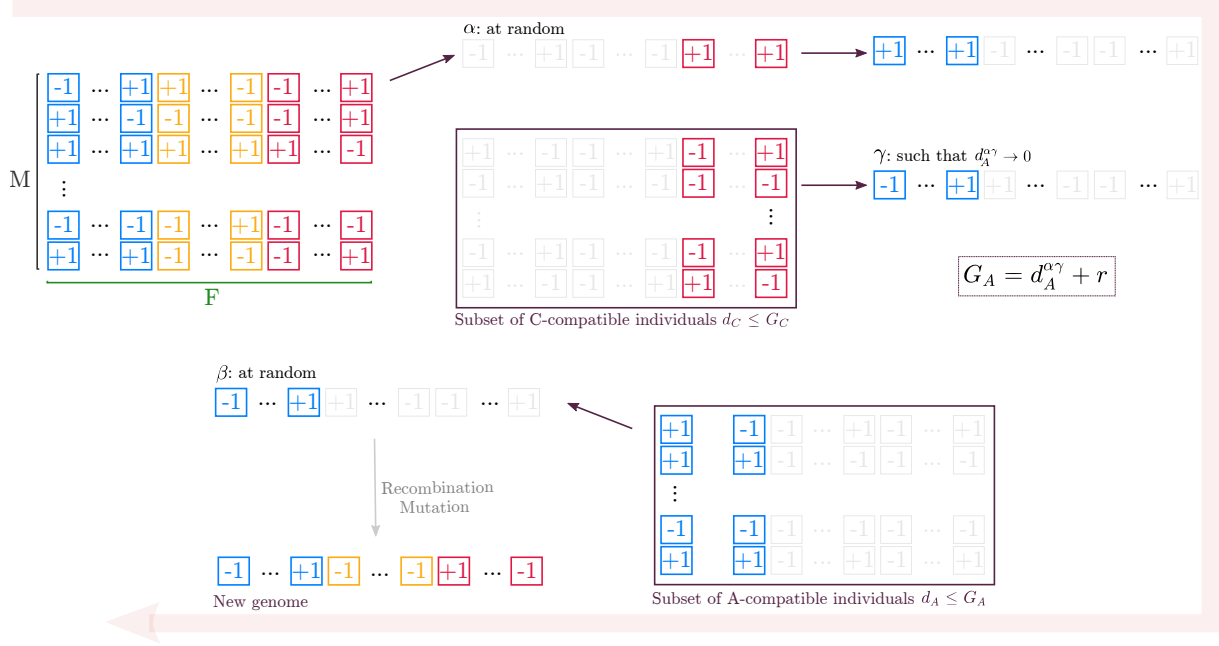
Figure 2 – Population evolution in the 3CADH model. From the population at generation t (top-left), an individual α is chosen at random for reproduction. Individuals sexually compatible with α are then arranged in a subset $\mathcal{C}$ (top-middle). We compute δ_A^α as the minimum distance $d_A^{\alpha\gamma}$, with respect to the assortativity chromosome, between α and all individuals $\gamma \in \mathcal{C}$. The potential mates of α are contained in another subset $\mathcal{M}$ such that $d_A^{\alpha\gamma} \leqslant \delta_A^\alpha + r$ where r is the choosiness parameter. Strict assortativity corresponds to $r = 0$. A mating partner β is chosen from $\mathcal{M}$ at random (bottom-left). An offspring is created for generation $t + 1$ by recombining all chromosomes of α and β and allowing their genes to mutate. The process is repeated until M offspring are created.

and full set of traits and to describe correlations between the three chromosomes and their evolution through generations. A key feature of the 3CADH model is that the minimum number of loci in the C chromosome necessary to induce speciation drops drastically when assortativity is taken into account. A summary of the parameters used in the 3CADH model is shown in Table 1.

3.1 The power of assortativity and the hitchhiking effect

In this section we show numerical simulations of the 3CADH model for different chromosome sizes, focusing on how strict assortativity ($r = 0$) facilitates speciation in a sympatric scenario. In all cases we keep the total number of genes $F = C + A + N$ fixed and change only the proportion of genes in each chromosome in the genetic architecture of the individuals.

As the population evolves, mutations are accumulated and transmitted to offspring via reproduction. Depending on the model parameters, the population may split

		Description	Color
M		Number of individuals	
μ		Mutation rate	
F		Full genome	Green
C	Number of genes	Compatibility chromosome	Crimson
A		Assortative chromosome	Azure
N		Neutral chromosome	Naples
d_γ	Genetic distance (2.2)	Full genome d_F Compatibility chromosome d_C Assortative chromosome d_A Neutral chromosome d_N	
g_γ	Clustering threshold	Full genome g_F Compatibility chromosome g_C Assortative chromosome g_A Neutral chromosome g_N	

Table 1 – Summary and description of parameters used in the models. Colors are used to differentiate between chromosomes along the simulations.

into species. For the original DH model with sexual reproduction and mating restriction ($A = N = 0$), species appear only if $F > 4,000$ (for a population size of $M = 500$ and a mutation rate of $\mu = 10^{-3}$). In our simulations we fixed $F = 2,500$ to prevent speciation in the original DH models and force the process to be fully dependent on assortativity. We also fixed the population size to $M = 500$, mutation rate $\mu = 10^{-3}$ and evolved the population for $T = 500$ generations, which is enough to observe equilibrium in species richness in all cases studied. The initial population is homogeneous, consisting of M identical individuals, with all genes set to +1. A common criticism to sympatric speciation modeling is the abnormal high mutation rate required for species to form. In the presented model, a lower mutation rate could still split the population into clusters (here called species), however the simulation cost would be very large [51].

The classification of individuals into clusters of similar traits can be performed for each chromosome separately and for the full genome. Classification with respect to the compatibility chromosome results in species; clusters classified according to the assortativity and neutral chromosome will be termed *A-clusters* and *N-clusters* respectively. As the population evolves, the number of clusters formed by similar individuals changes and allows us to see transitions associated to each chromosome type. Starting from a single cluster formed by the M, in this case 500, initially identical individuals, the average number of clusters evolves and reaches a plateau. In a single simulation, oscillations with considerable amplitude are observed, but the average over many simulations shows a smooth behavior. In Fig. 4, we show how the number of clusters evolve for an extreme case where assortativity and compatibility chromosome sizes are $A = C = 100$, i.e., only 4% of the full genome as in Fig. 3(b). Notice that the size of the compatibility chromosome
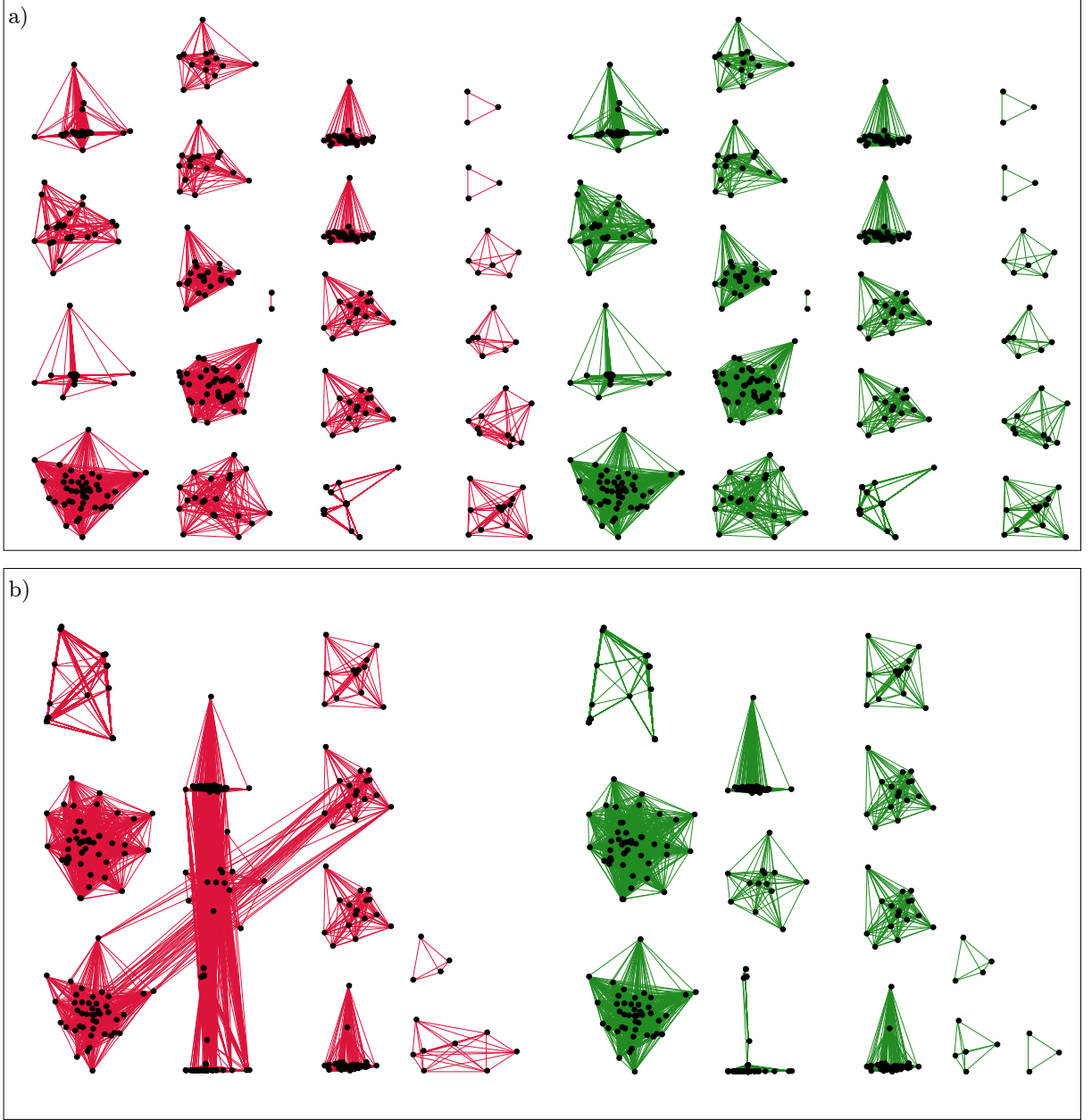
Figure 3 – Clustering from two populations evolved using the 3CADH model. Nodes represent individuals while links between them represent the fulfillment of $d_F \leqslant G_F$ (left), or $d_C \leqslant G_C$ (right). The two panels show networks at $T = 500$ for $M = 500$, $F = 2500$, and $\mu = 10^{-3}$. In a), species emerge using $C = 1500$ and $A = 1000$; and in b), $C = 100$, and $A = 100$. In both cases, the compatibility threshold is set at $G_C = 0.05C$.

is very small compared with the minimum size 4,000 needed for speciation to occur in the original DH model, showing the power of assortativity in promoting speciation in a sympatric scenario.

We used the same proportion of chromosome size to set the thresholds: $g_N = g_C = g_F = 0.05$. For assortativity, however, we set the threshold $g_A = 0.01$ so as to have the same behavior and similar scale of *A-clusters* as obtained by *C-clusters* (real species).

Figure 4 – Evolution of the number of clusters emerged using the 3CADH model. Simulations were performed along $T = 500$ generations for $F = 2500$, $A = 100$, $C = 100$, and $\mu = 10^{-3}$. In a), b), c), and d), bold lines represent the average of 100 executions of the model while shadows around them represent the dispersions. In e) all the average curves are put together.
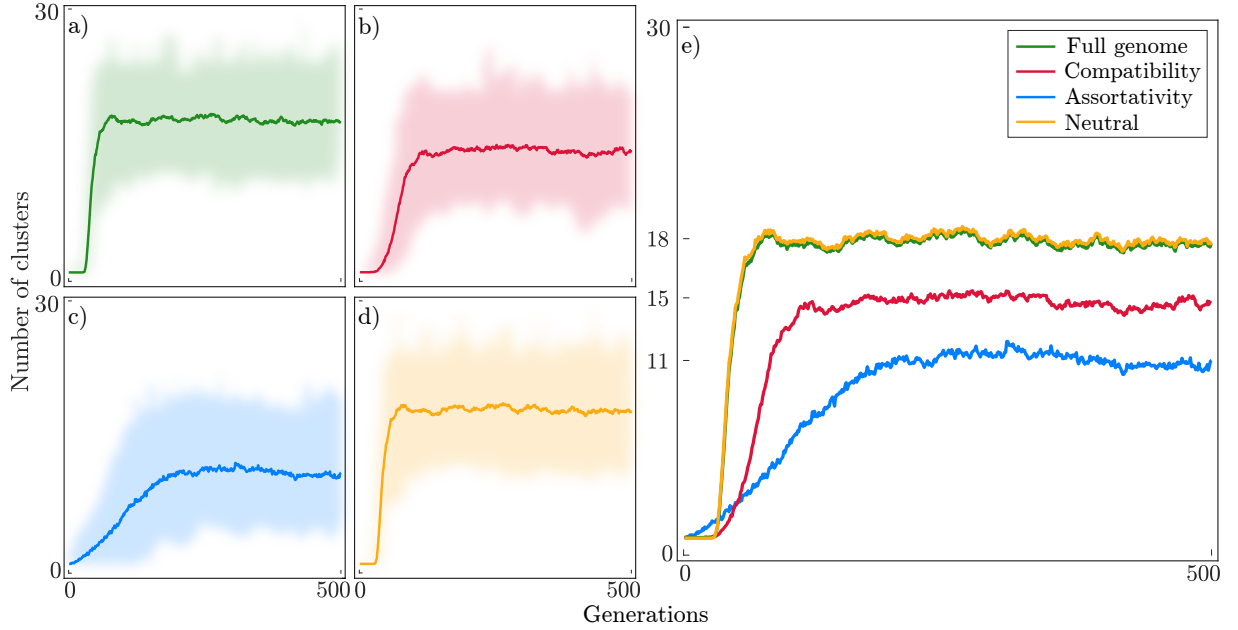
As shown in Figs. 4a, 4b, 4c, and 4d, the average number of clusters segregated according to each chromosome converges towards a fixed number, and as a byproduct, that of the full genome also does. Note that, from Fig. 4e, the behavior of the number of species works as a predictor for the behavior of the full genome, even for small compatibility chromosome sizes. Therefore, the neutral genes, which make up most of the genome in these simulations, follow the behavior of the parts under selection, in a sort of hitchhiking effect. Classifying species by the neutral trait would provide results very similar to the 'true' classification by reproductive isolation. Thus, neutral traits can work as proxies for reproductive isolation and, therefore, for species identification. The assortativity chromosome can also be used for species identification, although with less accuracy, as the predicted number of species depends more critically on g_A.

3.2 Species identification

Figure 4 suggests that genetic distances associated to all chromosomes are correlated. Indeed, once species form, reproduction is restricted to occur among members of each species, interrupting gene flow between species. As genomes of individuals belonging to different species become independent, they drift away from each other, whereas those of the same species keep mixing by reproduction, retaining some similarity. Since this argument holds for the entire genome, the similarity imposed by the mating restriction
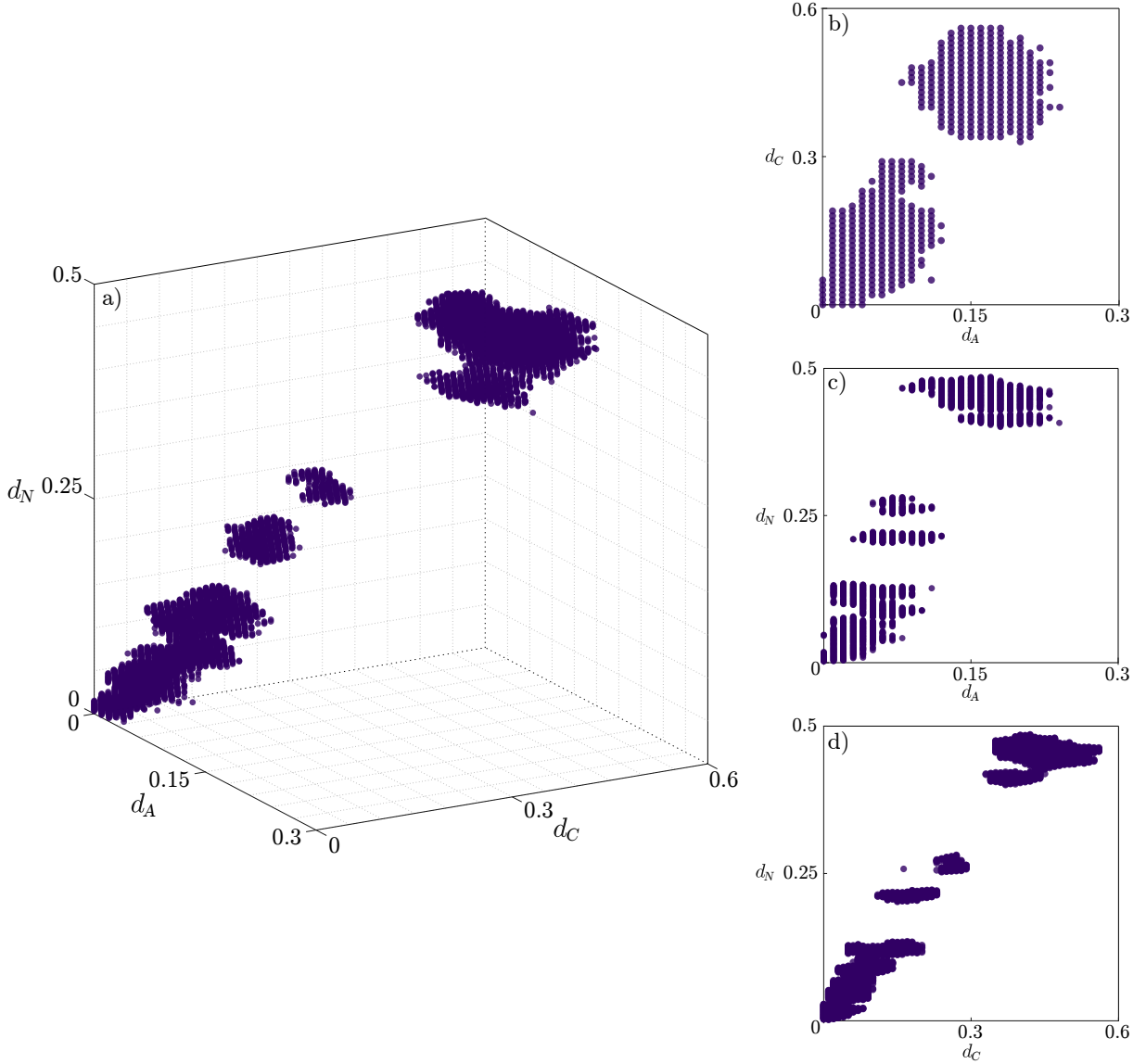
Figure 5 – Genetic distance correlation between chromosomes of each individual at $T = 500$. Simulations of the 3CADH model were performed for $F = 2500$, $A = 100$, $C = 100$, and $\mu = 10^{-3}$. Circles are positioned at the genetic distance between respective chromosomes of each pair of individuals in a) a three-dimensional box and in b), c), and d) projections in two-dimensions.

on the compatibility chromosome spreads to the assortativity and neutral chromosomes. Fig. 5 shows that genetic distances between pairs of individuals for each chromosome are actually linearly correlated. The clusters observed in this figure, that look like steam coming out of a kettle, are similar to the peaks in the histograms shown in Fig. 1. Points close to the origin represent pairs of similar individuals, that belong to the same species.

As shown previously, the use of the 3CADH model allows the emergence of species even when genome sizes are much below the threshold for speciation required by the DH model. The question arises on how large the assortativity chromosome should be for the model to preserve the speciation feature. To address this question, we show in Figure 6

the number of species according to the 3CADH model for different sizes of the assortativity chromosome and fixed size of the compatibility for mating chromosome $C = 100$. It shows that speciation occurs when the assortativity chromosome size is in a range from long enough to complement the genome without a neutral chromosome, to as small as 0.4% of the genome. Moreover, we note a few variations in the evolution of the species as the assortativity chromosome size changes. We start by pointing at the similarities in the structure of genetic distance distributions. Similar to the single-chromosome model, there is a single peak close to 1, which arises due to the differences between species clusters, and small peaks drifting from 0 to 1, evidencing the similarities between individuals within the species. In these cases, however, the drifting of the distribution, which leads to the formation of the single peak on the right, is faster when the assortativity chromosome is longer. This response highlights the ease of forming species when mating choosiness guarantees that sexual partners will be most similar to focal individuals. From the cluster transitions, we also notice a variation in the number of species dependent on the assortativity chromosome size. When the assortativity chromosome size surpasses this threshold, the number of species converges to a fixed number, as opposed to when the chromosome size is below, where the number of species is dependent on it.

All the effects previously described can be addressed by understanding the linkage between chromosomes in the 3CADH process. If the assortativity chromosome were much larger than the others, the process would be almost identical to asexual reproduction. Despite finding a first compatibility subset, the second step of finding the most similar partner with the assortativity chromosome would imply a high level of genetic similarity between the mating pair. The effect of the assortativity chromosome driving speciation is shown in Figure 7, where the system exhibits a stable behavior even in the case where only one gene determines assortativity. The averaged genetic distance of the DH model converges to the threshold value d_{max} due that the genome size is not long enough to generate species. The asexual and homogeneous models show the convergence of the averaged genetic distance to the mean value d_0. Whereas, for different sizes of assortativity chromosome, the convergence of the averaged genetic distance ranges from d_{max} to d_0.

3.3 The trouble with assortativity

In the previous sections we have shown results for strict assortativity only: among all compatible individuals (as dictated by the compatibility chromosome C) only the most similar to the mating individual (with respect to A) have a chance of reproducing with it. Those differing by a single extra allele would never be chosen. Here we relax this condition letting the choosiness parameter r be positive.

To have an idea of the effects of r we note that for $A = 100$ and $r = 0.02A$, we
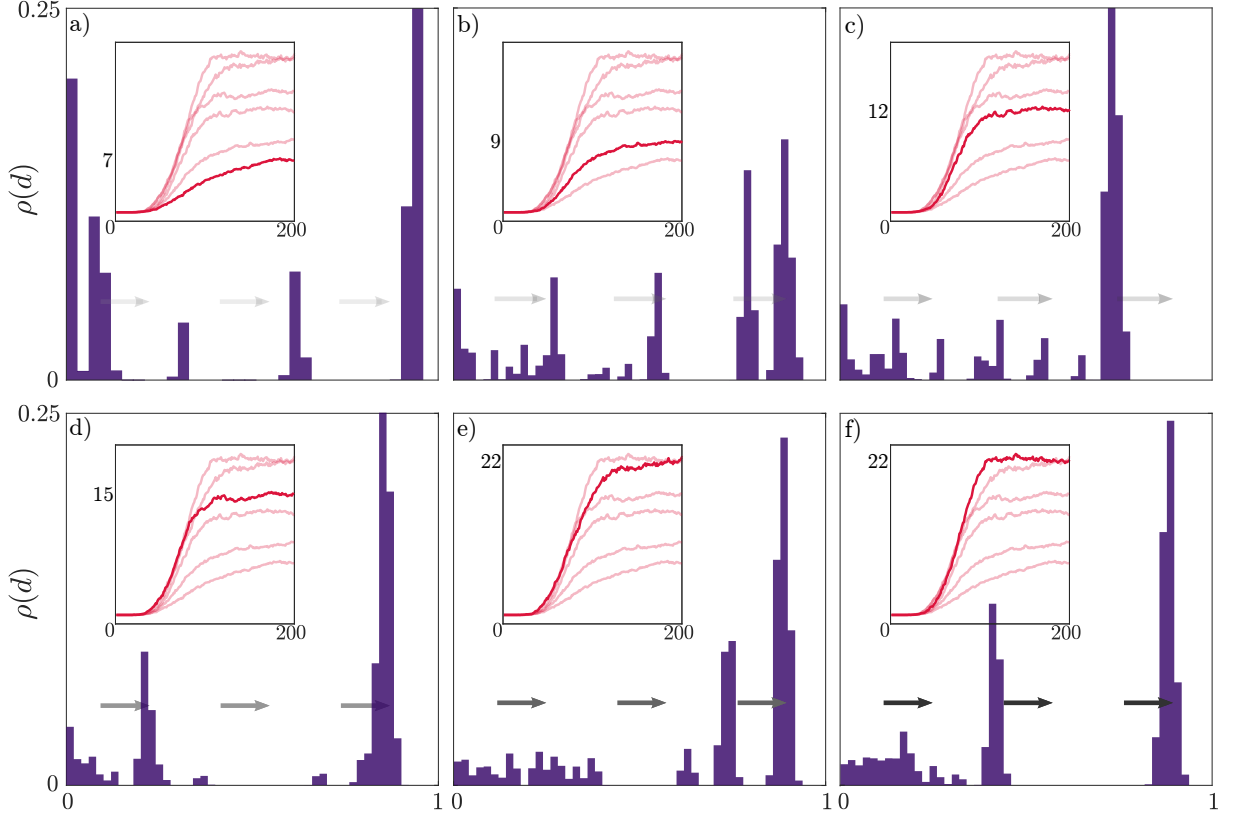
Figure 6 – Genetic distance distributions in the 3CADH model at $T = 1000$ for a) $A = 10$, b) $A = 20$, c) $A = 50$, d) $A = 100$, e) $A = 1000$, and f) $A = 2400$. Simulations were performed for $M = 500$, $F = 2500$, $\mu = 10^{-3}$, and $C = 100$. In each case, embedded figures show the average number of species as a function of the time, with the bold line representing the curve for the corresponding set of parameters. The light curves show the evolution for parameters in the other panels, for comparison. Bolder arrows indicate that the distribution drifting is faster.

include as potential mating partners individuals differing by 1 or 2 extra alleles beyond the maximum similarity at that moment. Note that the number of extra individuals included in the set increases rapidly as r increases. Therefore, we expect assortativity to stop working as a powerful selection mechanism quite soon.

Figure 8 shows the effect of r on the number of species for different sizes of the assortativity chromosome. We observe that indeed r leads to a rapid decrease of the number of species, especially for small values of A. Besides, it also delays speciation and slows down equilibration.

3.4 Discussion

We have studied the effects of assortativity in the emergence of species in a sympatric population of hermaphrodites individuals that reproduce sexually. Our work
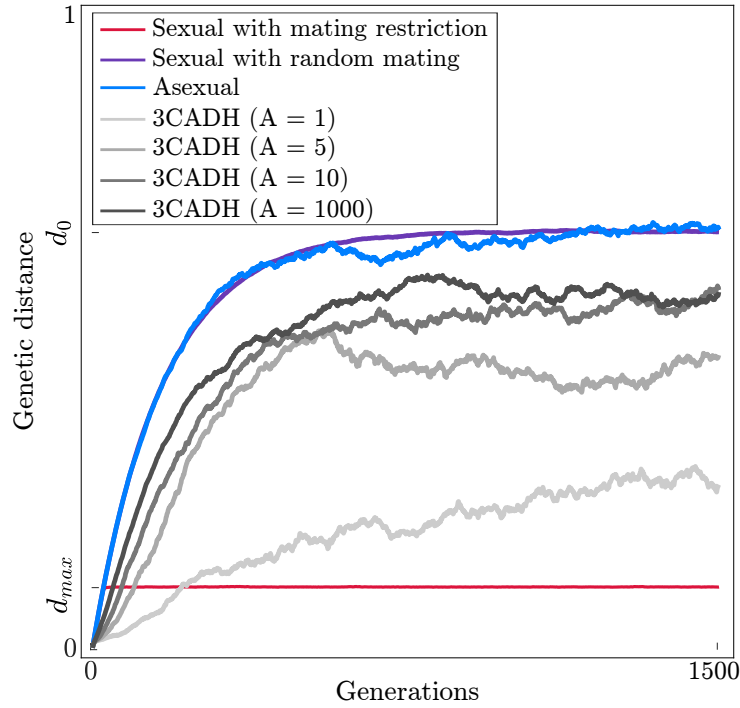
Figure 7 – Average genetic distance for the asexual, sexual with random mating, sexual with mating restriction, and 3CADH cases. Each case shows an average of 50 executions along $T = 1500$ generations for $M = 500$ and $F = 2500$.
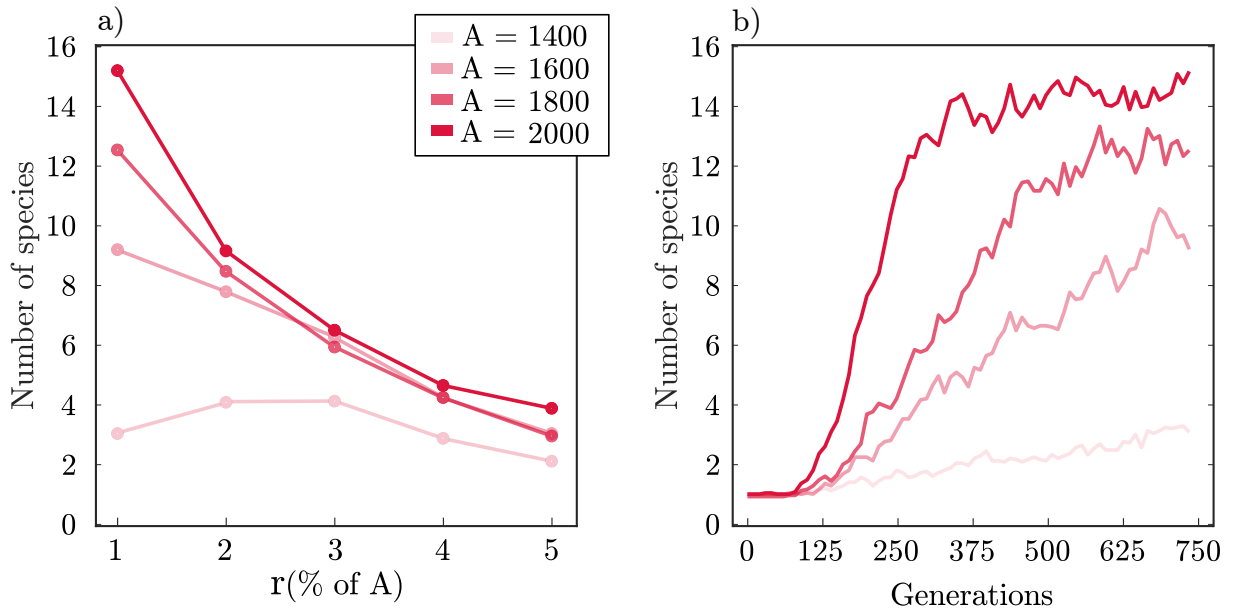
Figure 8 – Effects of choosiness on the emergence of species. Simulations were performed for $M = 500$, $F = 2500$, $\mu = 10^{-3}$, and $C = 100$. Both figures picture results from averaging 25 executions for the respective parameters. In a), each dot represents the number of species after 750 generations for different values of A and r. In b), each line describes the generational evolution of the number of species for different values of A and fixed $r = 0.01A$.

is based on the model proposed by Higgs and Derrida (DH) [44], where individuals are represented by biallelic genomes and reproduction requires the genomes of the mating pair to be sufficiently similar (genetic compatibility). Speciation in this scenario only happens if the genome size is sufficiently large (of the order of 4000 genes for the parameters used in our work). Here, we generalize the representation of the individuals and the way mating partners are selected. Individuals are represented by three chromosomes: a compatibility C, an assortativity A, and a neutral N chromosome. As in the DH model, mating is allowed only between compatible individuals, with Hamming distance between their C chromosomes smaller than a threshold value G. However, among the compatibles, the one with maximum genetic similarity with respect to the A chromosome is chosen.

We have shown that, in our model, speciation occurs even when genome size is small, much below the threshold required for the original DH model [48]. This drastic change in genome size requirement for speciation is a consequence of assortativity and the corresponding decrease in the gene flow it promotes. We have also shown that species, which are classified according to reproductive isolation imposed by the compatibility chromosome, can also be identified by comparing the N chromosome, which works as a proxy for reproductive isolation.

The dynamics of species formation in our model can be understood as follows: in the beginning of the simulation all chromosomes are identical and, therefore, all individuals are compatible. Mutations introduce small differences that, although are not enough to create incompatibilities during the first generations, produce different versions of the assortativiy chromosome. Individuals with a unique A chromosome never get selected for reproduction, and although these individuals have the chance of mating at least once, the rarity of their A chromosome will culminate with its disappearance. Groups of individuals with identical A's, on the other hand, will only mate among themselves, as they select the most similar possible partner. This creates clusters of individuals with very similar A chromosome. The key effect of this process is to create small isolated groups that, although not reproductively isolated from rest of the population, will only mate with others from the same group, purging new mutations in chromosome A. After the formation of such isolated groups, further mutations and drift lead the C chromosome to differentiate among groups, leading eventually to the formation of species. As shown in Figure 7, one single locus in the A chromosome guarantees the emergence of genetic variation necessary for diversification – at least in the case of strong assortativity, as imposed by the model.

Our results also reveal that, despite each chromosome and each locus being independent, there is genetic linkage disequilibrium (LD) in all the different chromosomes. The mechanism of assortativity leads indirectly to such correlations via species formation. As a consequence both the compatibility and the neutral chromosomes can identify almost exactly the same species. Therefore, although the neutral chromosome does not participate

in the dynamics of reproduction, it suffers the dynamic consequences that occur in the other chromosomes and mirrors the arrangement they went through. Assortative mating has been proposed as a mechanism that can lead to speciation, particularly in sympatric scenarios [29, 52–55]. For assortative mating to drive speciation, theoretical models often require disruptive selection, such as those proposed by Dieckmann and Doebeli [29] or scenarios where different fixed alleles exist in each subpopulation [53, 56]. One of the most influential works in this area is Felsenstein's 1981 paper, where he proposed genetic forces involved in speciation that incorporated assortative mating. He developed two different models using three gene loci, where the biallelic loci B and C were under selection in two different subpopulations connected by migration. The BC haplotype was favored in one subpopulation, while the bc was favored in the other.

In the one-allele model, Felsenstein predicted that the expression of a third gene locus (A) coding for strong assortativity in both subpopulations would reduce gene flow and induce speciation. In the framework of our model, this would be similar to impose a spatial mating neighborhood, where individuals can find their mates. In that case gene flow is reduced by this spatial mating restriction, without the need for an assortativity chromosome, as explored in [47, 48, 57–59]. In the other Felsenstein's model, the two-allele model, two (or more) alleles in the third locus define the mating preference of individuals. Carriers of the allele A (a) prefer to mate with those also carrying A (a). If A is preferred in the habitat where the BC haplotype is being favored, and a is preferred in the habitat with bc haplotypes, then a linkage disequilibrium (LD) emerges. However, due to genetic recombination dissolving the LD, Felsenstein predicted that this model was unlikely to lead to speciation [36, 53, 56].

The model explored in this work resembles the two-allele model, but with more alleles. We show, in contrast to Felsenstein's predictions, that assortative mating induces speciation in this sympatric scenario. Additionally, we do not require disruptive selection or differential selection by habitat for species to form. However, we do impose a genetic threshold in the compatibility chromosome, which defines the pool of compatible individuals and is also used for species definition. Assortative mating acts as the initial spark for species formation, reducing gene flow between dissimilar individuals and allowing speciation to occur. We observed LD among different chromosomes identifying almost the same species. Since during sexual mating offspring inherit each locus independently from their parents, we see that sexual reproduction is not breaking genetic associations that lead to speciation. We are aware of the lack of evidence for the two-allele model. However, as Servedio and Noor (2003) have pointed out [60], it is very difficult to distinguish whether the process by which a group of species evolved was a one-allele or two-allele scenario.

We expect that the gene flow interruption induced by assortativity may persist to some degree if this mating mechanism disappears due to biological cost or selection.

To further investigate the effects of choosiness in reducing gene flow and creating initial clusters of individuals, future studies could relax the strong assortativity we imposed by using a probability distribution or by creating pools of possible partners [42]. Additionally, decreasing assortativity after species have formed could help shed light on the significance of choosiness for species maintenance.

Sympatric speciation is a controversial topic [61–63] due to the difficulty in gathering information and fossilized evidence, as well as the challenges of manipulating complex life forms in laboratory settings. However, as science advances, it also creates the necessary tools for solving old problems and analysing classic questions with less limitations and genomics is an allied for this open problem in the coming years [64, 65]. Despite these limitations, we recognize the importance of theoretical approaches in helping to understand and potentially recognize this process in nature.

4 Frustration and chaos in systems of swarmalators

Swarming and synchronization are emergent phenomena observed in various natural systems. Swarming, more noticeable due to its occurrence in physical space, is evidenced in groups of fishes, birds, insects, and bacteria, among others [8, 66–73]. Synchronization, sometimes less apparent due to its nature, is observed in both living and non-living systems, including groups of humans, frogs, heart cells, and neurons, among others [16, 74–79]. From a theoretical standpoint, both phenomena have been extensively studied using distinct frameworks based on well-known models named after Kuramoto [21], Stuart-Landau [80], Couzin [81], and Vicsek [11]. In these models, single particles are represented by their positions or by periodic internal degrees of freedom dubbed phases. Then, individuals' spatial self-organization gives rise to swarming and, in the case of phase coherence, synchronization.

A model that merges swarming and synchronization into one was introduced by O'Keeffe and Strogatz [82]. In this, hypothetical individuals can move in space while possessing internal phases, which can synchronize. Moreover, spatial positioning affects the phase states and vice versa. This model, however, presents several drawbacks proper of its complexity. Similarly to previous swarming models, particles are not constrained to intrinsic behaviors. Also, the interactions between individuals drive the system to unrealistic radial distributions in space. And most importantly, the system is intractable analytically. Here, we study systems of swarmalators modeled using periodic boundary conditions. This consideration allows for the analytical treatment of these systems. We present individuals with their spatial motion constrained to a ring as well as a torus. In the former case, individuals' degrees of freedom are affected by frustration, similar to the Sakaguchi variation of the Kuramoto model [83]. In the latter case, individuals' interactions generate the emergence of static, active, and chaotic states.

The work corresponding to this section is composed of two papers published in Physical Review E [84, 85], both authored by the master's student and the advisor.

Conclusions

In this work, we have presented the study of two different phenomena: speciation and self-organization. Firstly, we showed the effects of considering assortativity in the mating process of a neutral population. Our findings reveal that speciation is promoted under strict assortativity conditions. In this setup, species arise even with finite-sized genomes, contrary to previous studies where genome sizes had to be large. Additionally, clusters formed by considering the compatibility of neutral chromosomes correlate with those representing species. This feature enables species identification using any of the chromosomes, rather than solely relying on the one associated with reproductive compatibility. Finally, we found that relaxing the assortativity conditions undermines their effectiveness, leading to the emergence of fewer species or even none at all.

Secondly, we explored self-organization in terms of swarming and synchronization and their interaction. For this, we presented two models of swarmalators: one where individuals are confined to a spatial ring, and a second where they can move on a torus. In the former, we considered frustration parameters affecting phase and spatial dynamics, which led to the emergence of several static and active collective states. These states were analyzed numerically and analytically. They were localized in the parameter space, identifying regions of multistability and areas where disordered states emerge. In the latter model, individuals can move in two dimensions. As well as in the one-dimensional model, we evaluated all the ordered static and active states numerically and analytically. Interestingly, in the active regime, populations of swarmalators can exhibit chaotic behavior. Furthermore, this chaotic state can be observed globally, while the spatial degrees of freedom remain correlated. The breaking of this correlation, which occurs when coupling parameters are strong, is interpreted as a dimensional transition.

Bibliography

1 DARWIN, C. On the origin of species by means of natural selection. 1859. *London: Murray Google Scholar*, 1968.

2 LOSOS, J. B. *The Princeton guide to evolution.* [S.l.]: Princeton University Press, 2017.

3 COYNE, J. A.; ORR, H. A. et al. *Speciation.* [S.l.]: Sinauer associates Sunderland, MA, 2004. v. 37.

4 BARTON, N.; BENGTSSON, B. O. The barrier to genetic exchange between hybridising populations. *Heredity*, Nature Publishing Group, v. 57, n. 3, p. 357–376, 1986.

5 CAMAZINE, S.; DENEUBOURG, J.-L.; FRANKS, N. R.; SNEYD, J.; THERAULA, G.; BONABEAU, E. Self-organization in biological systems. In: *Self-Organization in Biological Systems.* [S.l.]: Princeton university press, 2020.

6 OH, H.; SHIRAZI, A. R.; SUN, C.; JIN, Y. Bio-inspired self-organising multi-robot pattern formation: A review. *Robotics and Autonomous Systems*, Elsevier, v. 91, p. 83–100, 2017.

7 BAJEC, I. L.; HEPPNER, F. H. Organized flight in birds. *Animal Behaviour*, Elsevier, v. 78, n. 4, p. 777–789, 2009.

8 LARSSON, M. Why do fish school? *Current Zoology*, Oxford University Press Oxford, Uk, v. 58, n. 1, p. 116–128, 2012.

9 SCHNEIRLA, T. C.; PIEL, G. The army ant. *Scientific American*, JSTOR, v. 178, n. 6, p. 16–23, 1948.

10 REYNOLDS, C. W. Flocks, herds and schools: A distributed behavioral model. In: *Proceedings of the 14th annual conference on Computer graphics and interactive techniques.* [S.l.: s.n.], 1987. p. 25–34.

11 VICSEK, T.; CZIRÓK, A.; BEN-JACOB, E.; COHEN, I.; SHOCHET, O. Novel type of phase transition in a system of self-driven particles. *Physical review letters*, APS, v. 75, n. 6, p. 1226, 1995.

12 CUCKER, F.; SMALE, S. On the mathematics of emergence. *Japanese Journal of Mathematics*, Springer, v. 2, p. 197–227, 2007.

13 _____. Emergent behavior in flocks. *IEEE Transactions on automatic control*, IEEE, v. 52, n. 5, p. 852–862, 2007.

14 TONER, J.; TU, Y. Flocks, herds, and schools: A quantitative theory of flocking. *Physical review E*, APS, v. 58, n. 4, p. 4828, 1998.

15 SARFATI, R.; JOSHI, K.; MARTIN, O.; HAYES, J. C.; IYER-BISWAS, S.; PELEG, O. Emergent periodicity in the collective synchronous flashing of fireflies. *Elife*, eLife Sciences Publications, Ltd, v. 12, p. e78908, 2023.

16 NÉDA, Z.; RAVASZ, E.; BRECHET, Y.; VICSEK, T.; BARABÁSI, A.-L. The sound of many hands clapping. *Nature*, Nature Publishing Group UK London, v. 403, n. 6772, p. 849–850, 2000.

17 KÖNIG, P.; ENGEL, A. K.; ROELFSEMA, P. R.; SINGER, W. How precise is neuronal synchronization? *Neural Computation*, MIT Press One Rogers Street, Cambridge, MA 02142-1209, USA journals-info . . . , v. 7, n. 3, p. 469–485, 1995.

18 WINFREE, A. T. Biological rhythms and the behavior of populations of coupled oscillators. *Journal of theoretical biology*, Elsevier, v. 16, n. 1, p. 15–42, 1967.

19 KURAMOTO, Y. International symposium on mathematical problems in theoretical physics. *Lecture notes in Physics*, v. 30, p. 420, 1975.

20 KURAMOTO, Y.; KURAMOTO, Y. *Chemical turbulence.* [S.l.]: Springer, 1984.

21 STROGATZ, S. H. From kuramoto to crawford: exploring the onset of synchronization in populations of coupled oscillators. *Physica D: Nonlinear Phenomena*, Elsevier, v. 143, n. 1-4, p. 1–20, 2000.

22 RODRIGUES, F. A.; PERON, T. K. D.; JI, P.; KURTHS, J. The kuramoto model in complex networks. *Physics Reports*, Elsevier, v. 610, p. 1–98, 2016.

23 NOSIL, P. *Ecological speciation.* [S.l.]: Oxford University Press, 2012.

24 MAYR, E. Animal species and evolution. In: *Animal species and evolution.* [S.l.]: Harvard University Press, 2013.

25 MANZO, F.; PELITI, L. Geographic speciation in the Derrida-Higgs model of species formation. *Journal of Physics A: Mathematical and General*, v. 27, n. 21, p. 7079, 1994.

26 YAMAGUCHI, R.; IWASA, Y. First passage time to allopatric speciation. *Interface Focus*, Royal Society, v. 3, n. 6, p. 20130026, 2013. ISSN 2042-8898.

27 PRINCEPE, D.; CZARNOBAI, S.; PRADELLA, T. M.; CAETANO, R. A.; MARQUITTI, F.; AGUIAR, M. A. de; ARAUJO, S. B. Diversity patterns and speciation processes in a two-island system with continuous migration. *arXiv preprint arXiv:2202.11510*, 2022.

28 NOSIL, P.; SCHLUTER, D. The genes underlying the process of speciation. *Trends in Ecology & Evolution*, Elsevier, v. 26, n. 4, p. 160–167, 2011.

29 DIECKMANN, U.; DOEBELI, M. On the origin of species by sympatric speciation. *Nature*, v. 400, n. 6742, p. 354–357, 1999.

30 DOEBELI, M.; DIECKMANN, U. Speciation along environmental gradients. *Nature*, v. 421, n. 6920, p. 259–264, 01 2003. Disponível em: <http://dx.doi.org/10.1038/nature01274>.

31 POLECHOVÁ, J.; BARTON, N. H. Speciation through competition: a critical review. *Evolution*, Wiley Online Library, v. 59, n. 6, p. 1194–1210, 2005.

32 COOLEY, J. R.; SIMON, C.; MARSHALL, D. C. Temporal separation and speciation in periodical cicadas. *Bioscience*, American Institute of Biological Sciences, v. 53, n. 2, p. 151–157, 2003.

33 TAYLOR, R. S.; FRIESEN, V. L. The role of allochrony in speciation. *Molecular Ecology*, Wiley Online Library, v. 26, n. 13, p. 3330–3342, 2017.

34 MCKINNON, J. S.; MORI, S.; BLACKMAN, B. K.; DAVID, L.; KINGSLEY, D. M.; JAMIESON, L.; CHOU, J.; SCHLUTER, D. Evidence for ecology's role in speciation. *Nature*, Nature Publishing Group UK London, v. 429, n. 6989, p. 294–298, 2004.

35 JANICKE, T.; MARIE-ORLEACH, L.; AUBIER, T. G.; PERRIER, C.; MORROW, E. H. Assortative mating in animals and its role for speciation. *The American Naturalist*, The University of Chicago Press Chicago, IL, v. 194, n. 6, p. 865–875, 2019.

36 KOPP, M.; SERVEDIO, M. R.; MENDELSON, T. C.; SAFRAN, R. J.; RODRÍGUEZ, R. L.; HAUBER, M. E.; SCORDATO, E. C.; SYMES, L. B.; BALAKRISHNAN, C. N.; ZONANA, D. M. et al. Mechanisms of assortative mating in speciation with gene flow: connecting theory and empirical research. *The American Naturalist*, University of Chicago Press Chicago, IL, v. 191, n. 1, p. 1–20, 2018.

37 IRWIN, D. E. Assortative mating in hybrid zones is remarkably ineffective in promoting speciation. *The American Naturalist*, The University of Chicago Press Chicago, IL, v. 195, n. 6, p. E150–E167, 2020.

38 BOUMANS, L.; HOGNER, S.; BRITTAIN, J.; JOHNSEN, A. Ecological speciation by temporal isolation in a population of the stonefly leuctra hippopus (plecoptera, leuctridae). *Ecology and Evolution*, Wiley Online Library, v. 7, n. 5, p. 1635–1649, 2017.

39 RIESEBERG, L. H.; BLACKMAN, B. K. Speciation genes in plants. *Annals of Botany*, Oxford University Press, v. 106, n. 3, p. 439–455, 2010.

40 KONDRASHOV, A. S.; SHPAK, M. On the origin of species by means of assortative mating. *Proceedings of the Royal Society of London. Series B: Biological Sciences*, The Royal Society, v. 265, n. 1412, p. 2273–2278, 1998.

41 DOEBELI, M.; DIECKMANN, U. Evolutionary branching and sympatric speciation caused by different types of ecological interactions. *The American Naturalist*, The University of Chicago Press, v. 156, n. S4, p. S77–S101, 2000.

42 CAETANO, R. A.; SANCHEZ, S.; COSTA, C. L.; AGUIAR, M. A. M. de. Sympatric speciation based on pure assortative mating. *Journal of Physics A: Mathematical and Theoretical*, IOP Publishing, v. 53, n. 15, p. 155601, 2020.

43 BOLNICK, D. I.; FITZPATRICK, B. M. Sympatric speciation: Models and empirical evidence. *Annual Review of Ecology, Evolution, and Systematics*, v. 38, n. 1, p. 459–487, 2007. Disponível em: <http://dx.doi.org/10.1146/annurev.ecolsys.38.091206.095804>.

44 HIGGS, P. G.; DERRIDA, B. Stochastic models for species formation in evolving populations. *Journal of Physics A: Mathematical and General*, IOP Publishing, v. 24, n. 17, p. L985, 1991.

45 _____. Genetic distance and species formation in evolving populations. *Journal of Molecular Evolution*, Springer, v. 35, n. 5, p. 454–465, 1992.

46 GAVRILETS, S.; HAI, L.; VOSE, M. D. Rapid parapatric speciation on holey adaptive landscapes. *Proceedings of the Royal Society of London. Series B: Biological Sciences*, The Royal Society, v. 265, n. 1405, p. 1483–1489, 1998.

47 AGUIAR, M. A. M. de; BARANGER, M.; BAPTESTINI, E.; KAUFMAN, L.; BAR-YAM, Y. Global patterns of speciation and diversity. *Nature*, Nature Publishing Group, v. 460, n. 7253, p. 384–387, 2009.

48 AGUIAR, M. A. de. Speciation in the derrida–higgs model with finite genomes and spatial populations. *Journal of Physics A: Mathematical and Theoretical*, IOP Publishing, v. 50, n. 8, p. 085602, 2017.

49 ROSENTHAL, G. G. *Mate choice: the evolution of sexual decision making from microbes to humans.* [S.l.]: Princeton University Press, 2017.

50 PUEBLA, O.; BERMINGHAM, E.; GUICHARD, F. Pairing dynamics and the origin of species. *Proceedings of the Royal Society B: Biological Sciences*, The Royal Society, v. 279, n. 1731, p. 1085–1092, 2012.

51 BAPTESTINI, E. M.; AGUIAR, M. A. de; BAR-YAM, Y. Conditions for neutral speciation via isolation by distance. *Journal of theoretical biology*, Elsevier, v. 335, p. 51–56, 2013.

52 SMITH, J. M. Sympatric speciation. *The American Naturalist*, Science Press, v. 100, n. 916, p. 637–650, 1966.

53 FELSENSTEIN, J. Skepticism towards santa rosalia, or why are there so few kinds of animals? *Evolution*, [Society for the Study of Evolution, Wiley], v. 35, n. 1, p. 124–138, 1981. ISSN 00143820, 15585646. Disponível em: <http://www.jstor.org/stable/2407946>.

54 FRY, J. D. Multilocus models of sympatric speciation: Bush versus rice versus felsenstein. *Evolution*, Blackwell Publishing Ltd Oxford, UK, v. 57, n. 8, p. 1735–1746, 2003.

55 BOLNICK, D. I. Waiting for sympatric speciation. *Evolution*, [Society for the Study of Evolution, Wiley], v. 58, n. 4, p. 895–899, 2004. ISSN 00143820, 15585646.

56 BUTLIN, R. K.; SERVEDIO, M. R.; SMADJA, C. M.; BANK, C.; BARTON, N. H.; FLAXMAN, S. M.; GIRAUD, T.; HOPKINS, R.; LARSON, E. L.; MAAN, M. E. et al. Homage to felsenstein 1981, or why are there so few/many species? *Evolution*, Blackwell Publishing Inc Malden, USA, v. 75, n. 5, p. 978–988, 2021.

57 MARTINS, A. B.; AGUIAR, M. A. de; BAR-YAM, Y. Evolution and stability of ring species. *Proceedings of the National Academy of Sciences*, National Acad Sciences, v. 110, n. 13, p. 5080–5084, 2013.

58 COSTA, C. L.; LEMOS-COSTA, P.; MARQUITTI, F. M.; FERNANDES, L. D.; RAMOS, M. F.; SCHNEIDER, D. M.; MARTINS, A. B.; AGUIAR, M. A. de. Signatures of microevolutionary processes in phylogenetic patterns. *Systematic Biology*, Oxford University Press, v. 68, n. 1, p. 131–144, 2019.

59 MARQUITTI, F. M. D.; FERNANDES, L. D.; AGUIAR, M. A. M. de. Allopatry increases the balance of phylogenetic trees during radiation under neutral speciation. *Ecography*, Wiley Online Library, v. 43, n. 10, p. 1487–1498, 2020.

60 SERVEDIO, M. R.; NOOR, M. A. The role of reinforcement in speciation: theory and data. *Annual Review of Ecology, Evolution, and Systematics*, Annual Reviews 4139 El Camino Way, PO Box 10139, Palo Alto, CA 94303-0139, USA, v. 34, n. 1, p. 339–364, 2003.

61 COYNE, J. A.; PRICE, T. D. Little evidence for sympatric speciation in island birds. *Evolution*, Blackwell Publishing Inc Malden, USA, v. 54, n. 6, p. 2166–2171, 2000.

62 BOLNICK, D. I.; FITZPATRICK, B. M. Sympatric speciation: models and empirical evidence. *Annual Review of Ecology, Evolution, and Systematics*, Annual Reviews, v. 38, p. 459–487, 2007.

63 FITZPATRICK, B.; FORDYCE, J.; GAVRILETS, S. What, if anything, is sympatric speciation? *Journal of Evolutionary Biology*, Wiley Online Library, v. 21, n. 6, p. 1452–1459, 2008.

64 FOOTE, A. D. Sympatric speciation in the genomic era. *Trends in Ecology & Evolution*, Elsevier, v. 33, n. 2, p. 85–95, 2018.

65 RICHARDS, E. J.; SERVEDIO, M. R.; MARTIN, C. H. Searching for sympatric speciation in the genomic era. *BioEssays*, Wiley Online Library, v. 41, n. 7, p. 1900047, 2019.

66 MARRAS, S.; KILLEN, S. S.; LINDSTRÖM, J.; MCKENZIE, D. J.; STEFFENSEN, J. F.; DOMENICI, P. Fish swimming in schools save energy regardless of their spatial position. *Behavioral ecology and sociobiology*, Springer, v. 69, p. 219–226, 2015.

67 EMLEN, J. T. Flocking behavior in birds. *The Auk*, JSTOR, v. 69, n. 2, p. 160–170, 1952.

68 BIALEK, W.; CAVAGNA, A.; GIARDINA, I.; MORA, T.; SILVESTRI, E.; VIALE, M.; WALCZAK, A. M. Statistical mechanics for natural flocks of birds. *Proceedings of the National Academy of Sciences*, National Acad Sciences, v. 109, n. 13, p. 4786–4791, 2012.

69 SULLIVAN, R. T. Insect swarming and mating. *The Florida Entomologist*, JSTOR, v. 64, n. 1, p. 44–65, 1981.

70 CHITTKA, L.; ROSSI, N. Social cognition in insects. *Trends in Cognitive Sciences*, Elsevier, 2022.

71 KEARNS, D. B. A field guide to bacterial swarming motility. *Nature Reviews Microbiology*, Nature Publishing Group UK London, v. 8, n. 9, p. 634–644, 2010.

72 ARIEL, G.; RABANI, A.; BENISTY, S.; PARTRIDGE, J. D.; HARSHEY, R. M.; BE'ER, A. Swarming bacteria migrate by lévy walk. *Nature communications*, Nature Publishing Group UK London, v. 6, n. 1, p. 8396, 2015.

73 BE'ER, A.; ARIEL, G. A statistical physics view of swarming bacteria. *Movement ecology*, BioMed Central, v. 7, n. 1, p. 1–17, 2019.

74 STROGATZ, S. H.; ABRAMS, D. M.; MCROBIE, A.; ECKHARDT, B.; OTT, E. Crowd synchrony on the millennium bridge. *Nature*, Nature Publishing Group UK London, v. 438, n. 7064, p. 43–44, 2005.

75 YANIV, Y.; AHMET, I.; LIU, J.; LYASHKOV, A. E.; GUIRIBA, T.-R.; OKAMOTO, Y.; ZIMAN, B. D.; LAKATTA, E. G. Synchronization of sinoatrial node pacemaker cell clocks and its autonomic modulation impart complexity to heart beating intervals. *Heart Rhythm*, Elsevier, v. 11, n. 7, p. 1210–1219, 2014.

76 BYCHKOV, R.; JUHASZOVA, M.; TSUTSUI, K.; COLETTA, C.; STERN, M. D.; MALTSEV, V. A.; LAKATTA, E. G. Synchronized cardiac impulses emerge from heterogeneous local calcium signals within and among cells of pacemaker tissue. *Clinical Electrophysiology*, American College of Cardiology Foundation Washington DC, v. 6, n. 8, p. 907–931, 2020.

77 AIHARA, I.; HORAI, S.; KITAHATA, H.; AIHARA, K.; YOSHIKAWA, K. Dynamical calling behavior experimentally observed in japanese tree frogs (hyla japonica). *IEICE transactions on fundamentals of electronics, communications and computer sciences*, The Institute of Electronics, Information and Communication Engineers, v. 90, n. 10, p. 2154–2161, 2007.

78 AIHARA, I.; KITAHATA, H.; YOSHIKAWA, K.; AIHARA, K. Mathematical modeling of frogs' calling behavior and its possible application to artificial life and robotics. *Artificial Life and Robotics*, Springer, v. 12, p. 29–32, 2008.

79 UHLHAAS, P. J.; SINGER, W. Neural synchrony in brain disorders: relevance for cognitive dysfunctions and pathophysiology. *neuron*, Elsevier, v. 52, n. 1, p. 155–168, 2006.

80 AOYAGI, T. Network of neural oscillators for retrieving phase information. *Physical review letters*, APS, v. 74, n. 20, p. 4075, 1995.

81 COUZIN, I. D.; KRAUSE, J.; JAMES, R.; RUXTON, G. D.; FRANKS, N. R. Collective memory and spatial sorting in animal groups. *Journal of theoretical biology*, Elsevier, v. 218, n. 1, p. 1–11, 2002.

82 O'KEEFFE, K. P.; HONG, H.; STROGATZ, S. H. Oscillators that sync and swarm. *Nature communications*, Nature Publishing Group UK London, v. 8, n. 1, p. 1504, 2017.

83 SAKAGUCHI, H.; KURAMOTO, Y. A soluble active rotater model showing phase transitions via mutual entertainment. *Progress of Theoretical Physics*, Oxford University Press, v. 76, n. 3, p. 576–581, 1986.

84 LIZÁRRAGA, J. U.; AGUIAR, M. A. de. Synchronization of sakaguchi swarmalators. *Physical Review E*, APS, v. 108, n. 2, p. 024212, 2023.

85 LIZÁRRAGA, J. U.; O'KEEFFE, K. P.; AGUIAR, M. A. de. Order, chaos, and dimensionality transition in a system of swarmalators. *Physical Review E*, APS, v. 109, n. 4, p. 044209, 2024.

86 ACEBRÓN, J. A.; BONILLA, L. L.; VICENTE, C. J. P.; RITORT, F.; SPIGLER, R. The kuramoto model: A simple paradigm for synchronization phenomena. *Reviews of modern physics*, APS, v. 77, n. 1, p. 137, 2005.

87 RODRIGUES, F. A.; PERON, T. K. D. M.; JI, P.; KURTHS, J. The Kuramoto model in complex networks. *Physics Reports*, Elsevier B.V., v. 610, p. 1–98, 2016. ISSN 03701573. Disponível em: <http://dx.doi.org/10.1016/j.physrep.2015.10.008>.

88 MATTHEWS, P. C.; MIROLLO, R. E.; STROGATZ, S. H. Dynamics of a large system of coupled nonlinear oscillators. *Physica D: Nonlinear Phenomena*, Elsevier, v. 52, n. 2-3, p. 293–331, 1991.

89 KATZ, Y.; TUNSTRØM, K.; IOANNOU, C. C.; HUEPE, C.; COUZIN, I. D. Inferring the structure and dynamics of interactions in schooling fish. *Proceedings of the National Academy of Sciences*, National Acad Sciences, v. 108, n. 46, p. 18720–18725, 2011.

90 CAVAGNA, A.; CARLO, L. D.; GIARDINA, I.; GRIGERA, T. S.; MELILLO, S.; PARISI, L.; PISEGNA, G.; SCANDOLO, M. Natural swarms in 3.99 dimensions. *Nature Physics*, Nature Publishing Group UK London, p. 1–7, 2023.

91 AIHARA, I.; MIZUMOTO, T.; OTSUKA, T.; AWANO, H.; NAGIRA, K.; OKUNO, H. G.; AIHARA, K. Spatio-temporal dynamics in collective frog choruses examined by mathematical modeling and field observations. *Scientific reports*, Nature Publishing Group UK London, v. 4, n. 1, p. 3891, 2014.

92 ZHANG, B.; SOKOLOV, A.; SNEZHKO, A. Reconfigurable emergent patterns in active chiral fluids. *Nature communications*, Nature Publishing Group UK London, v. 11, n. 1, p. 4401, 2020.

93 GIOMI, L.; HAWLEY-WELD, N.; MAHADEVAN, L. Swarming, swirling and stasis in sequestered bristle-bots. *Proceedings of the Royal Society A: Mathematical, Physical and Engineering Sciences*, The Royal Society Publishing, v. 469, n. 2151, p. 20120637, 2013.

94 TAN, T. H.; MIETKE, A.; LI, J.; CHEN, Y.; HIGINBOTHAM, H.; FOSTER, P. J.; GOKHALE, S.; DUNKEL, J.; FAKHRI, N. Odd dynamics of living chiral crystals. *Nature*, Nature Publishing Group UK London, v. 607, n. 7918, p. 287–293, 2022.

95 CREPPY, A.; PLOURABOUÉ, F.; PRAUD, O.; DRUART, X.; CAZIN, S.; YU, H.; DEGOND, P. Symmetry-breaking phase transitions in highly concentrated semen. *Journal of The Royal Society Interface*, The Royal Society, v. 13, n. 123, p. 20160575, 2016.

96 LIZARRAGA, J. U.; AGUIAR, M. A. de. Synchronization and spatial patterns in forced swarmalators. *Chaos: An Interdisciplinary Journal of Nonlinear Science*, AIP Publishing LLC, v. 30, n. 5, p. 053112, 2020.

97 HONG, H. Active phase wave in the system of swarmalators with attractive phase coupling. *Chaos: An Interdisciplinary Journal of Nonlinear Science*, AIP Publishing LLC, v. 28, n. 10, p. 103112, 2018.

98 SAR, G. K.; CHOWDHURY, S. N.; PERC, M.; GHOSH, D. Swarmalators under competitive time-varying phase interactions. *New Journal of Physics*, IOP Publishing, v. 24, n. 4, p. 043004, 2022.

99 LEE, H. K.; YEO, K.; HONG, H. Collective steady-state patterns of swarmalators with finite-cutoff interaction distance. *Chaos: An Interdisciplinary Journal of Nonlinear Science*, AIP Publishing, v. 31, n. 3, 2021.

100 JIMÉNEZ-MORALES, F. Oscillatory behavior in a system of swarmalators with a short-range repulsive interaction. *Physical Review E*, APS, v. 101, n. 6, p. 062202, 2020.

101 JAPÓN, P.; JIMÉNEZ-MORALES, F.; CASARES, F. Intercellular communication and the organization of simple multicellular animals. *Cells & Development*, Elsevier, v. 169, p. 203726, 2022.

102 HONG, H.; O'KEEFFE, K. P.; LEE, J. S.; PARK, H. Swarmalators with thermal noise. *arXiv preprint arXiv:2302.11820*, 2023.

103 O'KEEFFE, K.; CERON, S.; PETERSEN, K. Collective behavior of swarmalators on a ring. *Physical Review E*, APS, v. 105, n. 1, p. 014211, 2022.

104 O'KEEFFE, K.; HONG, H. Swarmalators on a ring with distributed couplings. *Physical Review E*, APS, v. 105, n. 6, p. 064208, 2022.

105 SAR, G. K.; GHOSH, D.; O'KEEFFE, K. Pinning in a system of swarmalators. *Physical Review E*, APS, v. 107, n. 2, p. 024215, 2023.

106 YOON, S.; O'KEEFFE, K.; MENDES, J.; GOLTSEV, A. Sync and swarm: Solvable model of nonidentical swarmalators. *Physical Review Letters*, APS, v. 129, n. 20, p. 208002, 2022.

107 CERON, S.; O'KEEFFE, K.; PETERSEN, K. Diverse behaviors in non-uniform chiral and non-chiral swarmalators. *Nature Communications*, Nature Publishing Group UK London, v. 14, n. 1, p. 940, 2023.

108 KRUK, N.; MAISTRENKO, Y.; KOEPPL, H. Self-propelled chimeras. *Physical Review E*, APS, v. 98, n. 3, p. 032219, 2018.

109 STROGATZ, S. H.; MIROLLO, R. E. Stability of incoherence in a population of coupled oscillators. *Journal of Statistical Physics*, Springer, v. 63, p. 613–635, 1991.

110 SCHOELLER, S. F.; HOLT, W. V.; KEAVENY, E. E. Collective dynamics of sperm cells. *Philosophical Transactions of the Royal Society B*, The Royal Society, v. 375, n. 1807, p. 20190384, 2020.

111 DAIDO, H. Quasientrainment and slow relaxation in a population of oscillators with random and frustrated interactions. *Physical review letters*, APS, v. 68, n. 7, p. 1073, 1992.

112 OMEL'CHENKO, E.; WOLFRUM, M. Nonuniversal transitions to synchrony in the sakaguchi-kuramoto model. *Physical review letters*, APS, v. 109, n. 16, p. 164101, 2012.

113 MANORANJANI, M.; GUPTA, S.; CHANDRASEKAR, V. The sakaguchi–kuramoto model in presence of asymmetric interactions that break phase-shift symmetry. *Chaos: An Interdisciplinary Journal of Nonlinear Science*, AIP Publishing LLC, v. 31, n. 8, p. 083130, 2021.

114 ARNAUDON, A.; PEACH, R. L.; PETRI, G.; EXPERT, P. Connecting hodge and sakaguchi-kuramoto through a mathematical framework for coupled oscillators on simplicial complexes. *Communications Physics*, Nature Publishing Group UK London, v. 5, n. 1, p. 211, 2022.

115 AGUIAR, M. A. M. de. Generalized frustration in the multidimensional kuramoto model. *Phys. Rev. E*, American Physical Society, v. 107, p. 044205, Apr 2023. Disponível em: <https://link.aps.org/doi/10.1103/PhysRevE.107.044205>.

116 AIHARA, I.; KITAHATA, H.; AIHARA, K.; YOSHIKAWA, K. Periodic rhythm and anti-phase synchronization in calling behaviors of japanese rain frogs. *METR*, v. 35, p. 1–10, 2006.

117 MAGGI, C.; SAGLIMBENI, F.; SOSA, V. C.; LEONARDO, R. D.; NATH, B.; PUGLISI, A. Thermodynamic limits of sperm swimming precision. *PRX Life*, APS, v. 1, n. 1, p. 013003, 2023.

118 CREPPY, A.; PRAUD, O.; DRUART, X.; KOHNKE, P. L.; PLOURABOUÉ, F. Turbulence of swarming sperm. *Physical Review E*, APS, v. 92, n. 3, p. 032722, 2015.

119 PESHKOV, A.; MCGAFFIGAN, S.; QUILLEN, A. C. Synchronized oscillations in swarms of nematode turbatrix aceti. *Soft Matter*, Royal Society of Chemistry, v. 18, n. 6, p. 1174–1182, 2022.

120 YUAN, J.; RAIZEN, D. M.; BAU, H. H. Gait synchronization in caenorhabditis elegans. *Proceedings of the National Academy of Sciences*, National Acad Sciences, v. 111, n. 19, p. 6865–6870, 2014.

121 ĒRGLIS, K.; WEN, Q.; OSE, V.; ZELTINS, A.; SHARIPO, A.; JANMEY, P. A.; CĒBERS, A. Dynamics of magnetotactic bacteria in a rotating magnetic field. *Biophysical journal*, Elsevier, v. 93, n. 4, p. 1402–1412, 2007.

122 SARFATI, R.; HAYES, J. C.; SARFATI, É.; PELEG, O. Spatio-temporal reconstruction of emergent flash synchronization in firefly swarms via stereoscopic 360-degree cameras. *Journal of The Royal Society Interface*, The Royal Society, v. 17, n. 170, p. 20200179, 2020.

123 QUILLEN, A.; PESHKOV, A.; CHAKRABARTI, B.; SKERRETT, N.; MCGAFFIGAN, S.; ZAPIACH, R. Fluid circulation driven by collectively organized metachronal waves in swimming t. aceti nematodes. *Physical Review E*, APS, v. 106, n. 6, p. 064401, 2022.

124 BAROTTA, J.-W.; THOMSON, S. J.; ALVENTOSA, L. F.; LEWIS, M.; HARRIS, D. M. Bidirectional wave-propelled capillary spinners. *Communications Physics*, Nature Publishing Group UK London, v. 6, n. 1, p. 87, 2023.

125 MANNA, R. K.; SHKLYAEV, O. E.; BALAZS, A. C. Chemical pumps and flexible sheets spontaneously form self-regulating oscillators in solution. *Proceedings of the National Academy of Sciences*, National Acad Sciences, v. 118, n. 12, p. e2022987118, 2021.

126 ALI, N.; NAND, S.; KIRAN, A.; MISHRA, M.; MEHANDIA, V. Oscillating rheological behavior of turbatrix aceti nematodes. *Physics of Fluids*, AIP Publishing, v. 35, n. 1, 2023.

127 MCLENNAN-SMITH, T. A.; ROBERTS, D. O.; SIDHU, H. S. Emergent behavior in an adversarial synchronization and swarming model. *Physical Review E*, APS, v. 102, n. 3, p. 032607, 2020.

128 BELOVS, M.; LIVANOVIČS, R.; CĒBERS, A. Synchronized rotation in swarms of magnetotactic bacteria. *Physical Review E*, APS, v. 96, n. 4, p. 042408, 2017.

129   ADORJANI, B.; LIBAL, A.; REICHHARDT, C.; REICHHARDT, C. Motility induced phase separation and frustration in active matter swarmalators. *arXiv preprint arXiv:2309.10937*, 2023.

130   BLUM, N.; LI, A.; O'KEEFFE, K.; KOGAN, O. Swarmalators with delayed interactions. *Physical Review E*, APS, v. 109, n. 1, p. 014205, 2024.

131   KONGNI, S. J.; NGUEFOUE, V.; NJOUGOUO, T.; LOUODOP, P.; FERREIRA, F. F.; TCHITNGA, R.; CERDEIRA, H. A. Phase transitions on a multiplex of swarmalators. *Physical Review E*, APS, v. 108, n. 3, p. 034303, 2023.

132   GHOSH, S.; SAR, G. K.; MAJHI, S.; GHOSH, D. Antiphase synchronization in a population of swarmalators. *Physical Review E*, APS, v. 108, n. 3, p. 034217, 2023.

133   HAO, B.; ZHONG, M.; O'KEEFFE, K. Attractive and repulsive interactions in the one-dimensional swarmalator model. *Physical Review E*, APS, v. 108, n. 6, p. 064214, 2023.

134   BALCERZAK, M.; PIKUNOV, D.; DABROWSKI, A. The fastest, simplified method of lyapunov exponents spectrum estimation for continuous-time dynamical systems. *Nonlinear Dynamics*, Springer, v. 94, p. 3053–3065, 2018.

135   KRUK, N.; CARRILLO, J. A.; KOEPPL, H. Traveling bands, clouds, and vortices of chiral active matter. *Physical Review E*, APS, v. 102, n. 2, p. 022604, 2020.

136   CHILDS, L. M.; STROGATZ, S. H. Stability diagram for the forced kuramoto model. *Chaos: An Interdisciplinary Journal of Nonlinear Science*, AIP Publishing, v. 18, n. 4, 2008.

137   LÓPEZ, H. M.; GACHELIN, J.; DOUARCHE, C.; AURADOU, H.; CLÉMENT, E. Turning bacteria suspensions into superfluids. *Physical review letters*, APS, v. 115, n. 2, p. 028301, 2015.

138   QUILLEN, A.; PESHKOV, A.; WRIGHT, E.; MCGAFFIGAN, S. Metachronal waves in concentrations of swimming turbatrix aceti nematodes and an oscillator chain model for their coordinated motions. *Physical Review E*, APS, v. 104, n. 1, p. 014412, 2021.

139   LEVIS, D.; PAGONABARRAGA, I.; LIEBCHEN, B. Activity induced synchronization: Mutual flocking and chiral self-sorting. *Physical Review Research*, APS, v. 1, n. 2, p. 023026, 2019.

140   CAVAGNA, A.; GIARDINA, I.; GUCCIARDINO, M. A.; IACOMELLI, G.; LOMBARDI, M.; MELILLO, S.; MONACCHIA, G.; PARISI, L.; PEIRCE, M. J.; SPACCAPELO, R. Characterization of lab-based swarms of anopheles gambiae mosquitoes using 3d-video tracking. *Scientific Reports*, Nature Publishing Group UK London, v. 13, n. 1, p. 8745, 2023.

141   FACCHINELLI, L.; VALERIO, L.; LEES, R. S.; OLIVA, C. F.; PERSAMPIERI, T.; COLLINS, C. M.; CRISANTI, A.; SPACCAPELO, R.; BENEDICT, M. Q. Stimulating anopheles gambiae swarms in the laboratory: application for behavioural and fitness studies. *Malaria Journal*, Springer, v. 14, p. 1–9, 2015.

142   TOGASHI, Y. Modeling of nanomachine/micromachine crowds: interplay between the internal state and surroundings. *The Journal of Physical Chemistry B*, ACS Publications, v. 123, n. 7, p. 1481–1490, 2019.

143   ZHOU, C.; SUEMATSU, N. J.; PENG, Y.; WANG, Q.; CHEN, X.; GAO, Y.; WANG, W. Coordinating an ensemble of chemical micromotors via spontaneous synchronization. *ACS nano*, ACS Publications, v. 14, n. 5, p. 5360–5370, 2020.

144   CHEN, B.; TAN, H.; DING, M.; LIU, L.; WANG, S.; PENG, X.; TIAN, H.; JIANG, J.; GAO, J.; HUANG, W. et al. Nanorobot-mediated synchronized neuron activation. *ACS nano*, ACS Publications, v. 17, n. 14, p. 13826–13839, 2023.

APPENDIX A – Synchronization of Sakaguchi swarmalators

A.1 Abstract

Swarmalators are phase oscillators that cluster in space, like fireflies flashing on a swarm to attract mates. Interactions between particles, which tend to synchronize their phases and align their motion, decrease with the distance and phase difference between them, coupling the spatial and phase dynamics. In this work, we explore the effects of inducing phase frustration on a system of Swarmalators that move on a one-dimensional ring. Our model is inspired by the well-known Kuramoto-Sakaguchi equations. We find, numerically and analytically, the ordered and disordered states that emerge in the system. The active states, not present in the model without frustration, resemble states found previously in numerical studies for the 2D Swarmalators system. One of these states, in particular, shows similarities to turbulence generated in a flattened media. We show that all ordered states can be generated for any values of the coupling constants by tuning the phase frustration parameters only. Moreover, many of these combinations display multi-stability.

A.2 Introduction

Synchronization and swarming are emergent phenomena observed in various living systems. The former refers to the tendency of individuals' states to converge towards specific periodic behaviors and has been widely investigated using the Kuramoto [86,87] or the Stuart-Landau [80,88] models. The latter describes systems in which individuals tend to aggregate and align in space, as often observed in animals such as birds and fish [89,90]. Although the two behaviors have been spotted independently in nature, systems including the Japanese tree frogs [91] and the Quincke rollers [92], among others [93–95], suggest that synchronization and swarming also occur together. A model that couples both behaviors was recently proposed in [82] and the corresponding particles termed swarmalators.

The Swarmalators model [82] describes a system of particles characterized by internal phases θ_i and spatial positions $\vec{x}_i$. Phase and position dynamics coupled in such a way that phases tend to synchronize among nearby particles and velocities tend to align more easily among particles with synchronized phases. An instance of the model, for N

particles moving in a two-dimensional space, is described by

$$\dot{\vec{x}}_i = \frac{1}{N} \sum_{j \neq i}^{N} \left[\frac{\vec{x}_j - \vec{x}_i}{|\vec{x}_j - \vec{x}_i|} (1 + J \cos(\theta_j - \theta_i)) - \frac{\vec{x}_j - \vec{x}_i}{|\vec{x}_j - \vec{x}_i|^2} \right]$$
$$\dot{\theta}_i = \frac{K}{N} \sum_{j \neq i}^{N} \frac{\text{sen}(\theta_j - \theta_i)}{|\vec{x}_j - \vec{x}_i|}.$$

$$(A.1)$$

It has been shown that different collective states may emerge for specific sets of parameters K and J [82]. Previous work have also explored the system's behavior under external stimulus [96], variations on the nature of individual's interactions [97–101] and effects of thermal noise [102]. However, from an analytical perspective almost no progress has been made. Under this premise, O'Keeffe et. al [103] proposed a one-dimensional analogue of the model whose dynamics are governed by

$$\dot{x}_i = \frac{J}{N} \sum_j \text{sen}(x_j - x_i) \cos(\theta_j - \theta_i),$$
$$\dot{\theta}_i = \frac{K}{N} \sum_j \text{sen}(\theta_j - \theta_i) \cos(x_j - x_i),$$

$$(A.2)$$

and capture several features of Eqs. (A.1). This simpler model displays the emergence of several static collective states observed in the 2D system and, most importantly, can be treated analytically. Further work have also considered noisy interactions [102], distributed couplings [104], random pinning [105], and intrinsic oscillating frequencies [106].

The 1D Swarmalators model, however, cannot describe some of the active states displayed by the full 2D system. Even if some states of the 2D model are arranged in the form of an annulus, projecting it onto a 1D ring leaves out part of the dynamics that could be essential for the formation of the structure. On the other hand, the similarity of the 1D model with a pair of coupled Kuramoto equations, suggests that the expertise acquired from studying this famous synchronization model can be leveraged to analyze Swarmalators systems of this type. Here we propose a model of frustrated 1D swarmalators, based on the Sakaguchi-Kuramoto model [83], as a source of frustration that could compensate for the loss of freedom of the 1D system and potentially restore the active states observed in the 2D model. We call the corresponding particles *Sakaguchi Swarmalators*. We explore the effects of additional phase parameters to both the spatial and phase dynamics in Eqs. (A.2). This frustration differs from (and complements) the disorder produced by distributed couplings, studied by several authors for the Kuramoto model [86], and by O'Keeffe and Hong for the 1D Swarmalators model [104]. We will show that, indeed, frustration leads to coherent active states in 1D, similar to the ones found in the 2D setup. Additionally, it is worth mentioning that the new parameters of the Sakaguchi Swarmalators model have similarity with "offset terms" used in a recent numerical study of a modified 2D Swarmalators system [107].

We describe the modifications to the original 1D model in (Sec. A.3), introducing frustration as in the Kuramoto-Sakaguchi model. Then, in the same section, we present the different collective states obtained from numerical computations. In Sec. A.5, we present the stability analyses of states that show ordered configurations. The conditions obtained from the analytical computations allow us to picture the stability regions in the space of frustration parameters (Sec. A.6). Finally, in Sec. A.7 we sum up some concluding remarks.

A.3   The Sakaguchi Swarmalators model

Our modifications to the 1D Swarmalators model bring back the essential feature of the Kuramoto-Sakaguchi model: the introduction of disorder on a system intended to exhibit a coherent behavior [83]. The same idea was applied before to describe chimera states in self-propelled 2D particles [108]. In our model, however, the disorder affects both the spatial and phase components of each particle's dynamics. As described by the expressions

$$
\dot{x}_i = \frac{J}{N} \sum_j \text{sen}(x_j - x_i + \alpha) \cos(\theta_j - \theta_i + \beta),
$$
$$
\dot{\theta}_i = \frac{K}{N} \sum_j \text{sen}(\theta_j - \theta_i + \beta) \cos(x_j - x_i + \alpha)
$$

(A.3)

so that the disorder parameters α and β are incorporated to the system dynamics. Hence, if the system reaches coherence in phase ($\theta_j \approx \theta_i$) or space ($x_j \approx x_i$), the effects induced by α and β would lead to its disruption.

A.4   Equilibrium states

Numerical computation of Eqs. (A.3) allows us to get insights on its long term behavior. Snapshots of the system's collective behavior, after 10^4 time steps, are shown in Figures 9, 10, and 11. In all cases, the number of particles is $N = 500$ and the parameter J is set to 1. Thus, the control parameters are K, α, and β. In the figures we use the auxiliary parameters $\gamma^\pm = \alpha \pm \beta$, instead, since $\gamma^\pm$ will be relevant for the stability analyses in the next sections. Particles' positions and phases are initially distributed uniformly in ranges $-\pi$ to π. In the spatial pictures, shown in the top rows of Figures 9, 10, and 11, particles are positioned along the ring and colored according to their phases. The scatter plots, in the bottom row of Figures 9, 10, and 11, correspond to the spatial picture above and show the position-phase correlation for each particle. The states presented in Figure 9 demonstrate the convergence of particles to fixed values in phase and space. Once the particles reach these states, after a transient period, they remain there statically. Despite this feature, however, we observe clear differences in the position-phase coherence of each
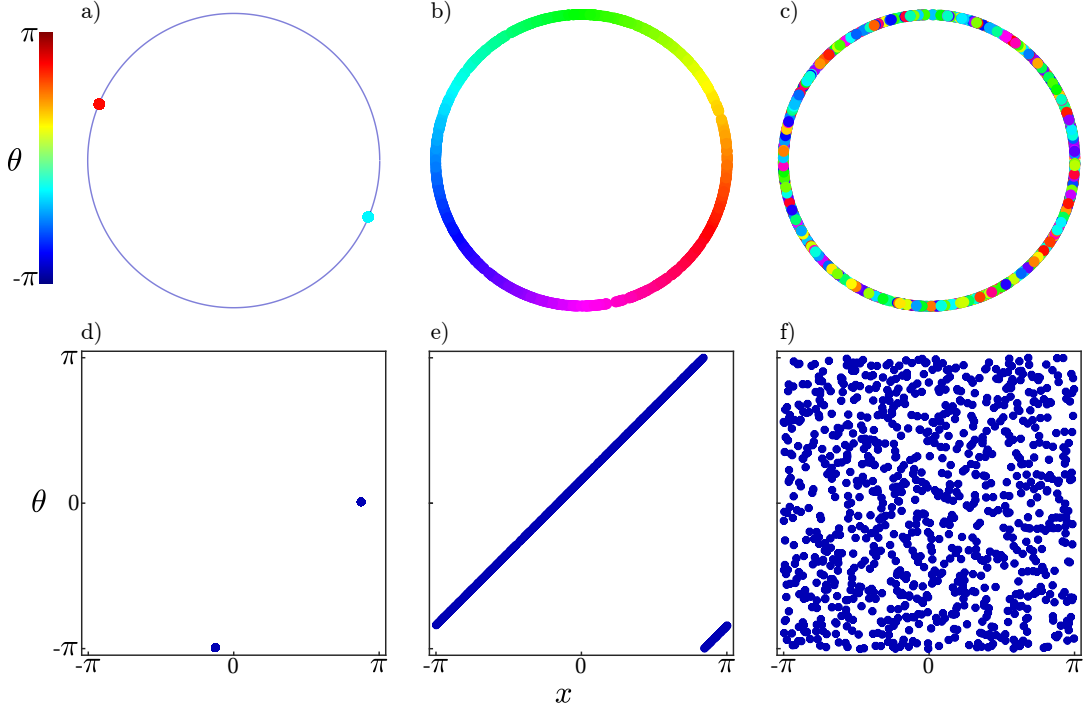
Figure 9 – Spatial behavior (top row) and position-phase correlations (bottom row) for the static states of the Sakaguchi Swarmalators model. ($K = 1$) is set for all the simulations, and (γ^+, γ^-) are set as a,d) $(0, 0)$ for the Static Synchronous, b,e) $(1.67, 0)$ for the Static Phase Wave, and c,f) $(1.8, 2)$ for the Static Asynchronous states.

case. The Static Synchronous state (Figures 9a and 9d) shows the formation of two clusters spaced, in phase and space, by a factor of π. Particles move to each cluster depending on their initial condition and synchronize with its cluster neighbors. In the Static Phase Wave state, (Figures 9b and 9e), particles are uniformly distributed along the ring. Moreover, each particle's phase is correlated with its position, implying that these are also distributed uniformly. The correlation shown in the figure is positive, however, variations in the initial conditions can change the behavior of the system so that the steady behavior leads to a negative correlation. The Static Asynchronous state (Figures 9c and 9d) shows that particles are distributed uniformly in phase and space. However, unlike the Static Phase Wave state, particles' positions and phases are uncorrelated.

Active analogues of the Static Synchronous and Static Phase Wave states are shown in Figure 10. In the Active Synchronous state (Figures 10a and 10d) the two clusters of particles, as described before for the Static Synchronous case, are rotating along the ring. Despite the rotation, the clusters preserve the spacing of π in position and phase. A similar effect is seen in the Active Phase Wave state (Figures 10b and 10e), where the uniformily distributed particles rotate while keeping the position-phase correlation. In Figures 10c and 10f, we introduce a new state where particles rotate around the ring while keeping a fixed pattern. In this state, particles cluster on a position-phase region,
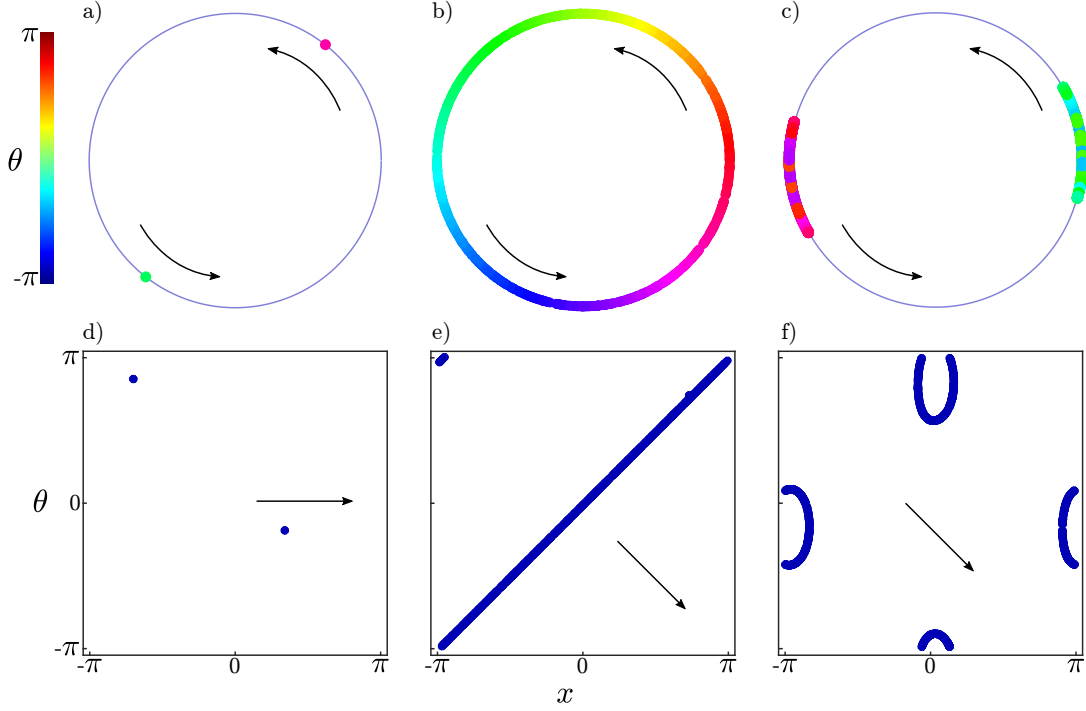
Figure 10 – Spatial behavior (top row) and position-phase correlations (bottom row) for the ordered active states of the Sakaguchi Swarmalators model. (K, γ^+, γ^-) are set as a,d) $(1, 1.3, 1.5)$ for the Active Synchronous, b,e) $(1, 2.5, 1.1)$ for the Active Phase Wave, and c,f) $(-5, 0.3, -3.1)$ for the Ring states. Arrows represent the translation direction of the particles.

in contrast to the Active Synchronous state, where particles cluster on two π-distanced points.

In Figure 11, we show three additional active states. Despite not being completely ordered these states still show the emergence of intriguing patterns. In the Noisy Active Phase Wave state (Figures 11a and 11d), particles move and initially form a correlated position-phase pattern. After some time, however, this coherence is destroyed and a dynamic behavior starts where distorted correlation appears and disappears continuously. The Active Asynchronous state (Figures 11b and 11e) is the active analogous to the Static Asynchronous state, shown in Figures 10c and 10e. In this state, however, particles jiggle and move randomly. The effects of this dynamic behavior, as better shown in the state's scatter plot, generate position-phase correlation in a non-uniformly distributed configuration. The last disordered state (Figures 11c and 11f) is named Turbulent and is unrelated to the previous ones. In this state, the particles move randomly along the ring without a specific position-phase coherence. However, as presented on its scatter plot, a recurrent pattern emerges where the particles' position-phase correlations generate vortices that rotate and move around while exchanging individuals.

The figures described in this section, obtained numerically, allow us to understand the coherent and incoherent behaviors of the Sakaguchi Swarmalators system. In
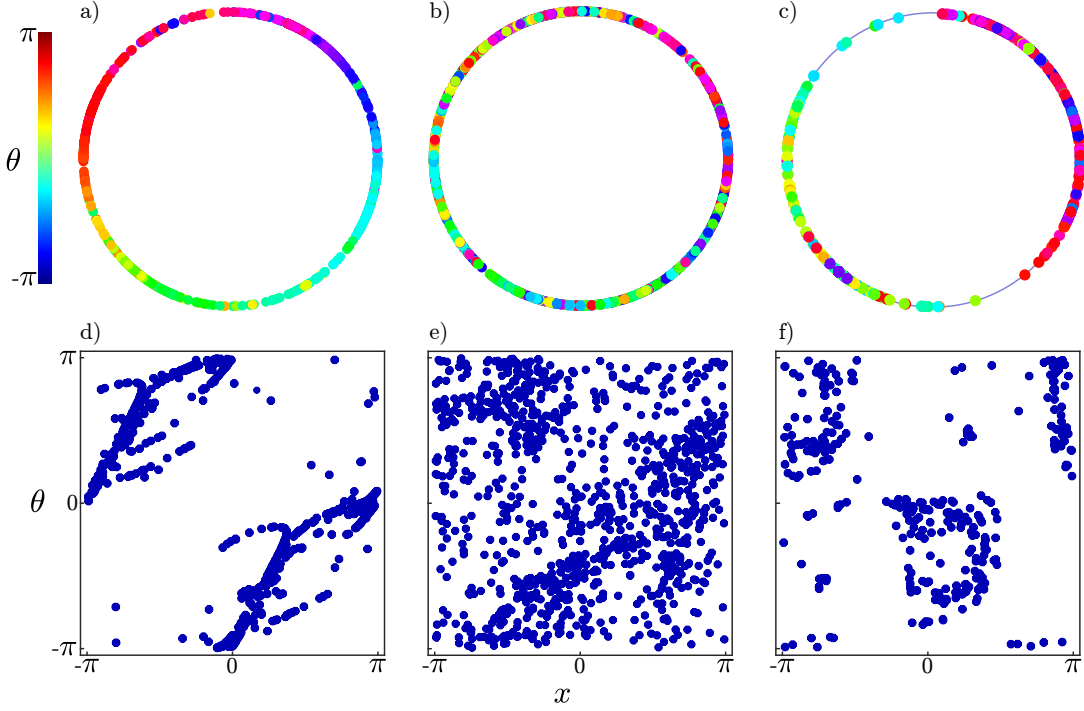
Figure 11 – Spatial behavior (top row) and position-phase correlations (bottom row) for the disordered active states of the Sakaguchi Swarmalators model. (K, γ^+, γ^-) are set as a,d) $(-0.2, 1.9, -1.4)$ for the Noisy Active Phase Wave, b,e) $(-1, 1.25, -0.25)$ for the Active Asynchronous, and c,f) $(-0.2, 3, -0.5)$ for the Turbulent states. In all cases, particles are in continuous motion.

the next section we explore the analytical features of the model, describing some of these states and their stability conditions.

A.5   Stability analyses

Following [103] we define $\xi_i = x_i + \theta_i$, $\eta_i = x_i - \theta_i$ and rewrite Eqs. (A.3) as

$$\dot{\xi}_i = \frac{J_+}{N} \sum_j \text{sen}(\xi_j - \xi_i + \gamma^+) + \frac{J_-}{N} \sum_j \text{sen}(\eta_j - \eta_i + \gamma^-),$$

$$\dot{\eta}_i = \frac{J_-}{N} \sum_j \text{sen}(\xi_j - \xi_i + \gamma^+) + \frac{J_+}{N} \sum_j \text{sen}(\eta_j - \eta_i + \gamma^-),$$

(A.4)

where $J_\pm = (J \pm K)/2$ and $\gamma^\pm = \alpha \pm \beta$. We also define the order parameters

$$S_+ e^{i\phi_+} = \frac{1}{N} \sum_j e^{i\xi_j},$$

$$S_- e^{i\phi_-} = \frac{1}{N} \sum_j e^{i\eta_j},$$

(A.5)

where the real values $S_\pm$ (ranging from 0 to 1) are coherence metrics associated with positive or negative correlations between particles' positions and phases. For instance, the

coherence of the Static Phase Wave state, shown in Figure 9b, is $(S_+, S_-) \approx (0, 1)$ due to the position-phase positive correlation of the particles. For the Static Asynchronous state, shown in Figure 9c, on the other hand, $S_\pm \approx 0$, since there is no correlation between particles' positions and phases.

A.5.1 Synchronous states

These states involve clustering and synchronization of the particles, that converge simultaneously to specific values in phase and space that can be static or dynamic. Setting $\xi_j = \xi_i = \xi$ and $\eta_j = \eta_i = \eta$ in Eqs. (A.4) we obtain the equilibrium trajectories

$$\xi = J_+\text{sen}(\gamma^+)t + J_-\text{sen}(\gamma^-)t + \xi_0,$$
$$\eta = J_-\text{sen}(\gamma^+)t + J_+\text{sen}(\gamma^-)t + \eta_0.$$

To analyze the stability of this solution, we add small perturbations $\delta\xi_i$ and $\delta\eta_i$ to each particle around the equilibrium trajectory and compute their dynamic behavior. The temporal evolution of the perturbations is described by

$$\delta\dot{\xi_i} = J^+ \cos(\gamma^+) \sum_j (\delta\xi_j - \delta\xi_i) + J^- \cos(\gamma^-) \sum_j (\delta\eta_j - \delta\eta_i)$$
$$\delta\dot{\eta_i} = J^- \cos(\gamma^+) \sum_j (\delta\xi_j - \delta\xi_i) + J^+ \cos(\gamma^-) \sum_j (\delta\eta_j - \delta\eta_i),$$
(A.6)

where $J^\pm = J_\pm/N$. These equations form a $2N \times 2N$ linear system which is evaluated in detail in Appendix A.8.1. The eigenvalues, that determine the stability of the equilibrium trajectory, are

$$\lambda_\pm^{SS} = -\frac{J_+}{2}\left(\cos(\gamma^+) + \cos(\gamma^-)\right) \pm \frac{1}{2}\left(J_+^2\left(\cos(\gamma^+) - \cos(\gamma^-)\right)^2 + 4J_-^2\cos(\gamma^+)\cos(\gamma^-)\right)^{1/2},$$
$$\lambda_0^{SS} = 0,$$
(A.7)

where $\lambda_\pm^{SS}$ have multiplicity $(N-1)$ each, and λ_0^{SS} has multiplicity 2. The superscript SS stands for Synchronous States.

For the particular case where $J = K$, and therefore $J_- = 0$, the non-zero eigenvalues are

$$\lambda_+^{SS(J=K)} = -J_+ \cos(\gamma^-),$$
$$\lambda_-^{SS(J=K)} = -J_+ \cos(\gamma^+),$$
(A.8)

and will be negative for $J_+ > 0$ when $\gamma^\pm \in [-\pi/2, \pi/2]$, and for $J_+ < 0$ when $\gamma^\pm \in [\pi/2, 3\pi/2]$. The stability regions for $J \neq K$ are more complicated due to the shape of the non-zero eigenvalues surfaces. We shown the stability regions in this case in the next section.

Before we close this subsection we note an interesting symmetry that appears for $J = 1$. In this specific case, $J_\pm = (K \pm 1)/2$, and considering $K^* = 1/K$, we get $J_\pm^* = \pm J_\pm/K$. Then, if we find $J_\pm^{*2}$ an plug it into Eqs. (A.7), we see that the non-zero eigenvalues will just be scaled as

$$\lambda_\pm^{SS*} = \frac{1}{K}\lambda_\pm^{SS}, \tag{A.9}$$

so the stability regions for K and $1/K$ are exactly the same.

A.5.2 Phase Wave states

Here the particles are distributed uniformly in space and phase but these variables are correlated. Also, they can move rigidly, keeping their relative positions and phases constant. These states are represented by $x_i = 2i\pi/N + x_0 + v_x t$ and $\theta_i = \pm 2i\pi/N + \theta_0 + v_\theta t$, where v_x and v_θ can be determined from Eqs. (A.4). The $\pm$ sign in θ_i depends on the type of position-phase correlation. We consider a negative correlation, so that the equilibrium trajectories must satisfy

$$\xi_i = J_+ \mathrm{sen}(\gamma^+)t + \xi_0,$$
$$\eta_i = J_- \mathrm{sen}(\gamma^+)t + \frac{4\pi i}{N} + \eta_0.$$

Substituting in Eqs. (A.4) we find $v_x + v_\theta = J_+ \mathrm{sen}\gamma^+$ and $v_x - v_\theta = J_- \mathrm{sen}\gamma^+$. To study the stability of this solution, we again add perturbations $\delta\xi_i$ and $\delta\eta_i$ to the equilibrium and find their dynamics. We obtain

$$\delta\dot{\xi}_i = J^+ \cos(\gamma^+) \sum_j (\delta\xi_j - \delta\xi_i) + J^- \sum_j \delta\eta_j \cos\left(\frac{4\pi}{N}(j - i) + \gamma^-\right),$$
$$\delta\dot{\eta}_i = J^- \cos(\gamma^+) \sum_j (\delta\xi_j - \delta\xi_i) + J^+ \sum_j \delta\eta_j \cos\left(\frac{4\pi}{N}(j - i) + \gamma^-\right). \tag{A.10}$$

The dynamics of the perturbations can again be arranged using a $2N \times 2N$ block matrix, and the stability of the system analyzed by its eigenvalues. A detailed derivation of the eigenvalues is shown in Appendix A.8.1. We obtain

$$\lambda_0^{nPW} = 0,$$
$$\lambda_1^{nPW} = -J_+ \cos(\gamma^+),$$
$$\lambda_{2\pm}^{nPW} = \frac{J_+}{2}\left(\frac{1}{2}e^{-i\gamma^-} - \cos(\gamma^+)\right) \pm \frac{1}{2}\left[J_+^2\left(\frac{1}{2}e^{-i\gamma^-} + \cos(\gamma^+)\right)^2 - 2J_-^2 e^{-i\gamma^-}\cos(\gamma^+)\right]^{1/2},$$
$$\lambda_{(N-2)\pm}^{nPW} = \frac{J_+}{2}\left(\frac{1}{2}e^{i\gamma^-} - \cos(\gamma^+)\right) \pm \frac{1}{2}\left[J_+^2\left(\frac{1}{2}e^{i\gamma^-} + \cos(\gamma^+)\right)^2 - 2J_-^2 e^{i\gamma^-}\cos(\gamma^+)\right]^{1/2},$$
$$\tag{A.11}$$

where λ_0^{nPW} and λ_1^{nPW} have multiplicities of 2 and $(N-6)$, respectively. The superscript *PW* stands for Phase Wave. Considering a positive position-phase correlation leads to slightly different eigenvalues. These differences, however, generate just a $\pi/2$ rotation of the stability regions (as will be shown in the next section). In Appendix A.8.1, we summarize the derivation of the eigenvalues for the positively correlated Phase Wave states.

For $J = K$ the non-zero eigenvalues are

$$\begin{aligned}
\lambda_1^{nPW(J=K)} &= -J_+ \cos(\gamma^+), \\
\lambda_{2+}^{nPW(J=K)} &= \frac{J_+}{2} e^{-i\gamma^-}, \\
\lambda_{2,(N-2)-}^{nPW(J=K)} &= -J_+ \cos(\gamma^+), \\
\lambda_{(N-2)+}^{nPW(J=K)} &= \frac{J_+}{2} e^{i\gamma^-},
\end{aligned} \tag{A.12}$$

and the regions where $\mathrm{Re}\{\lambda^{nPW(J=K)}\}$ are negative, for $J_+ > 0$ are $\gamma^+ \in [-\pi/2, \pi/2]$ and $\gamma^- \in [\pi/2, 3\pi/2]$, and for $J_+ < 0$ are $\gamma^+ \in [\pi/2, 3\pi/2]$ and $\gamma^- \in [-\pi/2, \pi/2]$. The regions for $J \neq K$, and for the positively correlated Phase Wave states are shown in the next section. Moreover, the symmetry $1/K \to K$ still applies for $J = 1$, and so does the scaling in Eq. (A.9). The stability regions for K and $1/K$ are, therefore, also the same for the Phase Wave states.

A.5.3 Asynchronous states

These states, such as the one shown in Figure 9c, are characterized by a uniform and uncorrelated distribution of particles in position and phase. To study their stability we take the limit of infinitely many oscillators and assume a continuum of particles described by the density function $\rho(x, \theta, t)\mathrm{d}x\mathrm{d}\theta$, which gives the fraction of particles lying between $x + \mathrm{d}x$ and $\theta + \mathrm{d}\theta$ at time t [109]. The normalization condition for the density is

$$\int_0^{2\pi} \int_0^{2\pi} \rho(x, \theta, t)\mathrm{d}x\mathrm{d}\theta = 1, \tag{A.13}$$

which allows us to rewrite the order parameters, introduced in Eqs. (A.5), as

$$S_\pm e^{i\phi_\pm} = \int_0^{2\pi} \int_0^{2\pi} e^{i(x\pm\theta)}\rho(x, \theta, t)\mathrm{d}x\mathrm{d}\theta. \tag{A.14}$$

Given that the description of this state is more intuitive in terms of x and θ, we use Eqs. (A.3) for its analysis. To reduce the size of the equations, however, we keep using the parameters ξ and η as defined before. Then, the equations of motion give the velocity vector field governing the behavior of the system:

$$\begin{aligned}
\dot{x} &= \frac{J}{2}S_+\mathrm{sen}(\phi_+ - \xi + \gamma^+) + \frac{J}{2}S_-\mathrm{sen}(\phi_- - \eta + \gamma^-) \\
\dot{\theta} &= \frac{K}{2}S_+\mathrm{sen}(\phi_+ - \xi + \gamma^+) - \frac{K}{2}S_-\mathrm{sen}(\phi_- - \eta + \gamma^-).
\end{aligned} \tag{A.15}$$

The temporal evolution of the density $\rho(x, \theta, t)$ is described by the continuity equation

$$\frac{\partial \rho}{\partial t} + \nabla(\rho \vec{v}) = 0, \tag{A.16}$$

where $\vec{v} = (\dot{x}, \dot{\theta})$ as in Eqs. (A.15). The uniform density $\rho_0 = \pi^{-2}/4$ with $S_+ = S_- = 0$ is an equilibrium incoherent state and its stability can be studied by perturbing it as $\rho = \rho_0 + \delta\rho$ and analyzing the perturbation dynamics. The perturbation analysis is detailed in Appendix A.8.3, and it leads to the derivation of the eigenvalues

$$\begin{aligned}
\lambda_{1\pm}^{oAS} &= \frac{J_+}{8\pi^2} e^{\pm i\gamma^+}, \\
\lambda_{2\pm}^{oAS} &= \frac{J_+}{8\pi^2} e^{\pm i\gamma^-}.
\end{aligned} \tag{A.17}$$

The Static Asynchronous state will be stable when the real part of these eigenvalues are negative, that is, for $J_+ > 0$ when $\gamma^\pm \in [\pi/2, 3\pi/2]$, and for $J_+ < 0$ when $\gamma^\pm \in [-\pi/2, \pi/2]$.

A.6 Stability diagrams

The analytical results obtained in the previous section can be summarized with graphic representations of the Sakaguchi Swarmalators' stability regions spanned for $\gamma^\pm \in [-\pi, \pi]$. We fix $J = 1$ in all diagrams, as this specific setup allows us to observe the stability symmetry expected when using K and $1/K$ (Figures 12b, 12c, 12e, and 12f).

The simplest case, where $J = K$, is shown in Figure 12a. As calculated in Eqs. (A.8), (A.12), and (A.17), the regions where each state emerges are just complementing squares. However, for $K > 0$ and different from J (Figures 12b and 12c), the Phase Wave squared regions deform giving rise to the formation of stability regions that intersect. These are regions of multi-stability, where the system converges to either the Synchronous or Phase Wave states, depending on the initial conditions. Once K becomes negative, the Synchronous square regions, depicted for $J \geqslant K$, split into four triangles, Figs. 12e and 12f, that split again for $K < -J$, Figs. 12g, and 12h. Even more interesting is the behavior of the Phase Wave regions, which for K approaching $-J$ from the right form intersecting $\pi/2$-rotated stripes (Figure 12e) that, when K increases towards 0, become fully intersected circles (Figure 12f). Similarly, the split of the Synchronous square and the Phase Wave stripes, which become circles, are found when K is set below $-J$ (Figures 12g and 12h). Despite the similarities, however, these stability regions are π-translated from the $-J < K < 0$ regions described before, in both the γ^- and γ^+ axes. We note that no such multi-stable regions exist in the Kuramoto-Sakaguchi model, suggesting that they depend on the interplay between the two degrees of freedom θ and x.

A special case takes place when $K = -J$, which corresponds to $J_+ = 0$, and leads to the vanishing of negative eigenvalues in all states. Under these circumstances,

the system exhibits the Active Asynchronous state, shown in Figure 11b. It is worth noting that, for these parameters, Eqs. (A.2) reduce to a Hamiltonian system with $H = (J/2N) \sum_{i,j} \text{sen}(x_j - x_i)\text{sen}(\theta_j - \theta_i)$. However, for frustration parameters $(\alpha, \beta) \neq 0$, the system loses the Hamiltonian structure and, therefore, a constant of motion. The stability regions when $K = 0$ are shown in Figure 12d, and, despite these appearing to be well-defined, their nature is very susceptible to small numerical changes. The Noisy Phase Wave and Turbulent states (introduced in Figures 11a and 11c) are also found in the stability diagrams, as pointed by red markers in Figures 12e, 12f, 12g, and 12h. These, given their disordered nature, do not belong to any of the stable state's regions but are positioned in the blank spaces. Finally, the intriguing ring state, introduced in Figure 10c, turns out to be an intermediate state when entering the Synchronous states' stable regions (as depicted by the blue star in Figure 12g), which gives meaning to its clustered behavior. This state allows us to remark that, at the boundaries, linear stability analysis is not enough to decide the nature of the equilibrium.

In Figure 13, we show heatmaps that complement the stability diagrams, presented in Figure 12, for the case where $J = K$. Each diagram is obtained for a system of $N = 500$ particles at its state after 10^4 time steps. Intensities are positioned according to specific values of $\gamma^{\pm}$ used for the computation. In Figures 13a and 13b, these correspond to S_+ and S_-, respectively, calculated using Eqs. (A.5). For Figure 13c, we use the additional parameter $S_v = 1/N \left| \sum_j \dot{x}_j \right|$, which is an indicator of the average velocity in the system.

Two main observations can be made by contrasting Figures 12a and 13. Firstly, as shown in the respective $S_{\pm}$ heatmaps, we can identify regions where the system converges to positively or negatively correlated states, which may represent either the Synchronous or Phase Wave states. Secondly, although convergence to any stable state can be proven by the eigenvalues, the definitions of ξ and η used for the stability analyses do not guarantee whether the system is static or active, even when analyzing $S_{\pm}$. However, the use of S_v provides additional information that allows us to overcome these limitations. As shown in Figure 13c, clear partitions consistent with the regions in Figure 12a are displayed, and intensities reveal the velocity dependence on $\gamma^{\pm}$, which is coherent with the equilibrium trajectories defined in Section A.5 for the Synchronous and Phase Wave states.

A.7 Discussion

We studied the effects of introducing frustration on a 1D Swarmalators system. Motivated by the work of Sakaguchi [83], we modified the original system introduced in [103], by including frustration parameters intended to break the coherence of the system in both position and phase spaces.
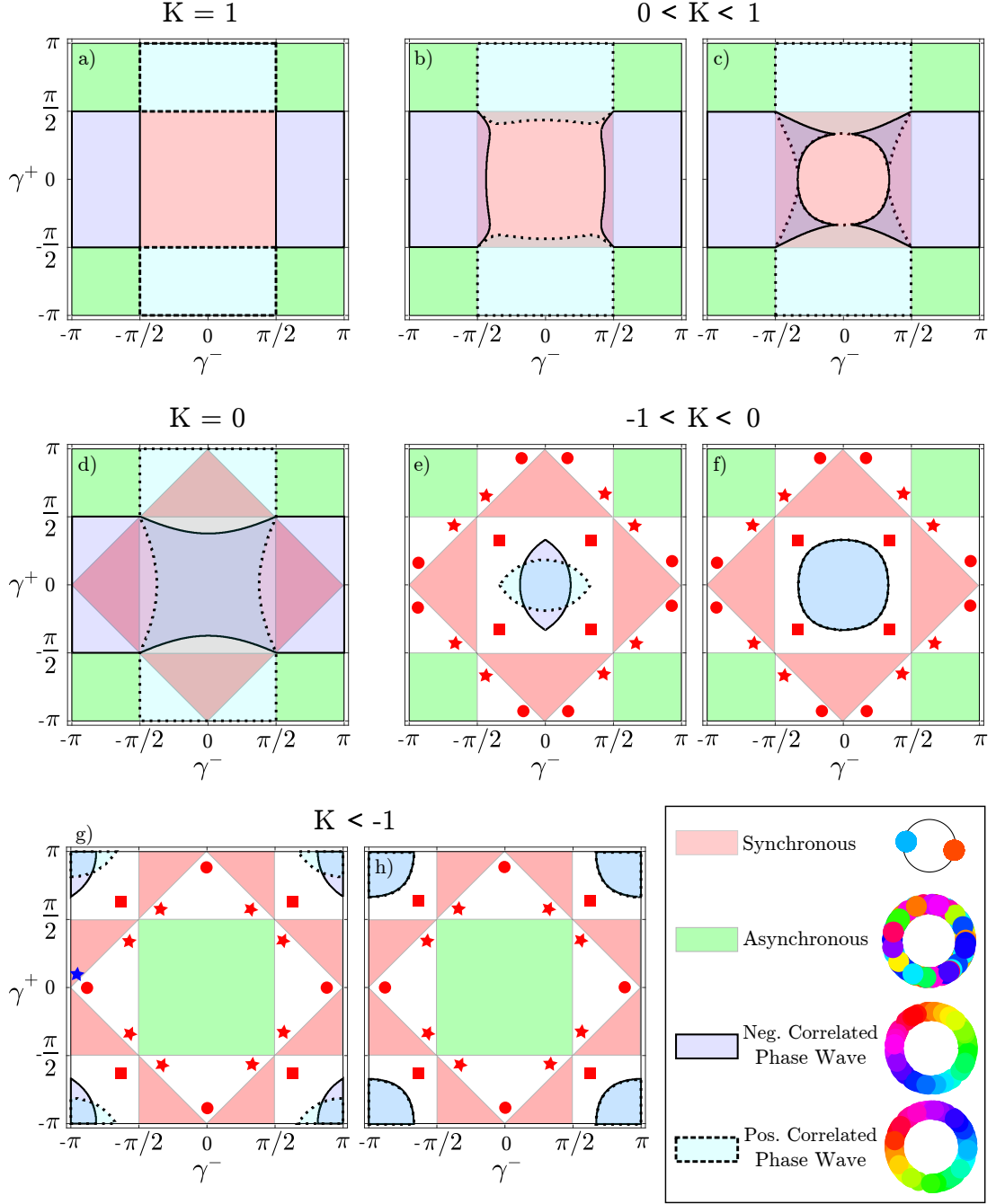
Figure 12 – Stability regions computed using the eigenvalues obtained from the perturbation analyses. All figures were obtained for $J = 1$ and $N = 500$. In b), the diagram shows the regions for both $K = 1/5$ and $K = 5$. Similarly, in c), the diagram corresponds to both $K = 1/500$ and $K = 500$. In e) and f), $K = -1/5$ and $K = -1/500$, respectively. And, in g) and h), $K = -5$ and $K = -500$, respectively. Red circles, stars and squares are positioned in regions where states Turbulent, Noisy Active Phase Wave, and a combination of these two emerge, respectively. The blue star in g) corresponds to one instance of Ring state.

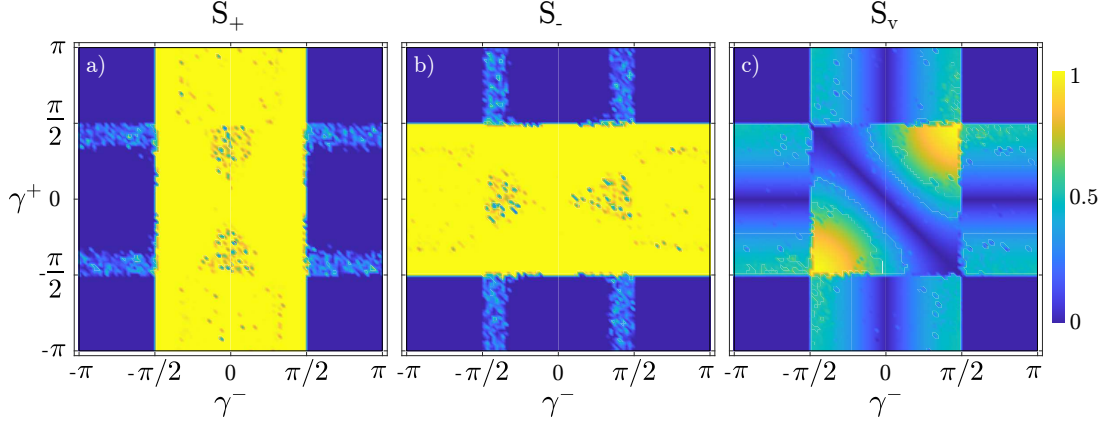Figure 13 – Order parameter heatmaps for $J = K = 1$ and $N = 500$, after 10^4 time steps. Each intensity corresponds to the value of the respective order parameter for specific (γ^+, γ^-) values. The diagrams show a) positive and b) negative position-phase correlation regions, and c) the average velocities.

The most striking feature of the model is the emergence of active states for non-zero frustration parameters. These states remind us of the ones found in the 2D Swarmalators model [82], that still lack a complete analytical explanation. In our model, however, we were able to find analytical solutions for the stability regions of each ordered state, independent of its static or active nature. Additionally, numerical computations allowed us to find regions where disordered active states emerge. In these states, despite the incoherent behavior exhibited by the particles, clear position-phase patterns can still be observed, which suggests that their analytical study could also be performed using different tools.

From the stability analyses we see that, in contrast to the original 1D Swarmalators model, the frustration parameters provide us flexibility to find ordered states for any fixed (J, K) values. That is, for a specific (J, K) setup, we can find Synchronous, positively or negatively correlated Phase Wave, or Asynchronous states just by tuning the values of $\gamma^\pm$. The disordered states, however, have been spotted only for $K < 0$. Even more exotic is the emergence of the Active Asynchronous case, which shows up only when $J = -K$.

Although Eqs. (A.3) have been defined in terms of an internal phase θ and a spatial coordinate x, we can think of the phase variable as another periodic spatial coordinate y, so that the scatter plots in Figures 9, 10, and 11 could represent particles' positions in the periodic Cartesian plane (a torus). The Active Asynchronous and Turbulent states are then similar to the patterns displayed by chiral rollers in [92] or ram semen in [110]. The turbulent state, in particular, is of specific interest for future studies, as it shows the emergence of vortices and eddy-like structures even for finite number of particles. We can point out, in this state, that the emergence of coherently behaved clusters, moving on a sea of incoherently behaved particles, portray a signature of chimeric

behavior. That relates our work with the emergence of chimeras, depicted in [108], for populations of self-propelled Kuramoto-like particles, also triggered by the addition of a phase lag parameter. Moreover, under a Cartesian setup, our results can also be extended to swarming-only systems whose position degrees of freedom interact.

An interesting take on the Sakaguchi Swarmalators model would be to consider asymmetrical frustrations (i.e. parameters affecting only the sines or cosines), or even considering distributed couplings and frustrations, as done in [111] for the Kuramoto model. In general, since the Kuramoto-Sakaguchi model and the concept of frustration have been widely studied [112–115], the study of Sakaguchi Swarmalators can be expanded following these ideas.

A.8 Appendix A1

A.8.1 Eigenvalues for coherent states

The stability calculations, described in subsections A.5.1 and A.5.2, show that perturbation dynamics can be arranged as

$$\dot{\vec{\delta}}_* = \mathbf{R}\vec{\delta}_*, \tag{A.18}$$

where, for each system's state, the vector $\vec{\delta}_*$ is composed of the individual perturbations $\delta\xi_i$ and $\delta\eta_i$, and

$$\mathbf{R} = \begin{bmatrix} \mathbf{R_{11}} & \mathbf{R_{12}} \\ \mathbf{R_{21}} & \mathbf{R_{22}} \end{bmatrix},$$

is a matrix of circulant blocks. The structure of $\mathbf{R}$ allows us to find its eigenvalues λ for all states, following the general procedure described below.

The eigenvalues are solutions of the equation

$$\det(\mathbf{R} - \lambda\mathbf{I_{2N}}) = 0,$$

where $\mathbf{I_{2N}}$ is the identity matrix of dimension $2N$. However, since $[\mathbf{R_{11}}, \mathbf{R_{21}}] = 0$ holds for both the Synchronous and Phase Wave cases, we rewrite the equation for the determinant as

$$\det(\mathbf{R} - \lambda\mathbf{I_{2N}}) = \det(\mathbf{M}),$$

where $\mathbf{M} = (\mathbf{R_{11}} - \lambda\mathbf{I_N})(\mathbf{R_{22}} - \lambda\mathbf{I_N}) - \mathbf{R_{21}}\mathbf{R_{12}}$ is also circulant. Then, the determinant of $\mathbf{M}$ can be computed using the general solution for circulant matrices

$$\det(\mathbf{M}) = \prod_{k=0}^{N-1} \left(M_{11} + M_{12}\zeta^k + \cdots + M_{1N}\zeta^{(N-1)k} \right), \tag{A.19}$$

where ζ is a primitive N-th root of unity, and the eigenvalues λ are found by equating the resulting equations inside the parenthesis to zero.

In the next subsections, we describe the solution to the eigenvalue problems for the Synchronous and Phase Wave states using the procedure described above. In each of these states, the blocks composing $\mathbf{R}$ have different structures that, however, can be considered special instances of circulant matrices. To differentiate between Synchronous and Phase Wave states, we use respectively the superscripts ^{SS} and ^{PW} on matrices and their elements. Since the Phase Wave state has two instances, we add the letters n and p in front of the superscripts to differentiate according to the negative or positive nature of the position-phase correlation. Additionally, to reduce the size of some expressions, we use s_* and c_* to represent $\text{sen}(*)$ and $\cos(*)$ functions, respectively.

A.8.1.1 Synchronous states

Arranging Eqs. (A.6) as Eq. (A.18) leads to a matrix $\mathbf{R}^{SS}$ composed by blocks

$$\mathbf{R}^{SS}_{11} = J^+ \cos(\gamma^+)\mathbf{R}_\dagger,$$
$$\mathbf{R}^{SS}_{12} = J^- \cos(\gamma^-)\mathbf{R}_\dagger,$$
$$\mathbf{R}^{SS}_{21} = J^- \cos(\gamma^+)\mathbf{R}_\dagger,$$
$$\mathbf{R}^{SS}_{22} = J^+ \cos(\gamma^-)\mathbf{R}_\dagger,$$

where

$$\mathbf{R}_\dagger = \begin{pmatrix} 1-N & 1 & \cdots & 1 \\ 1 & 1-N & \cdots & 1 \\ \vdots & \vdots & \ddots & \vdots \\ 1 & 1 & \cdots & 1-N \end{pmatrix}.$$

The composition of the block matrix $\mathbf{R}^{SS}$ allows us to infer that the off-diagonal terms of $\mathbf{M}^{SS}$ will all be the same. Thus, the only relevant elements to calculate $\det(\mathbf{M})$ are

$$M^{SS}_{11} = \lambda^2 - \lambda J^+(1-N)(c_{\gamma^-} + c_{\gamma^+}) +$$
$$N(1-N)c_{\gamma^+}c_{\gamma^-}(J^{-2} - J^{+2}),$$
$$M^{SS}_{12} = -\lambda J^+(c_{\gamma^-} + c_{\gamma^+}) + Nc_{\gamma^+}c_{\gamma^-}(J^{-2} - J^{+2}),$$

and Eq. (A.19) can be rewritten as

$$\det(\mathbf{M}^{SS}) = \prod_{k=0}^{N-1} \left(M^{SS}_{11} + M^{SS}_{12} \sum_{r=1}^{N-1} \zeta^{rk} \right), \tag{A.20}$$

where

$$\sum_{r=1}^{N-1} \zeta^{rk} = -1$$

for $k \neq 0$.

Solving Eq. (A.20) leads to the product of N quadratic equations, where $N-1$ of them are replicas. Equating this product to zero allows us to get the eigenvalue expressions shown in Eqs. (A.7).

A.8.1.2 Negatively correlated Phase Wave states

For these states, obtain the blocks

$$\mathbf{R}_{11}^{nPW} = J^+ \cos(\gamma^+)\mathbf{R}_\dagger,$$
$$\mathbf{R}_{12}^{nPW} = J^- \mathbf{R}_*^-,$$
$$\mathbf{R}_{21}^{nPW} = J^- \cos(\gamma^+)\mathbf{R}_\dagger,$$
$$\mathbf{R}_{22}^{nPW} = J^+ \mathbf{R}_*^-,$$

where

$$\mathbf{R}_*^\pm = \begin{pmatrix} \cos(\gamma^\pm) & \cos\left(4\pi\dfrac{1}{N} + \gamma^\pm\right) & \cdots & \cos\left(4\pi\dfrac{N-1}{N} + \gamma^\pm\right) \\ \cos\left(4\pi\dfrac{N-1}{N} + \gamma^\pm\right) & \cos(\gamma^\pm) & \cdots & \cos\left(4\pi\dfrac{N-2}{N} + \gamma^\pm\right) \\ \vdots & \vdots & \ddots & \vdots \\ \cos\left(4\pi\dfrac{1}{N} + \gamma^\pm\right) & \cos\left(4\pi\dfrac{2}{N} + \gamma^\pm\right) & \cdots & cos(\gamma^\pm) \end{pmatrix}.$$

Although we use only $\mathbf{R}_*^+$ to describe the $\mathbf{R}^{nPW}$ blocks, the matrix $\mathbf{R}_*^-$ will be used in the next subsection when describing the $\mathbf{R}^{pPW}$ blocks corresponding to the positive correlated Phase Wave states.

The blocks in $\mathbf{R}^{nPW}$ have different off-diagonal elements, which make the structure of $\mathbf{M}^{nPW}$ less intuitive. In this case the elementz needed to compute the determinant are

$$M_{11}^{nPW} = \lambda^2 - \lambda J^+ \left[c_{\gamma^-} + (1-N)c_{\gamma^+}\right] + N\left(J^{-2} - J^{+2}\right)c_{\gamma^+}c_{\gamma^-},$$

$$M_{1(r+1)}^{nPW} = -\lambda J^+ \left[\cos\left(\frac{4\pi}{N}r + \gamma^-\right) + c_{\gamma^+}\right] + N\left(J^{-2} - J^{+2}\right)c_{\gamma^+}\cos\left(\frac{4\pi}{N}r + \gamma^-\right),$$

and Eq. (A.19) can be rewritten as

$$\det(\mathbf{M}^{nPWS}) = \prod_{k=0}^{N-1}\left(M_{11}^{nPW} + \sum_{r=1}^{N-1} M_{1(r+1)}^{nPW}\zeta^{rk}\right). \tag{A.21}$$

Setting Eq. (A.21) to zero should return the eigenvalues shown in Eqs.(A.11). However, since elements $M_{1(r+1)}^{nPW}$ are all different, this solution is a bit more intricate. In Appendix A.8.2, we show the simplification of Eq. (A.21) that allows us to get analytical solutions for the eigenvalues.

A.8.1.3 Positively correlated Phase Wave states

We start by summarizing the perturbation analysis since this was removed from the main text for the sake of clarity. For the Phase Wave states that exhibit a positive position-phase correlation, the equilibrium trajectories are

$$\xi_i = J_- \text{sen}(\gamma^-)t + \frac{4\pi i}{N} + \xi_0,$$

$$\eta_i = J_+ \text{sen}(\gamma^-)t + \eta_0.$$

Adding perturbations to the equilibrium solutions we obtain

$$\delta\dot{\xi}_i = J^- c_{\gamma^-} \sum_j (\delta\eta_j - \delta\eta_i) + J^+ \sum_j \delta\xi_j C_{ij+},$$

$$\delta\dot{\eta}_i = J^+ c_{\gamma^-} \sum_j (\delta\eta_j - \delta\eta_i) + J^- \sum_j \delta\xi_j C_{ij+},$$

where $C_{ij+} = \cos\left(\frac{4\pi}{N}(j-i) + \gamma^+\right)$. This can be arranged in blocks

$$\mathbf{R}_{11}^{pPW} = J^+ \mathbf{R}_*^+,$$

$$\mathbf{R}_{12}^{pPW} = J^- \cos(\gamma^-)\mathbf{R}_\dagger,$$

$$\mathbf{R}_{21}^{pPW} = J^- \mathbf{R}_*^+,$$

$$\mathbf{R}_{22}^{pPW} = J^+ \cos(\gamma^-)\mathbf{R}_\dagger.$$

Despite the differences between $\mathbf{R}^{nPW}$ and $\mathbf{R}^{pPW}$, elements of $\mathbf{M}^{nPW}$ and $\mathbf{M}^{pPW}$ differ only by a swap of γ^+ and γ^-. Thus, we find

$$M_{11}^{pPW} = \lambda^2 - \lambda J^+ \left[(1-N)c_{\gamma^-} + c_{\gamma^+}\right] + N\left(J^{-2} - J^{+2}\right)c_{\gamma^+}c_{\gamma^-},$$

$$M_{1(r+1)}^{pPW} = -\lambda J^+ \left[c_{\gamma^-} + \cos\left(\frac{4\pi}{N}r + \gamma^+\right)\right] + N\left(J^{-2} - J^{+2}\right)\cos\left(\frac{4\pi}{N}r + \gamma^+\right)c_{\gamma^-}.$$

Then, $\det(\mathbf{M}^{pPW})$ has the same form of Eq. (A.21) and it can be solved using the simplification shown in Appendix A.8.2. The solution leads to the eigenvalues

$$\lambda_0^{pPW} = 0,$$

$$\lambda_1^{pPW} = -J_+ \cos(\gamma^-),$$

$$\lambda_{2\pm}^{pPW} = \frac{J_+}{2}\left(\frac{1}{2}e^{-i\gamma^+} - \cos(\gamma^-)\right) \pm \frac{1}{2}\left[J_+^{\,2}\left(\frac{1}{2}e^{-i\gamma^+} + \cos(\gamma^-)\right)^2 - 2J_-^{\,2}e^{-i\gamma^+}\cos(\gamma^-)\right]^{1/2},$$

$$\lambda_{(N-2)\pm}^{pPW} = \frac{J_+}{2}\left(\frac{1}{2}e^{i\gamma^+} - \cos(\gamma^-)\right) \pm \frac{1}{2}\left[J_+^{\,2}\left(\frac{1}{2}e^{i\gamma^+} + \cos(\gamma^-)\right)^2 - 2J_-^{\,2}e^{i\gamma^+}\cos(\gamma^-)\right]^{1/2}.$$

$$\text{(A.22)}$$

A.8.2 Simplification

We are interested in finding the solutions of a quadratic equation of the form

$$\lambda^2 + \lambda\phi + \omega = 0,$$

where, from Eq. (A.21),

$$\phi = -J^+ \left[c_{\gamma^-} + c_{\gamma^+} \left(1 - N + \sum_{r=1}^{N-1} \zeta^{rk} \right) + \sum_{r=1}^{N-1} \zeta^{rk} \cos \left(\frac{4\pi}{N} r + \gamma^- \right) \right],$$

$$\omega = N(J^{-2} - J^{+2}) c_{\gamma^+} \left[c_{\gamma^-} + \sum_{r=1}^{N-1} \zeta^{rk} \cos \left(\frac{4\pi}{N} r + \gamma^- \right) \right].$$

We expand the sum in the right hand side of these equations as

$$\sum_{r=1}^{N-1} \zeta^{rk} \cos \left(\frac{4\pi}{N} r + \gamma^- \right) = \frac{1}{2} e^{i\gamma^-} \sum_{r=1}^{N-1} e^{ir(4\pi + 2\pi k)/N}$$

$$+ \frac{1}{2} e^{-i\gamma^-} \sum_{r=1}^{N-1} e^{-ir(4\pi - 2\pi k)/N}.$$

Then, for $k \neq 2$,

$$\phi = \begin{cases} 0, & \text{if } k = 0 \\ J_+ c_{\gamma^+}, & \text{otherwise} \end{cases},$$

$$\omega = 0,$$

which lead to pairs of eigenvalues where one of them is real and the other one is zero, or both are zero ($k = 0$). For $k = 2$,

$$\phi = -J_+ \left(\frac{1}{2} e^{-i\gamma^-} - c_{\gamma^+} \right),$$

$$\omega = \frac{1}{2} e^{-i\gamma^-} \left(J_-^{\,2} - J_+^{\,2} \right) c_{\gamma^+},$$

and $k = (N - 2)$,

$$\phi = -J_+ \left(\frac{1}{2} e^{i\gamma^-} - c_{\gamma^+} \right),$$

$$\omega = \frac{1}{2} e^{i\gamma^-} \left(J_-^{\,2} - J_+^{\,2} \right) c_{\gamma^+},$$

which lead to pairs of complex conjugate eigenvalues.

A.8.3 Perturbation analysis of incoherent states

Incoherent states are characterized by $S_\pm = 0$ and, therefore, $\vec{v} = (\dot{x}, \dot{\theta}) = \vec{0}$. Thus, the homogeneous density $\rho_0 = \pi^{-2}/4$ is a static solution of the continuity equation (A.14).

Adding a small perturbation to the equilibrium state, $\rho = \rho_0 + \delta\rho$, and using Eq. (A.16), we find that the temporal evolution of the perturbed state is governed by

$$\frac{\partial}{\partial t}\delta\rho = -\nabla(\delta\rho)\,\vec{v}, \tag{A.23}$$

where, from Eq. (A.13)

$$\int_0^{2\pi}\int_0^{2\pi}\delta\rho(x,\theta,t)\mathrm{d}x\mathrm{d}\theta = 0. \tag{A.24}$$

To first order in $\delta\rho(x,\theta,t)$, we find that

$$S_\pm^1 e^{\mathrm{i}\phi_\pm} = \int_0^{2\pi}\int_0^{2\pi} e^{\mathrm{i}(x\pm\theta)}\delta\rho(x,\theta,t)\mathrm{d}x\mathrm{d}\theta, \tag{A.25}$$

which leads to

$$\frac{\partial}{\partial t}\delta\rho = \frac{J_+}{4\pi^2}\left(S_+^1\cos(\phi_+ - \xi + \gamma^+)\right. \\ \left. + S_-^1\cos(\phi_- - \eta + \gamma^-)\right). \tag{A.26}$$

Expanding $\delta\rho$ in Fourier series

$$\delta\rho = \sum_{m,n} f_{m,n}(t)e^{\mathrm{i}(mx+n\theta)}, \tag{A.27}$$

and comparing with Eq. (A.26) we see that the only relevant terms are $f_{\pm1,\pm1}$. We obtain

$$\dot{f}_{1,1}(t) = \frac{J_+}{8\pi^2}e^{-\mathrm{i}\gamma^-}f_{1,1}(t),$$
$$\dot{f}_{-1,1}(t) = \frac{J_+}{8\pi^2}e^{\mathrm{i}\gamma^-}f_{-1,1}(t),$$
$$\dot{f}_{1,-1}(t) = \frac{J_+}{8\pi^2}e^{-\mathrm{i}\gamma^+}f_{1,-1}(t),$$
$$\dot{f}_{-1,-1}(t) = \frac{J_+}{8\pi^2}e^{\mathrm{i}\gamma^+}f_{-1,-1}(t). \tag{A.28}$$

Finally, writting $f(t) = \bar{f}e^{t\lambda}$, we can solve Eqs. (A.28) to get the eigenvalues shown in Eqs. (A.17).

APPENDIX B – Order, chaos, and dimensionality transition in a system of swarmalators

B.1 Abstract

Similar to sperm, where individuals self-organize in space while also striving for coherence in their tail swinging, several natural and engineered systems exhibit the emergence of swarming and synchronization. The arising and interplay of these phenomena have been captured by collectives of hypothetical particles named swarmalators, each possessing a position and a phase whose dynamics are affected reciprocally and also by the space-phase states of their neighbors. In this work, we introduce a solvable model of swarmalators able to move in two-dimensional spaces. We show that several static and active collective states can emerge and derive necessary conditions for each to show up as the model parameters are varied. These conditions elucidate, in some cases, the displaying of multistability among states. Notably, in the active regime, the system exhibits hyperchaos, maintaining spatial correlation under certain conditions and breaking it under others on what we interpret as a dimensionality transition.

B.2 Introduction

Swarming and synchronization are emergent phenomena observed in various natural systems. Swarming, more noticeable due to its occurrence in physical space, is evidenced in groups of fishes, birds, insects, bacteria, among others [8,66–73]. Synchronization, sometimes less apparent due to its nature, is observed in both living and non-living systems, including groups of humans, frogs, heart cells, neurons, among others [16,74–79,116]. From a theoretical standpoint, both phenomena have been extensively studied using distinct frameworks based on well-known models named after Kuramoto [21], Stuart-Landau [80], Couzin [81], and Vicsek [11]. In these models, single particles are represented by their positions or by periodic internal degrees of freedom dubbed phases. Then, individuals' spatial self-organization gives rise to swarming and, in case of phase coherence, to synchronization.

Despite the success in studying swarming and synchronization independently, a significant step up has taken place recently, influencing both fields. A singular type of particles, named swarmalators, have been introduced in [82] such that, collectively, these can synchronize and swarm as their spatial and phase dynamics interplay. Several

systems where individuals' phases influence their positions and vice versa have been spotted in nature. These include magnetic quincke rollers [92], sperm [95, 117, 118], starfish embryos [94], tree frogs [91], nematodes [119, 120], and more [121–126].

The swarmalators model, introduced in [82], is defined by the equations

$$\dot{\vec{p}}_i = \vec{\varepsilon}_i + \frac{1}{N}\sum_{j=1}^{N}\left[I_\alpha(\vec{p}_{ji})F(\theta_{ji}) - I_\rho(\vec{p}_{ji})\right],$$

$$\dot{\theta}_i = \omega_i + \frac{1}{N}\sum_{j=1}^{N}H_\alpha(\theta_{ji})G(\vec{p}_{ji}),$$

(B.1)

where $\vec{p}_i$ and θ_i represent the position and the phase of the i-th swarmalator, respectively. Each individual is affected by intrinsic spatial and angular velocities $(\vec{\varepsilon}_i, \omega_i)$, and by the coupling with other individuals, determined by attraction (I_α, H_α), repulsion (I_ρ), and influence (F, G) functions. We use $\vec{p}_{ji}$ and θ_{ji} as compact representations of $(\vec{p}_j - \vec{p}_i)$ and $(\vec{\theta}_j - \vec{\theta}_i)$, respectively. It was shown, in the same work, that computing a two-dimensional (2D) instance of the model would lead to the emergence of several static and active states, each with unique features. Afterwards, various modifications of this 2D model were introduced, analyzing effects produced by an external stimulus [96], chirality of the particles [107], different interactions [97, 98, 127], among others [101, 128–132]. One drawback shared by most of these studies, however, is that despite their numeric findings, analytic results are very limited given the complexity of the model.

The starting point of the work we present here is the one-dimensional (1D) swarmalators model, also denominated "ring model", introduced in [103]. Following the same terminology as in Eqs. (B.1), the 1D model is defined by

$$\dot{x}_i = \frac{1}{N}\sum_{j=1}^{N}I_\alpha(x_{ji})F(\theta_{ji}),$$

$$\dot{\theta}_i = \frac{1}{N}\sum_{j=1}^{N}H_\alpha(\theta_{ji})G(x_{ji}),$$

(B.2)

where attraction and influence functions are chosen to be sines and cosines, respectively, weighted by scalar coupling constants, and $(x_i, \theta_i) \in (\mathbb{S}^1, \mathbb{S}^1)$. Individuals are assumed to be identical, so intrinsic velocities are not considered. Thus, the dynamics of the system are defined by a couple of Kuramoto-like equations. In these, the independent synchronization of positions and phases, promoted by the sines, is strengthened by the interplay induced by the cosines. Given the simplicity in handling periodic functions, this version of the 1D swarmalators model is analytically tractable. Taking advantage of this, several solvable variations have been presented afterwards, with a focus on analyzing the effects generated by nonidentical swarmalators [106], distributed couplings [104], and other factors [84, 105, 133]. One drawback of the 1D swarmalators model in its 'bare' form [Eq. (B.2)] is that its structure prevents the emergence of active states, where $(\dot{x}_i, \dot{\theta}_i \neq 0)$,

in contrast with the 2D instance of Eq. (B.1), where active states emerge even for identical particles. To observe such states in the 1D framework, the solutions found so far involved adding frustration [84], external stimuli [105], considering nonidentical individuals [106], or by splitting the population and mixing coupling signs [133].

Here, we introduce a 2D swarmalators model that shares features with the ones described in Eqs. (B.1) and (B.2), leveraging their advantages and overcoming their drawbacks: the particles are able to move in a 2π-periodic 2D space, and the model is tractable analytically. We show that the model presents several static and active states, some of them similar to ones found in previous studies and some of them new. The active states, moreover, are part of a chaotic regime which, under certain conditions, generates a dimensionality transition.

We outline the general form of our model in Sec. B.3, along with the specific equations used in this work. Next, in Sec. B.4, we present the static and active states that emerge through numerical computations of the model. Upon the intuition gained from the numerical results, in Sec. B.5, we show the main results concerning the stability of the static states. In Sec. B.6, we present the conditions where the system shows chaotic behaviors and the dimensionality transition. In Sec. B.7, we summarize static and active states constructing diagrams showing their stable regions. We conclude this work by discussing our findings and future research suggestions in Sec. B.8.

B.3 The model

We aim to exploit the solvability of the 1D model introduced in [103], in a 2D setup. However, before we describe our generalization, we find it useful to comment on the limitations that arise when trying to recover the dynamics in Eqs. (B.1) from Eqs. (B.2). First, and most evident, the 1D model lacks an explicit repulsive component. This drawback hinders the emergence of states that rely on the different scales of attraction and repulsion forces. For instance, the 1D model cannot generate active states, where the particles keep moving after a transient. Even if an additional position coordinate y_i is considered, defined to be symmetric with x_i, the Kuramoto-like feature, as defined in [103], would lead to the synchronization in each axis, collapsing the system to static analogs of the 1D states. Moreover, the attraction and repulsion functions in Eqs. (B.1) depend on the spatial distances between the particles $\vec{p}_{ji}$. For example, the 2D instance presented in [82] use a power law in p_{ji} as repulsion function, generating collective states where particles distribute radially. Extensions of the ring model to 2D must, therefore, include explicit dependence of repulsive interactions on particle's positions.

For our 2D setup, we define the position of the i-th swarmalator as $\vec{p}_i = (x_i, y_i)$ but use the distances in each axis, x_{ij} and y_{ij}, independently in the dynamical equations,

as using the modulus p_{ij} would undermine the reduction of complexity that we are looking for. The coupling between x and y is done through the phases θ_i, included in the functions F_α and F_ρ that affect attraction I_α and repulsion I_ρ, respectively. The phase dynamics, on the other hand, are defined by their mutual interaction H and by the interplay of both spatial coordinates G. In its general form the model is described by

$$\dot{x}_i = u_i + \frac{1}{N} \sum_{j=1}^{N} \left[I_\alpha(x_{ji}) F_\alpha(\theta_{ji}) - I_\rho(x_{ji}) F_\rho(\theta_{ji}) \right],$$

$$\dot{y}_i = v_i + \frac{1}{N} \sum_{j=1}^{N} \left[I_\alpha(y_{ji}) F_\alpha(\theta_{ji}) - I_\rho(y_{ji}) F_\rho(\theta_{ji}) \right],$$

$$\dot{\theta}_i = \omega_i + \frac{1}{N} \sum_{j=1}^{N} H_\alpha(\theta_{ji}) G(x_{ji}, y_{ji}).$$

For the specific model we study here, we consider that $(x_i, y_i, \theta_i) \in (\mathbb{S}^1, \mathbb{S}^1, \mathbb{S}^1)$, and individuals are assumed to be identical, so $(u_i, v_i, \omega_i) = 0$. Following [103], we choose combinations of sines and cosines for all functions, weighted by coupling constants $J^\pm$ and K'. This makes the problem amenable to analytical treatment, but introduces repulsion in a weak sense:

$$\dot{x}_i = \frac{1}{N} \sum_{j=1}^{N} \left\{ J^- \operatorname{sen}(x_{ji}) \cos(\theta_{ji}) - J^+ \left[1 - \cos(x_{ji}) \right] \operatorname{sen}(\theta_{ji}) \right\},$$

$$\dot{y}_i = \frac{1}{N} \sum_{j=1}^{N} \left\{ J^- \operatorname{sen}(y_{ji}) \cos(\theta_{ji}) - J^+ \left[1 - \cos(y_{ji}) \right] \operatorname{sen}(\theta_{ji}) \right\}, \quad \text{(B.3)}$$

$$\dot{\theta}_i = \frac{K'}{N} \sum_{j=1}^{N} \operatorname{sen}(\theta_{ji}) \left[2 + \cos(2x_{ji}) + \cos(2y_{ji}) \right].$$

In this form, J^- is the weight of the Kurmamoto-like attractive interaction, that is enhanced by phase synchronization. J^+, on the other hand, is the weight of the weak repulsion term, whose sign depends on the difference of phases. It is weak because it disappears when particles are on top of each other, allowing for full synchronization in x, y and θ. When phases are synchronized, $\theta_{ij} = 0$, the equations for x_i and y_i reduce to independent Kuramoto dynamics. Similarly, when $x_{ij} = y_{ij} = 0$, the equation for θ_i follows the Kuramoto model. Repulsion and attraction terms in each direction depend only on the distances in that direction. This is the key feature that allows for simplifications in the analytical treatment while still supporting active states.

As a final step, for an easier understanding of the system, we rewrite $J^\pm = (J_A \pm J_R)/2$ and $K' = K/2$. These new parameters do not alter the structure shown in Eqs. (B.3), but facilitate manipulating attraction and repulsion scales, affected respectively by J_A and

J_R. Thus, the expanded model is given by

$$\dot{x}_i = \frac{1}{N}\sum_{j=1}^{N}\frac{J_A}{2}\left\{\operatorname{sen}(x_{ji})\cos(\theta_{ji}) - \left[1 - \cos(x_{ji})\right]\operatorname{sen}(\theta_{ji})\right\}$$

$$- \frac{J_R}{2}\left\{\operatorname{sen}(x_{ji})\cos(\theta_{ji}) + \left[1 - \cos(x_{ji})\right]\operatorname{sen}(\theta_{ji})\right\},$$

$$\dot{y}_i = \frac{1}{N}\sum_{j=1}^{N}\frac{J_A}{2}\left\{\operatorname{sen}(y_{ji})\cos(\theta_{ji}) - \left[1 - \cos(y_{ji})\right]\operatorname{sen}(\theta_{ji})\right\} \qquad (B.4)$$

$$- \frac{J_R}{2}\left\{\operatorname{sen}(y_{ji})\cos(\theta_{ji}) + \left[1 - \cos(y_{ji})\right]\operatorname{sen}(\theta_{ji})\right\},$$

$$\dot{\theta}_i = \frac{K}{N}\sum_{j=1}^{N}\operatorname{sen}(\theta_{ji})\left\{1 + \frac{1}{2}\left[\cos(2x_{ji}) + \cos(2y_{ji})\right]\right\}.$$

Notice that, in this form, the terms proportional to J_R in the equation for $\dot{x}_i$ include a truly repulsive interaction, $-\operatorname{sen}(x_{ji})$, and half of the weakly repulsive term, $-\left[1 - \cos(x_{ji})\right]$ (and similarly for $\dot{y}_i$). The terms in J_A, however, include the attractive part $\operatorname{sen}(x_{ji})$ but also the other half of the weakly repulsive term. By considering this expanded 2D model, we can derive the original ring model under intuitive convenient conditions (see Appendix B.9.1).

B.4   Numerical results

Simulations performed for the model described in Eqs. (B.4) show the emergence of states that gather features of several states observed in instances of Eqs. (B.1) and (B.2). Additionally, we observe active states that, despite the similarity with states presented in previous works, show interesting properties. All these states are presented in Figs. 14, 15, and 16, where the computations were performed for a population of $N = 500$ swarmalators and different values of J_A, J_R, and K. The particles start positioned uniformly in a 2π-length cube in the (x, y, θ) space, and their states evolve along 10^5 time-steps. From Fig. 14 to Fig. 16, each shows the particles distributed in the (x, y) space colored according to their phases (top rows), and their respective distributions in the (x, y, θ) space (bottom rows).

In Figs. 14(a) and 14(d), we present the point synchronous state, which shows the phase synchronization of particles and their convergence to a fixed point in the (x, y) space. Once these reach a (x_0, y_0, θ_0) state, they remain steady. A similar state emerges on the 1D model [103], where particles converge to a fixed position on the ring. In our model, the emergence of this state requires phase synchronization ($K > 0$), and also ($J_A, J_R > 0$). Moreover, attraction must be stronger than repulsion, $J_A > J_R$, so that particles, which start distributed across the (x, y) space, can collapse to a fixed position. For $J_R > J_A$ the particles converge to the distributed synchronous state shown in Figs. 14(b) and 14(e). In
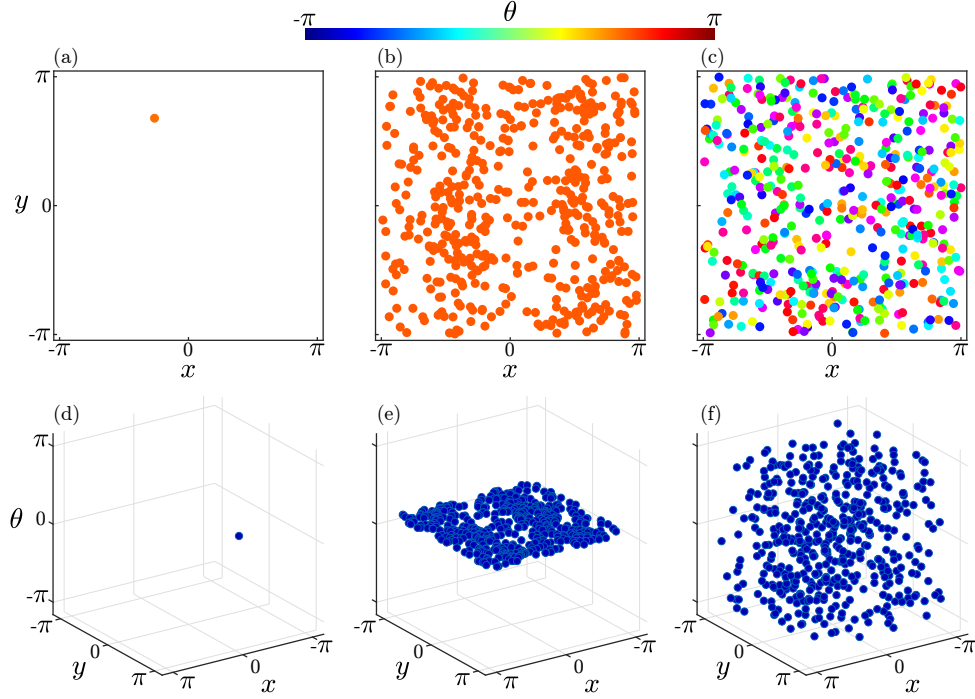
Figure 14 – Snapshots of the [(a),(d)] point synchronous, [(b),(e)] distributed synchronous, and [(c),(f)] distributed asynchronous states after a transient. The panels show the spatial distribution of the particles (top row) and the respective correlation scatter plots (bottom row). The parameters (K, J_A, J_R) are set as $(1, 1, 0.5)$ for the state in [(a), (d)], $(1, 0.5, 1)$ for the state in [(b), (e)], and $(0, -0.5, 0.5)$ for the state in [(c),(f)].

this state, particles synchronize (as $K > 0$) but they remain distributed in the (x, y) space given that now repulsion is stronger than attraction. This state shows a first approach to spatial states generated by instances of Eqs. (B.1), where particles tend to distribute radially [82, 96, 97]. Finally, in Figs. 14(c) and 14(f), we show the distributed asynchronous state. In this, the individuals keep their initial phases frozen ($K = 0$), and the repulsion between them is strong enough to keep the particles distributed uniformly in the (x, y) space. Similar states can also be observed emerging in the 1D model [103, 104], where particles remain asynchronized while distributed along the ring, and in 2D and 3D instances of Eqs. (B.1), where the spatial distribution is radial [82, 97].

Panels in Fig. 15 show three types of static phase wave state. First, Figs. 15(a) and 15(d) show that individuals' positions (x_i, y_i) are positively correlated and that phases θ_i are also positively correlated to these positions. Second, Figs. 15(b) and 15(e) show that individuals' positions (x_i, y_i) are positively correlated but that phases θ_i are negatively correlated to x_i and therefore y_i. Third, Figs. 15(c) and 15(f) show that individuals' positions (x_i, y_i) are negatively correlated and that phases θ_i are positively correlated to x_i only. Each of these states shows similarities with states found in previous work. The static phase wave state in 1D shows the emergence of correlations between particles' positions

	Type of correlation	
State	Positive	Negative
Static phase wave I	x_i, y_i, θ_i	
Static phase wave II	x_i, y_i	x_i, θ_i
Static phase wave III	x_i, θ_i	x_i, y_i

Table 2 – Classification of the static phase wave states according to the type of correlation between individuals' positions and phases.
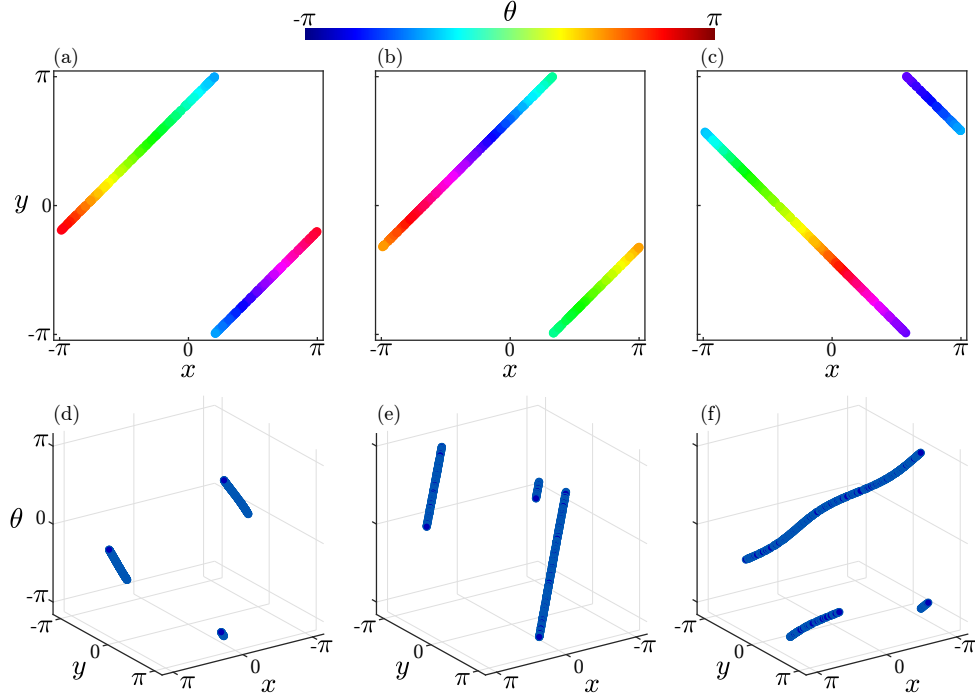

Figure 15 – Snapshots of the static phase wave states after a transient. The panels show the spatial distribution of the particles (top row) and the respective correlation scatter plots (bottom row).[(a), (d)], [(b), (e)], and [(e), (f)] pairs correspond to different types of correlation between x_i, y_i, and θ_i states. The parameters (K, J_A, J_R) are set as $(0, 0, -0.8)$ for the state in [(a), (d)], $(0, 0.8, 0)$ for the state in [(b), (e)], and $(0, 1, -1)$ for the state in [(c),(f)].

and phases [103], and in 2D, the correlation emerges between the polar angle that describes the radial position of each particle and its respective phase [82]. A remarkable feature in our model, furthermore, is that independent of the type of correlation, it features the concept of *'like attracts like'* introduced in [82]: despite individuals' phases being frozen ($K = 0$), they end up grouping in space with similar phases individuals. For simplicity, in the following sections, we will refer to each type of static phase wave state as summarized in Table 2. An additional observation is that, Figs. 15(c) and 15(f) show a small curvature in the correlation, that reminds us of the buckled phase wave state introduced in [103].

In Fig. 16, we show instances of the most noteworthy states of this work: the active ones. We call these 'instances', since all of them are part of a chaotic regime that
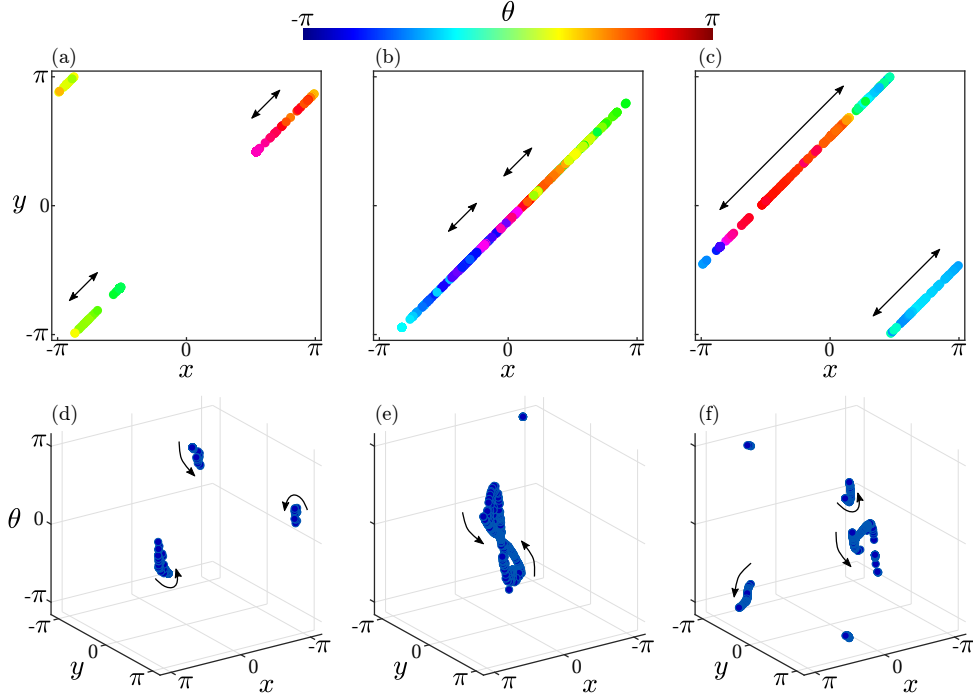
Figure 16 – Snapshots of the [(a),(d)] swirling, [(b),(e)] butterfly, and [(c),(f)] bouncing states after 10^5 time-steps. The panels show the spatial distribution of the particles (top row) and the respective correlation scatter plots (bottom row). The arrows represent the motion of the particles. The parameters (K, J_A, J_R) are set as $(-1, 0, -0.5)$ for the state in [(a), (d)], $(-1, -0.5, -0.5)$ for the state in [(b), (e)], and $(-1, -1, -0.5)$ for the state in [(c),(f)].

we explore in more detail in the following sections. The first one, presented in Figs. 16(a) and 16(d), shows that after a transient, there is an apparent correlation between x_i, y_i, and θ_i, similar to the ones presented for the static phase wave states in Fig. 15. However, individuals move, and despite the positive correlation between x_i and y_i, shown in Fig. 16(a), individuals' positions and phases generate unsteady irregular annular shapes, as noted in Fig. 16(d). These swirls remind us of the ones formed by non-conformist individuals in [133], so we name our state after it. We refer to the second instance of active state, shown in Figs. 16(b) and 16(e), as butterfly state. In this state, particles move while positions x_i and y_i keep linearly correlated. Furthermore, the population of particles continuously alternates between splitting into two clusters and merging back to a single one. Similar to the swirling state, individuals' positions and phases are not correlated. Furthermore, the shape generated by these, as shown in Fig. 16(e), reminds us of the well-known Lorenz attractor projected in 2D. Finally, the bouncing state, depicted in Figs. 16(c) and 16(f), shows similarities with the butterfly state in terms of the correlation between individuals' positions [Fig. 16(c)] and the shapes generated between their positions and phases [Fig. 16(f)]. However, the population of particles goes back and forth, from a single cluster to several ones, in an erratic way. Despite this behavior, the linear correlation between x_i and y_i is preserved.

B.5   Static states

We perform perturbation analyses to study the stability of the static equilibrium states reached by our system. The computations we carry out are based on the analyses presented in [84] for an instance of the 1D model. Then, since the procedures are known, only major considerations and results are presented in the main text and complex calculations are left for the Appendix.

B.5.1   Point synchronous (PS) state

This state is characterized by the convergence of the particles to a point state $x_i = x$, $y_i = y$, and $\theta_i = \theta$, which proves to be a solution of Eqs. (B.3). We add small perturbations δx_i, δy_i, and $\delta \theta_i$ to each particle in their equilibrium state, and find expressions for their time evolution. The perturbation dynamics and their analysis as a linear system are shown in detail in Appendix B.9.2.

The eigenvalues that determine the stability of this state are

$$
\begin{aligned}
\lambda_0^{PS} &= 0, \\
\lambda_1^{PS} &= -2K, \\
\lambda_2^{PS} &= \frac{J_R - J_A}{2},
\end{aligned}
\tag{B.5}
$$

revealing that the PS state emerges only when $K > 0$ and $J_A \geqslant J_R$, as expected from the remarks in the previous section: phase synchronization is driven by $K > 0$ and particles' clustering result from $J_A > J_R$. Moreover, from Eqs. (B.3), we can see that phase synchrony strengthen the attractive effects in spatial dynamics, reason why particles converge to a single point in space instead of cluttering while keeping distance from each other.

B.5.2   Static phase wave (SPW) states

The main feature shared by these states is the linear correlation among x_i, y_i, and θ_i, as classified in Tab. 2. It is easy to check that equilibrium states based on these correlations satisfy the dynamical equations.

In the static phase wave I, the equilibrium state is defined by $x_i = 2\pi i/N + x_0$, $y_i = 2\pi i/N + y_0$, and $\theta_i = 2\pi i/N + \theta_0$. The perturbation analysis performed for this equilibrium is described in Appendix B.9.2.2. The eigenvalues that determine the stability of this state are

$$
\begin{aligned}
\lambda_0^{(I)} &= 0, \\
\lambda_1^{(I)} &= 0.5 J_R, \\
\lambda_2^{(I)} &= 0.5 J_R + 0.25 J_A, \\
\lambda_3^{(I)} &= 0.25 J_R + 0.125 K \\
&\quad \pm 0.5 (0.25 J_R^2 + 0.0625 K^2 - 1.25 J_R K)^{0.5}, \\
\lambda_4^{(I)} &= 0.25 J_R + 0.375 K \\
&\quad \pm 0.5 (0.25 J_R^2 + 0.562 K^2 + 0.75 J_R K \\
&\quad\quad\quad + 0.5 J_A K)^{0.5}.
\end{aligned}
\tag{B.6}
$$

The simplest case to frame, using these eigenvalues, is when $(K = 0)$, which implies that individual phases will remain distributed randomly as in their initial state. Then, the conditions for stability are $J_R \leqslant 0$ and $J_R \leqslant -0.5 J_A$. The negative repulsion and the positive attraction terms indicate a primarily attractive nature of the particles. However, because phases are different, particles cluster with others of similar phases. Additionally, considering $(K > 0)$ would lead to phase synchronization and, consequently, disrupt the clustering behavior among different phases. This behavior is also aligned with our expectation for this state based on the nature of our model. The case where $(K < 0)$ is more complex given that the phase asynchrony is now weighted, incorporating an active ingredient to the system. We explore this active state in the following section.

The static phase wave II is given by $x_i = 2\pi i/N + x_0$, $y_i = 2\pi i/N + y_0$, and $\theta_i = -2\pi i/N + \theta_0$. The details of the perturbation analysis for this equilibrium state are shown in Appendix B.9.2.3. The eigenvalues that determine its stability are

$$
\begin{aligned}
\lambda_0^{(II)} &= 0, \\
\lambda_1^{(II)} &= -0.5 J_A, \\
\lambda_2^{(II)} &= -0.5 J_A - 0.25 J_R, \\
\lambda_3^{(II)} &= -0.25 J_A + 0.125 K \\
&\quad \pm 0.5 (0.25 J_A^2 + 0.0625 K^2 + 1.25 J_A K)^{0.5}, \\
\lambda_4^{(II)} &= -0.25 J_A + 0.375 K \\
&\quad \pm 0.5 (0.25 J_A^2 + 0.562 K^2 - 0.75 J_A K \\
&\quad\quad\quad - 0.5 J_R K)^{0.5}.
\end{aligned}
\tag{B.7}
$$

The conditions for stability are similar to those found in the previous case (static phase wave I): for $K = 0$, we need $J_A \geqslant 0$ and $-J_A \geqslant 0.5 J_R$. Both conditions suggest the attractive nature of the particles, which will lead to the clustering of particles

with similar phases. When $K > 0$, diversity among phases is disrupted, whereas $K < 0$ drives the emergence of active states. The main difference between this state and the previous one lies in the regions of the $(J_A - J_R)$ plane where each state appears, as we will demonstrate in a following section.

Finally, the equilibrium states in the static phase wave III is defined as $x_i = 2\pi i/N + x_0$, $y_i = -2\pi i/N + y_0$, and $\theta_i = 2\pi i/N + \theta_0$. Despite the similarity of these expressions to the equilibria in the two previous cases, the analysis is more complex. The negative correlation between x_i and y_i prevent simplifications in the perturbation analysis. Consequently, finding the eigenvalues that characterize the state's stability becomes more intricate. For details of this analysis, we refer the reader to the Appendix B.9.2.4. Although we do not present the corresponding eigenvalues in the main text, in a following section we will show the stability regions of this state in the $(J_A - J_R)$ plane.

B.5.3 Distributed states

To study the stability of these states we assume a continuum of particles, instead of a discrete set like in the previous cases. We define the fraction of particles lying between x, y, θ and $x + \mathrm{d}x$, $y + \mathrm{d}y$, $\theta + \mathrm{d}\theta$ at time t, by the density $\rho(x, y, \theta, t)\mathrm{d}x\mathrm{d}y\mathrm{d}\theta$. Moreover, ρ will satisfy the normalization condition

$$\int \rho(x, y, \theta)\mathrm{d}x\mathrm{d}y\mathrm{d}\theta = 1 \tag{B.8}$$

where all integrals run from 0 to 2π.

To perform the stability analysis we introduce order parameters of the form

$$S_\sigma e^{\mathrm{i}\phi_\sigma} = \frac{1}{N}\sum_{j=1}^{N} e^{\mathrm{i}\sigma_j}. \tag{B.9}$$

In this expression, σ can represent any individual variable x, y, θ, or a linear combination of these. So, for instance, if we consider $\sigma : \theta$, the order parameter will measure phase coherence, giving $S_\theta = 1$ for a fully synchronized state. Another instance, a bit more interesting is the consideration of $\sigma : (\theta + x)$, which measures the correlation between individuals' positions x_j and phases θ_j. In this case, getting $S_{(\theta+x)} = 1$ is an indicator of a negative correlation between x_i and θ_i as in the static phase wave state II.

In the continuum limit, considering Eq. (B.8), we can rewrite the order parameters as

$$S_\sigma e^{\mathrm{i}\phi_\sigma} = \int_0^{2\pi} e^{\mathrm{i}\sigma}\rho(x, y, \theta)\mathrm{d}x\mathrm{d}y\mathrm{d}\theta, \tag{B.10}$$

so that Eq. (B.3) turns into the mean-field equations

$$
v_x = \frac{J_A}{2} S_{(\theta+x)} \text{sen} \left(\phi_{(\theta+x)} - \theta - x \right) + \frac{J_R}{2} S_{(\theta-x)} \text{sen} \left(\phi_{(\theta-x)} - \theta + x \right) - \frac{J_A + J_R}{2} S_\theta \text{sen} \left(\phi_\theta - \theta \right),
$$

$$
v_y = \frac{J_A}{2} S_{(\theta+y)} \text{sen} \left(\phi_{(\theta+y)} - \theta - y \right) + \frac{J_R}{2} S_{(\theta-y)} \text{sen} \left(\phi_{(\theta-y)} - \theta + y \right) - \frac{J_A + J_R}{2} S_\theta \text{sen} \left(\phi_\theta - \theta \right),
$$

$$
v_\theta = K S_\theta \text{sen} \left(\phi_\theta - \theta \right) + \frac{K}{4} \Big[S_{(\theta+2x)} \text{sen} \left(\phi_{(\theta+2x)} - \theta - 2x \right) + S_{(\theta-2x)} \text{sen} \left(\phi_{(\theta-2x)} - \theta + 2x \right)
$$
$$
+ S_{(\theta+2y)} \text{sen} \left(\phi_{(\theta+2y)} - \theta - 2y \right) + S_{(\theta-2y)} \text{sen} \left(\phi_{(\theta-2y)} - \theta + 2y \right) \Big].
$$
$$
\tag{B.11}
$$

A fully incoherent state, as depicted in the distributed asynchronous case, would be portrayed by the convergence of all the order parameters, in Eqs. (B.11), to zero. However, we can also describe the distributed synchronous state by considering that incoherence happens in space only, letting the system reach phase synchronization ($S_\theta = 1$). For both cases, we define the respective incoherent densities

$$
\rho_0^A = \frac{1}{8\pi^3},
$$
$$
\rho_0^S = \frac{1}{4\pi^2},
$$
$$
\tag{B.12}
$$

which under conditions of the order parameters described above, prove to be equilibrium states of the continuity equation

$$
\frac{\partial \rho}{\partial t} = -\vec{\nabla}(\rho \vec{v}),
\tag{B.13}
$$

where $\vec{v} = (v_x, v_y, v_\theta)$ is the velocity field defined in Eq. (B.11). We perform perturbation analyses for both incoherent states (see Appendix B.9.3). The eigenvalues that determine the stability of the distributed asynchronous state are

$$
\lambda_1^A = \frac{J_A}{16\pi^2},
$$
$$
\lambda_2^A = -\frac{J_R}{16\pi^2},
$$
$$
\lambda_3^A = \frac{K}{8\pi^2},
$$
$$
\lambda_4^A = \frac{K}{32\pi^2},
$$
$$
\tag{B.14}
$$

and, for the distributed synchronous state,

$$
\lambda^S = \frac{J_A - J_R}{8\pi^2},
\tag{B.15}
$$

which additionally requires ($K > 0$) to reach phase coherence.

B.6   Active states

In the previous section, we discussed all the conditions that allow the emergence of the static states. Despite these analytical results, we found only very few hints on the conditions driving the emergence of active states. In order to get more clues on their behavior, we start our analysis by considering distributed states with finite number of particles. Then, we will demonstrate that all the active states shown in Sec. B.4 are actually part of the same chaotic regime.

B.6.1   Active asynchronous state

The analysis of distributed states performed in Sec. B.5.3 relied on the assumption that the number of particles is infinite, so that we could take the continuum limit. This allowed us to consider that all order parameters in Eq. (B.11) would converge asymptotically to zero. However, when dealing with a finite number of particles, this last assumption is not quite true. For $K = 0$, in particular (frozen phases), phase incoherence is not perfect and $S_\theta > 0$. This drawback promotes the appearance of small velocities in $\dot{x}_i$ and $\dot{y}_i$, proportional to $(J_A + J_R)/2$, which ultimately will drive the emergence of an active state. If $J_A = -J_R$, i.e., attraction and repulsion have the same intensity, the state still converges to a static configuration.

B.6.2   Hyperchaos in 3N dimensions

In Sec. B.5 we studied the stability of static states by computing the eigenvalues of the linearized dynamics in scenarios where phases were frozen, $K = 0$, or driven towards synchronization by $K > 0$. Negative phase couplings ($K < 0$), however, not only make computation more complex but also drive the emergence of active states (as shown in Figs. 16).

An interesting feature of these states is that particles are sensitive to small changes in their initial conditions. We highlight this property in Figs. 17(a), 17(b), and 17(c), where trajectories in the x-axis are shown for the same particle in scenarios where $K = -1$. In each of these, we compare the trajectories followed by a single particle when the system starts on the N-dimensional initial states $(\vec{x}_0, \vec{y}_0, \vec{\theta}_0)$ and $(\vec{x}_0 + \delta_x^{(1)}, \vec{y}_0, \vec{\theta}_0)$, where $\delta_x^{(1)} = 10^{-4}$ represents that only the particle of interest's state is perturbed (for instance $x_{1(0)} + \delta_x^{(1)}$). It is clear then that, when considering $(J_A, J_R) = (0.5, -0.5)$ [Fig. 17(a)], the perturbation does not affect the trajectory of the particle considerably. In fact, from Eqs. (B.6), we can infer that these parameters drive the emergence of the static phase wave I. However, once J_A becomes negative [$(J_A, J_R) = (-0.5, -0.5)$ for Fig. 17(b) and $(J_A, J_R) = (-0.5, -3)$ for Fig. 17(c)], the perturbed trajectories suggest the existence of chaos.

In order to explore the presence of chaotic states we compute the maximum Lyapunov exponent as a function of J_A, for $K = -1$ and $J_R = -0.5$. We consider a system of $N = 500$ individuals and take two $3N$-dimensional state trajectories, one with initial conditions $(\vec{x}_0, \vec{y}_0, \vec{\theta}_0)$, and the other one with $(\vec{x}_0 + \delta_x^{(1)}, \vec{y}_0, \vec{\theta}_0)$. We remark that, although $\delta_x^{(1)}$ affects the initial condition of a single particle in the x direction, it perturbs the entire $3N$-dimensional state through the couplings. We then calculate the evolution of the distances $d_{(t)} = d_0 e^{\lambda t}$ between the $3N$-dimensional trajectories and infer the Lyapunov exponents λ from the transitioning slope of $\log[d_{(t)}/d_0]$. These are shown in Fig. 17(d) and, as expected, there is a threshold, at about $J_A = 0.2$, where the system jumps from regular to chaotic (positive Lyapunov exponent). Additionally, from Eqs. (B.6), we can see that $J_A \in [0, 0.2]$, is a region where the static phase wave I state is also stable, meaning that it is a region of bistability between the static phase wave I and the chaotic regime.

State trajectories in the chaotic regime form strange attractors whose structures differ according to the parameters (K, J_A, J_R). Fig. 18 shows a bidimensional projection of the chaotic trajectory followed by a single particle, in the $x - \theta$ torus, in four scenarios. We can see that, depending on the scale difference between attracting (J_A) and repulsing (J_R) terms, the trajectories patterns grow from a small disc [Fig. 18(a)], to butterfly-like [Fig. 18(b)], to a disordered single-loop [Fig. 18(c)], and end-up with a scribble-like structure that covers the whole torus [Fig. 18(d)].

Another interesting phenomenon happens when the scale difference between J_A and J_R surpasses a threshold: the system undergoes a transition of dimensionality. We can see in the insets of Fig. 17(d) that, despite being inside the chaotic regime, when $J_A > -2$, the linear correlation between x_i and y_i is held. However, once J_A gets below this threshold, this correlation breaks. This behavior is strikingly unexpected for our system, given that expressions for $\dot{x}_i$ and $\dot{y}_i$ are symmetric, and even the variations in (J_A, J_R) are the same.

In principle, we might infer that the dimensionality jump is associated with the formation of the scribble-like structure in Fig. 18(d), considering that more dimensions could be required to show a clearer attractor structure. However, this raises an additional question on what is the behavior in the remaining dimensions. A more appropriate analysis to handle this inquiry consists on evaluating more Lyapunov exponents, as we show in Figs. 19 and 20. To compute these, we followed the procedure described in [134], and due to computational limitations, the evaluated system's population was reduced to only $N = 30$ swarmalators. In Fig. 19, we present the behavior of fifteen Lyapunov exponents, out of the ninety that conform the Lyapunov spectrum, when changing J_A for fixed $(K, J_R) = (-1, -0.5)$. As shown, the evolution of the largest Lapunov exponent λ_1 in Fig. 19(a) is consistent with Fig. 17(d), and the points where exponents become positive (pointed out by the respective dashed lines), are positioned around the same place. We
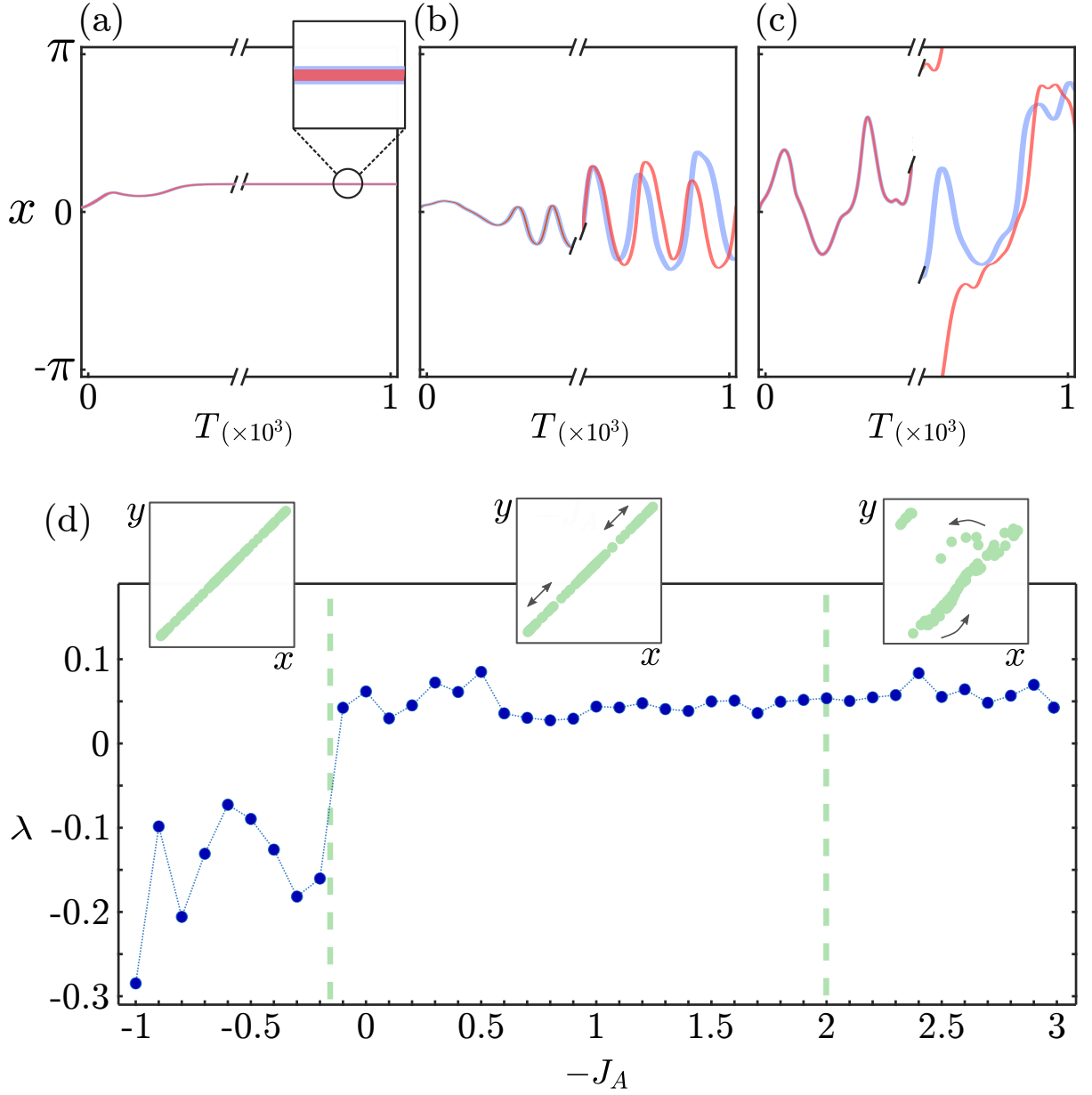
Figure 17 – Temporal behavior of single particle trajectories along the x-axis with non-perturbed (lavender) and perturbed (red) initial conditions (top row), and maximum Lyapunov exponents for different values of J_A (bottom row). Parameters (K, J_R) are set as $(-1, -0.5)$ for all the figures. Trajectories are generated for (a) $J_A = 0.5$, (b) $J_A = -0.5$, and (c) $J_A = -3$. The square in the top corner of (a) shows a magnification of the circled trajectories, and the ones in (d) show correlations in $x - y$ coordinates depending on the values of J_A. The green dashed lines represent the change from static phase wave to chaotic states (left) and the breaking of $x - y$ coordinates correlation (right).
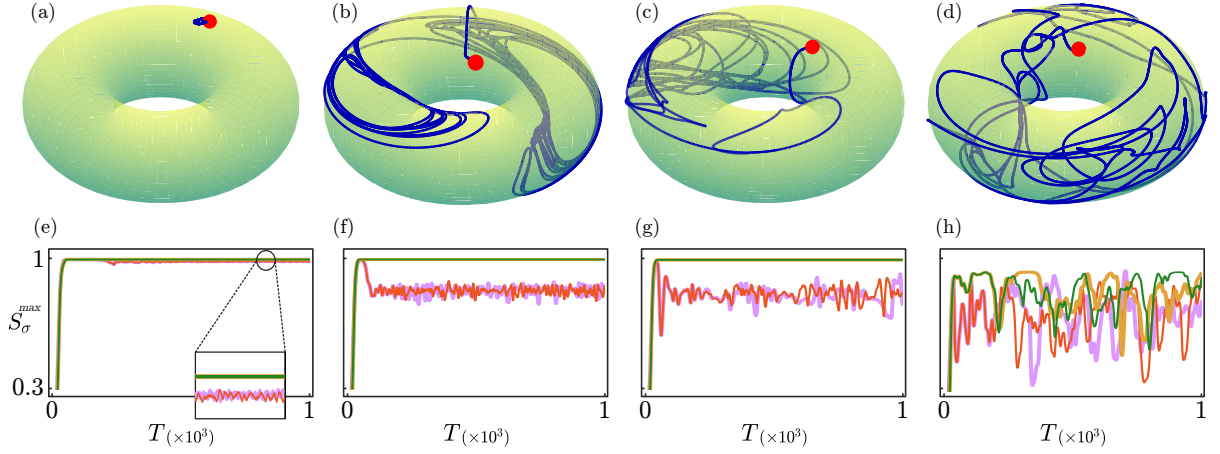
Figure 18 – Top row: trajectories (blue) followed by single particles in the $x - \theta$ torus. The red circles are positioned at the start of each trajectory. Bottom row: evolution of $S_{(\theta\pm x)}^{max}$ and $S_{(x\pm y)}^{max}$ for the original initial conditions (purple and gold, respectively) and the perturbed initial conditions (orange and green, respectively). Parameters (K, J_A, J_R) are set as [(a), (e)] $(-1, 0, -0.5)$, [(b), (f)] $(-1, -0.5, -0.5)$, [(c), (g)] $(-1, -1, -0.5)$, and [(d), (h)] $(-1, -3, -0.5)$. The small rectangle in (a) shows a magnification of the circled lines.

attribute the amplitude differences of these paths to the fact that exponents in the latter figure were calculated by hand after plotting $\log[d_{(t)}/d_0]$. As well, another source of error lies in the nature of the algorithm used to calculate the spectrum, where the precision depends on the computation time. Setting these drawbacks aside, we can see that, in Figs. 19(a), (b), and (c), more than one Lyapunov exponent becomes positive once J_A surpasses the threshold, revealing the hyperchaotic behavior of the system. In addition, in Fig. 20, we present the five largest Lyapunov exponents obtained considering only the spatial dynamics. As expected, exponents are negative while spatial correlation exists, and become positive when correlation is broken. The dashed lines in Figs. 20 and 17(d), pointing out the approximate value of J_A where correlation breaks, are positioned in the same place.

B.6.3 Low-dimensional chaos

The chaotic behavior of the system can also be identified through the correlation functions defined in Sec B.5.3. Specifically, we use the metrics

$$S_{(\theta\pm x)}^{max} = \max\left[S_{(\theta+x)}, S_{(\theta-x)}\right],$$
$$S_{(x\pm y)}^{max} = \max\left[S_{(x+y)}, S_{(x-y)}\right],$$

so we can get a measure of the linear correlation between the respective variables, at any specific time-step, independent on their sign. As shown in the bottom row of Fig. 18, perturbing the initial conditions, generates order parameters that evolve differently. Some of these [Figs. 18(e), (f), (g)] fluctuate around a fixed value, which indicates that we
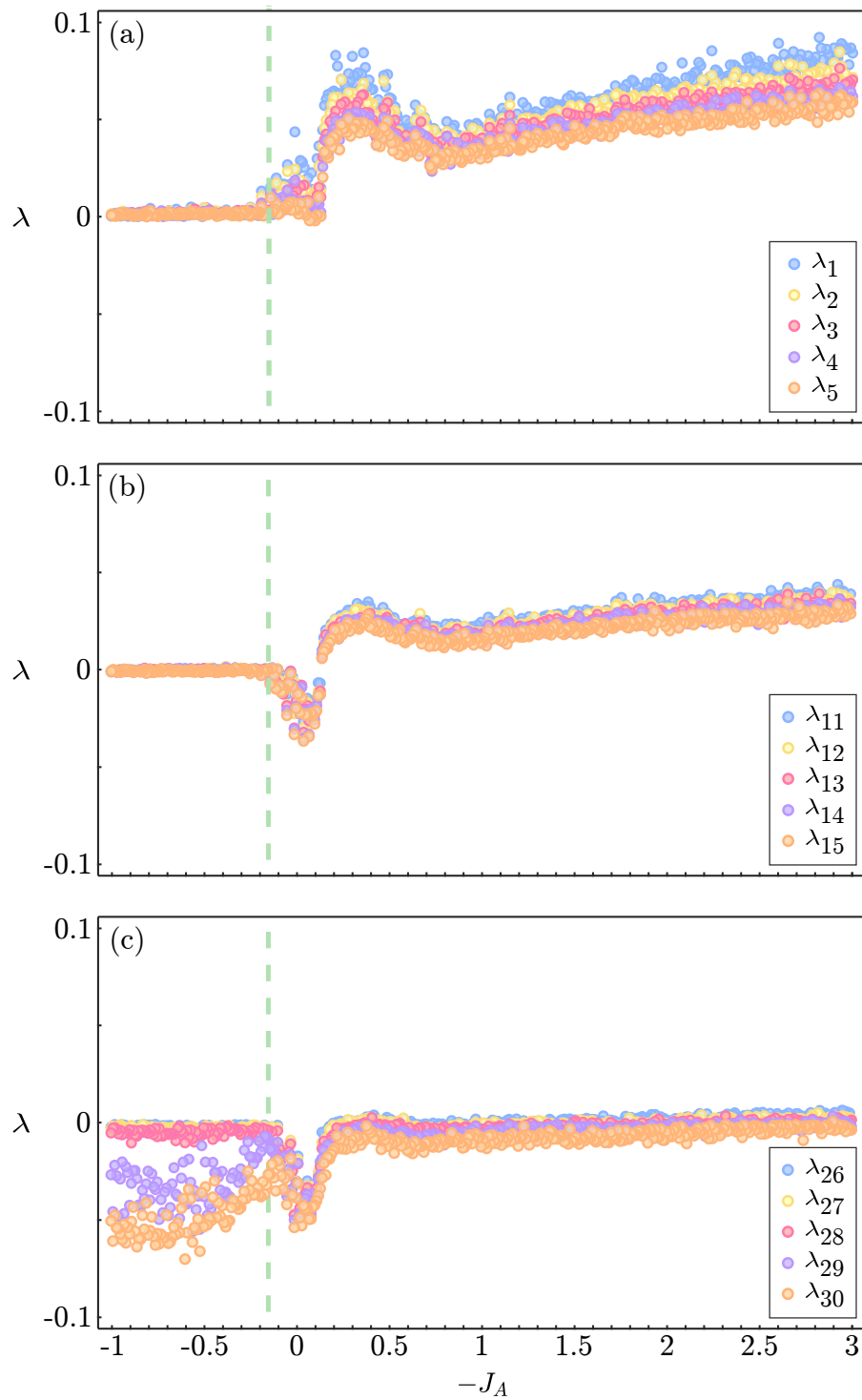
Figure 19 – Evolution of several Lyapunov exponents of the system in function of J_A. The largest exponent is given by λ_1 and the subsequent ones, in terms of amplitude, follow the respective numeration. The panels (a), (b), and (c) display sets of five consecutive exponents within each panel but non-consecutive across panels. The dashed line is positioned close to where at least one exponent becomes significantly positive.
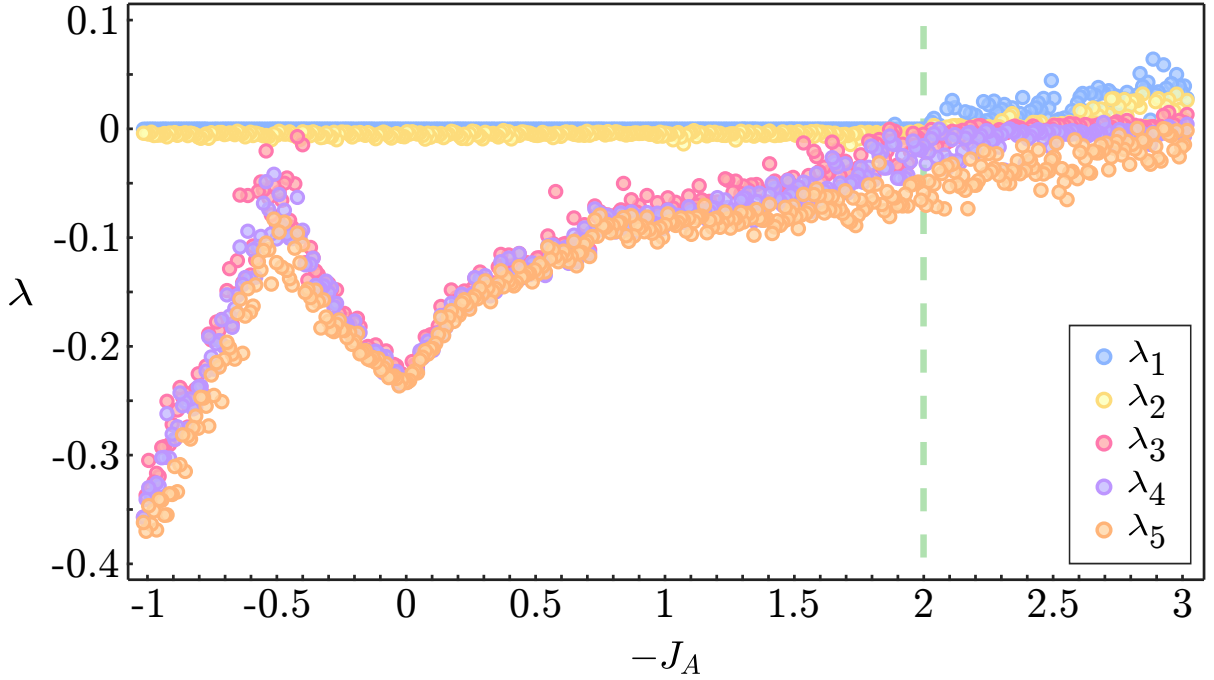
Figure 20 – Evolution of the five largest Lyapunov exponents, estimated considering only position degrees of freedom, in function of J_A. The dashed line is positioned close to where at least one exponent becomes significantly positive.

can use them to discern between states. In Fig. 18(h), however, the fluctuations have a much larger amplitude, hindering any attempt to classify the state based on its value. Additionally, the dimensionality jump is also spotted by $S_{x \pm y}^{max}$, given that it converges to 1 when J_A is over the threshold [Figs. 18(e),(f), and (g)], indicating that x_i and y_i are fully correlated, but it fluctuates once J_A falls below it [Fig. 18(h)].

B.7 Attraction-Repulsion phase diagram

In Fig. 21, we present a summary of the regions where each state emerges in the $J_A - J_R$ plane. These are based on the eigenvalues obtained in Sec. B.5 and the Lyapunov exponents calculated in Sec. B.6.

Note that the active states analyzed in previous sections assumed a positive correlation between x_i, y_i, and θ_i, corresponding to an extension of static phase wave I for $(K < 0)$. We refer to this chaotic regime as Chaos I. Similarly, active effects remain consistent when considering the correlation of static phase wave II, leading us to name that region Chaos II. We can also spot several regions of bistability and multistability. Not only between static states, but also between static and active ones. Remarkably, the regions shown in Fig. 21, consider that initial conditions are distributed randomly in x, y, and θ. Starting in full synchronization ($\theta_i = \theta$) and considering frozen phases ($K = 0$), would lead to the emergence of a synchronous state depending on (J_A, J_R). More exotic
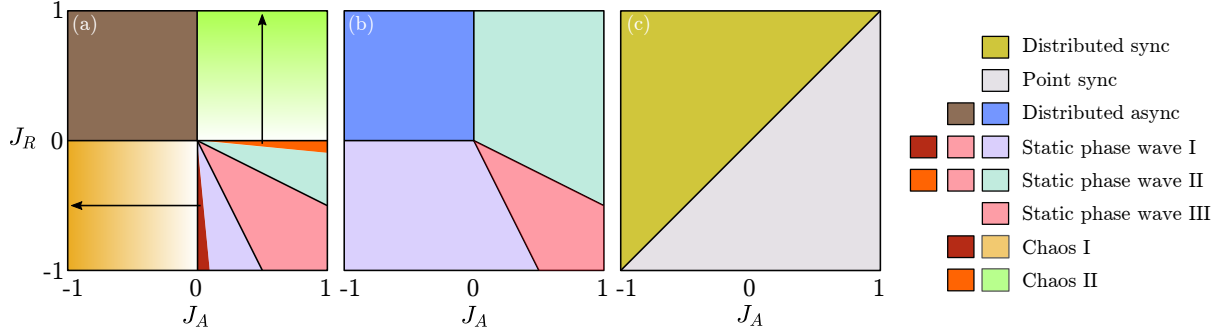
Figure 21 – Regions where states emerge on the $J_A - J_R$ plane for (a) $K < 0$, (b) $K = 0$, and (c) $K > 0$. Arrows and gradients in (a) represent state variations in the chaotic regime, transitioning from swirling to bouncing states. Colors labeling different states are an indicator of multistability.

behaviors, that we do not study here, can be obtained when considering non-random initial conditions.

B.8   Discussion

We have studied a swarmalators system where particles move in the 2D plane with periodic boundary conditions. The model, that generalizes the 1D instance introduced in [103], considers attraction and repulsion terms, which ultimately lead the emergence of distributed and active states, some of them similar to the ones introduced in [82] and [103]. All interaction functions involve only sines and cosines, making stability analysis relatively simple, but leading to a weak form of repulsion. In contrast with previous 2D models, the strength of interactions depends on spatial distances in each direction separately, $x_i - x_j$ and $y_i - y_j$, instead of $\sqrt{(x_i - x_j)^2 + (y_i - y_j)^2}$. That allowed us to obtain analytical conditions for the emergence of all the static states we presented and also analyzed the nature of the active ones.

Two states presented in this work, the distributed synchronous and asynchronous states, closely resemble their counterparts described in [82], the only difference being that, in our findings, particles are not radially distributed. For these, we determined analytically the conditions that drive their emergence considering only control parameters (K, J_A, J_R). Along this line, we have also introduced an active asynchronous state, that emerges under specific conditions for a finite number of particles. Furthermore, we derived the conditions that guarantee the emergence of a point synchronous state, similar to the one introduced in [103] for the 1D model.

We also described static phase wave states that share features with their 1D [103, 104] and 2D counterparts [82]. The main difference with the former is that, in our model, linear correlations show up in three different ways, as classified in Tab. 2. Moreover,

as pointed before for the distributed synchronous and asynchronous states, our model leads to square, instead of radial, symmetry in particle distribution. Despite these differences, the phase wave states share the *'like attracts like'* feature, characteristic of their definition. Our analytical findings allowed us to state all the conditions in (K, J_A, J_R) that drive the emergence of each type of correlation. Strikingly, we found that for $(K \leqslant 0)$ there is a region of multistability in the $J_A - J_R$ plane, where the three types of phase wave state could emerge.

Despite the static states and their counterparts found in previous works, the primary distinction between our model and these lies in the active states, which have remained elusive in 1D simplifications of the original swarmalators model. Previous studies where active states emerged in 1D were based on the inclusion of additional parameters, such as frustration [96], external forcing and pinning [105], or mixed coupling signs [133]. Here we demonstrated that active states can emerge solely by adjusting the model parameters (K, J_A, J_R) when repulsion is included. This is coherent with the original idea of swarmalator systems where unsteady states emerge as a result of scale differences between attractive and repulsive effects. Except for the radial symmetry, the active states we found are similar to the splintered and active phase wave states from [82]. However, after estimating the Lyapunov spectrum, we demonstrated that the active states in our system respond to the emergence of hyperchaos. Just as interestingly, under certain conditions in this regime, the system undergoes a dimensionality transition, where the spatial correlation breaks and particles behave chaotically in x, y, and θ axes.

From a theoretical perspective, our model incorporates intriguing characteristics that may pique curiosity as a dynamical system in its own right. Given the system's dimensionality and its hyperchaotic behavior, we believe it would be worthwhile to delve more deeply into its features. We showed, for example, that the spatial symmetry breaking, responsible for the dimensionality transition, is associated with the appearance of positive Lyapunov exponents when analyzing the spatial dynamics only. However, we have not intensively explored the relation of this phenomena with that of the synchronization of chaos. Another intriguing peculiarity to explore can be observed in Fig. 19(a), where it appears that more than one exponent becomes positive at the same time. It may be also of interest understanding the bifurcations triggered by varying K. In Fig. 21, we have shown three specific cases that allowed us to discern between the states when $(K < 0)$, $(K = 0)$, and $(K > 0)$. However, it may be worthwhile to study in detail the intermediate states of the system as K transitions from being positive-valued to negative-valued and vice versa. This investigation should provide valuable insights into two open questions: why certain states, like the swirling one, have a very long transient before exhibiting their active characteristics, and what mechanisms underlie the emergence of chaos. Regarding the latter question, we also recommend a rigorous study of the routes to chaos and dimensionality breaking when $(K < 0)$. Preliminary numerical studies on this subject have given us

hints of emergent intermittency and crises when examining the evolution of the order parameters for different (J_A, J_R). Finally, it would also be worthwhile to explore whether a threshold on the number of particles N exists, and if so, at what point chaotic behaviors are triggered.

Our model merges two lines of research on the same topic: 1D systems based on the ring model and 2D modifications of the original model. Therefore, its adaptation to previous work on these two lines can occur smoothly. For instance, future work could take our model as a base to consider chirality [107], different phase interactions [97, 98, 127], finite cutoff ranges [99], clusters with different attractive and repulsive strengths [132], or short range repulsive interactions [100]. Then, given the structure of our model, finding analytical solutions on each of these modifications would be less challenging than doing it for instances of the 2D model introduced in [82].

Given that the interactions in our model are based on Kuramoto-like terms, modifications performed in the Kuramoto model could also be adapted to ours [86]. A particularly interesting take would be to consider frustration, given that the addition of lag parameters are responsible for the emergence of a turbulent-like state in the ring model [84], and also drive the formation of interesting spatial patterns in swarming only systems [108, 135]. Furthermore, the inclusion of external stimulus discussed in previous work, implies affecting the dynamics in a periodic nature [105] and mainly in the phase dynamics [96, 136]. One suggestion would be to consider external stimuli in space, mimicking a shear, as has been done for bacterial suspensions [137]. It would also be of interest considering finite cutoff interaction distances between individuals [99] so that different concentrations of individuals can be managed, emulating the study on vinegar eels in [138]. If a collective of swarmalators works as a medium, it would also be worth studying how it is affected by external particles and vice versa, similar to the study in [123] for nematodes. Additionally, we could explore changing the mobility space of the swarmalators, for instance, by imposing discontinuities in the (x, y) space, or also considering self-propulsion of the particles in the direction of their phases, as presented in [139].

States emerging in our model could also fit collective swarming-only behaviors if we consider that their three spatial degrees of freedom interplay. A clear example of this approach is depicted by the behavior of swarming mosquitoes [140, 141], which shows similarities with the active asynchronous state in a spherical description. For this setup, we consider switching the model variables such that θ_i determines the radial distances, and (x_i, y_i), the azimuthal and polar angles, respectively. The resulting state shows clustered individuals in the middle of a cloud of loosely behaved ones, coherent with a description given in [140]. We also expect the chaotic states, shown in Fig. 18, to be useful in the study of populations that exhibit this type of behaviors. Finally, our model could be considered as a basis for engineered systems, similar to the ones presented in [142–144].

B.9   Appendix B1

B.9.1   Derivation of the ring model

We can collapse the 2D system to a single dimension in space by considering $\dot{x}_i = \dot{y}_i$. Hence, we get rid of the second expression in Eqs. (B.4). Additionally, if we assume that there is no scale difference between attraction and repulsion, and that individuals are purely attracting (i.e. $J = J_A = -J_R$, for $J_A > 0$), the equations governing the system's dynamics become

$$\dot{x}_i = \frac{J}{N} \sum_{j=1}^{N} \text{sen}(x_{ji}) \cos(\theta_{ji}),$$

$$\dot{\theta}_i = \frac{K}{N} \sum_{j=1}^{N} \text{sen}(\theta_{ji}) \left[\cos(x_{ji}) \right]^2.$$

Notice that, without loss of generality, we have neglected the scaling factor in the phase dynamics ($2K \to K$). This 1D system fits with the structure described in Eqs. (B.2), and, the only difference with the 1D model introduced in [103] is the squared cosine in the phase dynamics. This variation ultimately improves the driving towards synchronous or asynchronous states (depending on the value of K), as the influence of the individuals' positions will always be null or positive.

B.9.2   Perturbation analysis of coherent states

For each state described below, we will be able to rearrange the respective perturbation dynamics as

$$\dot{\delta \vec{r}_i} = \mathbf{R} \delta \vec{r}_i, \tag{B.16}$$

where $\delta \vec{r}_i = (\delta x_i, \delta y_i, \delta \theta_i)$ and

$$\mathbf{R} = \begin{pmatrix} \mathbf{R_1} & \mathbf{R_2} & \mathbf{R_3} \\ \mathbf{R_4} & \mathbf{R_5} & \mathbf{R_6} \\ \mathbf{R_7} & \mathbf{R_8} & \mathbf{R_9} \end{pmatrix} \tag{B.17}$$

is a $3N \times 3N$ block matrix where each $N \times N$ block is circulant. Thus, the stability of Eq. (B.16) can be analyzed by finding the eigenvalues of $\mathbf{R}$.

We follow the usual procedure to solve an eigenvalue problem, which starts by defining $\mathbf{R_*} = \mathbf{R} - \vec{\lambda} \mathbf{I}_{3N \times 3N}$ and then concludes by finding the eigenvalues $\vec{\lambda}$ from the determinant of $\mathbf{R_*}$. Thus, considering that $\mathbf{R_*}$ is also a block matrix, we can rewrite its determinant as

$$\det(\mathbf{R_*}) = \det(\mathbf{M}),$$

where

$$\mathbf{M} = \mathbf{R_1^*}(\mathbf{R_5^* R_9^*} - \mathbf{R_6 R_8}) - \mathbf{R_2}\left(\mathbf{R_4 R_9^*} - \mathbf{R_6 R_7}\right)$$
$$+ \mathbf{R_3}\left(\mathbf{R_4 R_8} - \mathbf{R_5^* R_7}\right),$$

since blocks commute, and

$$\mathbf{R_1^*} = \mathbf{R_1} - \vec{\lambda}_1 \mathbf{I}_N,$$
$$\mathbf{R_5^*} = \mathbf{R_5} - \vec{\lambda}_5 \mathbf{I}_N,$$
$$\mathbf{R_9^*} = \mathbf{R_9} - \vec{\lambda}_9 \mathbf{I}_N.$$

Given that blocks composing $\mathbf{R}$ are circulant, the $N \times N$ matrix $\mathbf{M}$ will also be circulant. Then, we can use the general solution to find the determinant of circulant matrices as

$$\det\left(\mathbf{M}\right) = \prod_{k=0}^{N-1} \sum_{r=0}^{N-1} M_{r+1} \zeta^{kr}, \tag{B.18}$$

from where we are able to obtain the eigenvalues $\vec{\lambda}$. The term $\zeta = \exp\left\{2\pi \mathrm{i}/N\right\}$ is a primitive N-root of unity. Notice that the structure of $\mathbf{M}$ follows that of $\mathbf{R}$ in Eq. (B.17) (i.e. elements' sub-indexes represent the same position in the matrix).

B.9.2.1   Point Synchronous

We add small individual perturbation to the equilibrium states as

$$x_i = x + \delta x_i$$
$$y_i = x + \delta y_i$$
$$\theta_i = x + \delta \theta_i.$$

By plugging these into Eq. (B.4), we find the perturbation dynamics, governed by

$$\delta \dot{x}_i = \frac{J_A - J_R}{2N} \sum_{j=1}^{N} (\delta x_j - \delta x_i),$$

$$\delta \dot{y}_i = \frac{J_A - J_R}{2N} \sum_{j=1}^{N} (\delta y_j - \delta y_i),$$

$$\delta \dot{\theta}_i = \frac{2K}{N} \sum_{j=1}^{N} (\delta \theta_j - \delta \theta_i),$$

which can be arranged as the linear system shown in Eq. (B.16). In this particular case, we have that $\{\mathbf{R_2}, \mathbf{R_3}, \mathbf{R_4}, \mathbf{R_6}, \mathbf{R_7}, \mathbf{R_8}\} = \mathbf{0}$ and $\mathbf{R_1} = \mathbf{R_5}$, which simplifies the eigenvalue problem considerably. Finally, using Eq. (B.18), we obtain the eigenvalues shown in Eqs. (B.5).

B.9.2.2 Static phase wave I

In this case, the perturbed equilibrium states are defined as

$$x_i = \frac{2\pi \mathrm{i}}{N} + x_0 + \delta x_i,$$

$$y_i = \frac{2\pi \mathrm{i}}{N} + y_0 + \delta y_i,$$

$$\theta_i = \frac{2\pi \mathrm{i}}{N} + \theta_0 + \delta\theta_i,$$

and the perturbation dynamics are governed by

$$
\begin{aligned}
\delta\dot{x}_i &= \frac{1}{2N} \sum_j \left[\delta x_j F_a^{(I)}(i,j) + \delta\theta_j F_b^{(I)}(i,j) \right] \\
&\quad + \frac{J_R}{2} (\delta x_i - \delta\theta_i), \\
\delta\dot{y}_i &= \frac{1}{2N} \sum_j \left[\delta y_j F_a^{(I)}(i,j) + \delta\theta_j F_b^{(I)}(i,j) \right] \\
&\quad + \frac{J_R}{2} (\delta y_i - \delta\theta_i), \\
\delta\dot{\theta}_i &= \frac{K}{2N} \sum_j \left[\delta x_j F_c^{(I)}(i,j) + \delta y_j F_c^{(I)}(i,j) \right. \\
&\quad \left. + \delta\theta_j F_d^{(I)}(i,j) \right],
\end{aligned}
\tag{B.19}
$$

where

$$F_a^{(I)}(i,j) = J_A \cos\left(\frac{4\pi}{N}(j-i) \right) - J_R,$$

$$
\begin{aligned}
F_b^{(I)}(i,j) &= J_R + J_A \cos\left(\frac{4\pi}{N}(j-i) \right) \\
&\quad - (J_A + J_R) \cos\left(\frac{2\pi}{N}(j-i) \right),
\end{aligned}
$$

$$F_c^{(I)}(i,j) = \cos\left(\frac{6\pi}{N}(j-i) \right) - \cos\left(\frac{2\pi}{N}(j-i) \right),$$

$$F_d^{(I)}(i,j) = \cos\left(\frac{6\pi}{N}(j-i) \right) + 3\cos\left(\frac{2\pi}{N}(j-i) \right).$$

The positive correlation between x_i and y_i, in the equilibrium, generates a clear symmetry in position dynamics. Then, as noticed, the coefficients $F_a^{(I)}(i,j)$ and $F_b^{(I)}(i,j)$ repeat in the expressions defining $\delta\dot{x}_i$ and $\delta\dot{y}_i$, and $F_c^{(I)}(i,j)$ shows up twice in the definition of $\delta\dot{\theta}_i$. These features allow for the simplification of the linear system when structuring it as in Eq. (B.16). Thus, for this case we have that $\mathbf{R_1} = \mathbf{R_5}$, $\mathbf{R_3} = \mathbf{R_6}$, $\mathbf{R_7} = \mathbf{R_8}$, and $\{\mathbf{R_2}, \mathbf{R_4}\} = \mathbf{0}$. These considerations allow us to split the eigenvalue problem into two problems of lower dimensions such that

$$\mathbf{M}^{(I)} = \mathbf{R_1^*}\left(\mathbf{R_1^* R_9^*} - 2\mathbf{R_3 R_7} \right).$$

Then, using Eq. (B.18), we have that

$$\det(\mathbf{R_1^*}) = \prod_{k=0}^{N-1} \left\{ -\lambda + \frac{J_R}{2} + \frac{1}{2N} \sum_{j=1}^{N} \zeta^{(j-1)k} F_a^{(I)}(1,j) \right\},$$

$$\det\left(\mathbf{R_1^* R_9^*} - 2\mathbf{R_3 R_7}\right) = \prod_{k=0}^{N-1} \left\{ \lambda^2 - \lambda \left[\frac{J_R}{2} + \frac{1}{2N} \sum_{j=1}^{N} \zeta^{(j-1)k} \left[F_a^{(I)}(1,j) + K F_d^{(I)}(1,j) \right] \right] \right.$$

$$+ \frac{K}{2N} \sum_{j=1}^{N} \zeta^{(j-1)k} [J_R F_c^{(I)}(1,j) + \frac{J_R}{2} F_d^{(I)}(1,j) - \frac{J_A + J_R}{2}$$

$$\left. \cos\left(\frac{2\pi}{N}(j-1) \right)] \right\},$$

whose solution allows us to find the eigenvalues presented in Eqs. (B.6).

B.9.2.3 Static phase wave II

The only difference between this state and the previous one, in the equilibrium, is that the correlation between x_i and θ_i is now negative. Then, after perturbing the equilibrium states individually, we have that

$$x_i = \frac{2\pi i}{N} + x_0 + \delta x_i,$$

$$y_i = \frac{2\pi i}{N} + y_0 + \delta y_i,$$

$$\theta_i = -\frac{2\pi i}{N} + \theta_0 + \delta \theta_i,$$

and the perturbation dynamics are governed by

$$\delta \dot{x}_i = \frac{1}{2N} \sum_j \left[\delta x_j F_a^{(II)}(i,j) + \delta \theta_j F_b^{(II)}(i,j) \right]$$

$$- \frac{J_A}{2} (\delta x_i + \delta \theta_i),$$

$$\delta \dot{y}_i = \frac{1}{2N} \sum_j \left[\delta y_j F_a^{(II)}(i,j) + \delta \theta_j F_b^{(II)}(i,j) \right]$$

$$- \frac{J_A}{2} (\delta y_i + \delta \theta_i),$$

$$\delta \dot{\theta}_i = \frac{K}{2N} \sum_j \left[\delta x_j F_c^{(II)}(i,j) + \delta y_j F_c^{(II)}(i,j) \right.$$

$$\left. + \delta \theta_j F_d^{(II)}(i,j) \right],$$

where

$$F_a^{(II)}(i,j) = J_A - J_R \cos\left(\frac{4\pi}{N}(j-i)\right),$$

$$F_b^{(II)}(i,j) = J_A + J_R \cos\left(\frac{4\pi}{N}(j-i)\right)$$
$$- (J_A + J_R)\cos\left(\frac{2\pi}{N}(j-i)\right),$$

$$F_c^{(II)}(i,j) = \cos\left(\frac{2\pi}{N}(j-i)\right) - \cos\left(\frac{6\pi}{N}(j-i)\right),$$

$$F_d^{(II)}(i,j) = 3\cos\left(\frac{2\pi}{N}(j-i)\right) + \cos\left(\frac{6\pi}{N}(j-i)\right).$$

Notice that these equations also show the recurrence of some coefficients in the definition of $\delta\dot{x}_i$, $\delta\dot{y}_i$, and $\delta\dot{\theta}_i$. This consideration leads to the same simplifications described for the previous state when structuring the system as in Eqs. (B.16). So we have that, $\mathbf{R_1} = \mathbf{R_5}$, $\mathbf{R_3} = \mathbf{R_6}$, $\mathbf{R_7} = \mathbf{R_8}$, and $\{\mathbf{R_2}, \mathbf{R_4}\} = \mathbf{0}$.

$$\mathbf{M}^{(II)} = \mathbf{R_1^*}\left(\mathbf{R_1^*R_9^*} - 2\mathbf{R_3R_7}\right).$$

$$\det(\mathbf{R_1^*}) = \prod_{k=0}^{N-1}\left\{-\lambda - \frac{J_A}{2} + \frac{1}{2N}\sum_{j=1}^{N}\zeta^{(j-1)k}F_a^{(II)}(1,j)\right\},$$

$$\det\left(\mathbf{R_1^*R_9^*} - 2\mathbf{R_3R_7}\right) = \prod_{k=0}^{N-1}\left\{\lambda^2 - \lambda\left[-\frac{J_A}{2} + \frac{1}{2N}\sum_{j=1}^{N}\zeta^{(j-1)k}\left(KF_d^{(II)}(1,j) + F_a^{(II)}(1,j)\right)\right]\right.$$

$$+ \frac{K}{2N}\sum_{j=1}^{N}\zeta^{(j-1)k}[J_AF_c^{(II)}(1,j) - \frac{J_A}{2}F_d^{(II)}(1,j) + \frac{(J_A + J_R)}{2}$$

$$\left.\cos\left(\frac{2\pi}{N}(j-1)\right)]\right\},$$

which lead to the eigenvalues presented in Eqs. (B.7).

B.9.2.4 Static phase wave III

For this case, the perturbed equilibrium states are defined as

$$x_i = \frac{2\pi i}{N} + x_0 + \delta x_i,$$

$$y_i = -\frac{2\pi i}{N} + y_0 + \delta y_i,$$

$$\theta_i = \frac{2\pi i}{N} + \theta_0 + \delta\theta_i,$$

and the perturbation dynamics are governed by

$$\delta \dot{x}_i = \frac{1}{2N} \sum_j \left[\delta x_j F_a^{(III)}(i,j) + \delta \theta_j F_b^{(III)}(i,j) \right]$$

$$+ \frac{J_R}{2}(\delta x_i - \delta \theta_i),$$

$$\delta \dot{y}_i = \frac{1}{2N} \sum_j \left[\delta y_j F_c^{(III)}(i,j) + \delta \theta_j F_d^{(III)}(i,j) \right]$$

$$- \frac{J_A}{2}(\delta y_i + \delta \theta_i),$$

$$\delta \dot{\theta}_i = \frac{1}{2N} \sum_j \left[\delta x_j F_e^{(III)}(i,j) - \delta y_j F_e^{(III)}(i,j) \right.$$

$$\left. + \delta \theta_j F_f^{(III)}(i,j) \right],$$

where

$$F_a^{(III)}(i,j) = J_A \cos \left(\frac{4\pi}{N}(j-i) \right) - J_R,$$

$$F_b^{(III)}(i,j) = J_R + J_A \cos \left(\frac{4\pi}{N}(j-i) \right) - (J_A + J_R) \cos \left(\frac{2\pi}{N}(j-i) \right),$$

$$F_c^{(III)}(i,j) = J_A - J_R \cos \left(\frac{4\pi}{N}(j-i) \right),$$

$$F_d^{(III)}(i,j) = J_A + J_R \cos \left(\frac{4\pi}{N}(j-i) \right) - (J_A + J_R) \cos \left(\frac{2\pi}{N}(j-i) \right),$$

$$F_e^{(III)}(i,j) = K \cos \left(\frac{6\pi}{N}(j-i) \right) - K \cos \left(\frac{2\pi}{N}(j-i) \right),$$

$$F_f^{(III)}(i,j) = 3K \cos \left(\frac{2\pi}{N}(j-i) \right) + K \cos \left(\frac{6\pi}{N}(j-i) \right).$$

Despite the slight difference in the definition of equilibrium states compared to the previous cases (types I and II), simplifications are not possible in the perturbation equations of motion. As noticed, the only repeating coefficient is $F_e^{(III)}(i,j)$ in the definition of $\delta \dot{\theta}_i$. Hence, when structuring the perturbation dynamics as in Eqs. (B.16), the only consideration we can make is that $\mathbf{R_7} = -\mathbf{R_8}$. This drawback forces us to write the determinant, using Eq. (B.18), as

$$\det(\mathbf{M}^{(III)}) = \prod_{k=0}^{N-1} \left\{ -\lambda^3 + \lambda^2 \left[\frac{J_R - J_A}{2} + \frac{1}{2N} S_1 \right] + \lambda \left[\frac{J_A J_R}{4} + \frac{J_A J_R}{4N} T_1 + \frac{J_A}{4N} S_2 - \frac{J_R}{4N} S_3 \right] \right.$$

$$\left. + \frac{K}{16N} (J_A + J_R)^2 - \frac{J_A J_R}{8N} S_4 \right\},$$

where

$$S_1 = \sum_{j=1}^{N} \zeta^{(j-1)k} \left(F_a^{(III)}(1,j) + F_c^{(III)}(1,j) + K F_f^{(III)}(1,j) \right),$$

$$S_2 = \sum_{j=1}^{N} \zeta^{(j-1)k} \left(F_a^{(III)}(1,j) + KF_e^{(III)}(1,j) + KF_f^{(III)}(1,j) \right),$$

$$S_3 = \sum_{j=1}^{N} \zeta^{(j-1)k} \left(F_c^{(III)}(1,j) + KF_e^{(III)}(1,j) + KF_f^{(III)}(1,j) \right),$$

$$S_4 = \sum_{j=1}^{N} \zeta^{(j-1)k} \left(2F_e^{(III)}(1,j) + F_f^{(III)}(1,j) \right),$$

$$T_1 = \sum_{j=1}^{N} \zeta^{(j-1)k} + 0.25 \left(\zeta^{(j-1)(k+2)} + \zeta^{(j-1)(k-2)} \right),$$

$$T_2 = 0.5 \sum_{j=1}^{k} \zeta^{(j-1)(k+1)} + \zeta^{(j-1)(k-1)}.$$

To find the eigenvalues, we must address N cubic equations of the form $-\lambda^3 + \lambda^2\beta + \lambda\xi + \eta$. We solve these using the general formula for

$$\beta = \begin{cases} 0, & \text{for } k = 0; \\ 0.5(J_R - J_A) + 1.5K, & \text{for } k = 1, N-1; \\ 0.25(J_R - J_A), & \text{for } k = 2, N-2; \\ 0.5(J_R - J_A) + 0.25K, & \text{for } k = 3, N-3; \\ 0.5(J_R - J_A), & \text{otherwise}; \end{cases} \qquad \text{(B.20)}$$

$$\xi = \begin{cases} 0, & \text{for } k = 0, \\ 0.25(J_A J_R + K(J_A - J_R)), & \text{for } k = 1, N-1; \\ 0.125(J_A^2 + J_R^2 + 2.5 J_A J_R), & \text{for } k = 2, N-2; \\ 0.25(J_A J_R + K(J_A - J_R)), & \text{for } k = 3, N-3; \\ 0.25 K J_A J_R, & \text{otherwise}; \end{cases} \qquad \text{(B.21)}$$

and

$$\eta = \begin{cases} 0, & \text{for } k = 0; \\ 0.125K[0.25(J_A + J_R)^2 \\ \quad - J_A J_R], & \text{for } k = 1, N-1; \\ 0, & \text{for } k = 2, N-2; \\ -0.1875 K J_A J_R, & \text{for } k = 3, N-3; \\ 0, & \text{otherwise}. \end{cases}$$

B.9.3   Perturbation analysis of incoherent states

In general, we perturb the equilibrium state ρ_0 by a small quantity $\delta\rho$, such that $\rho = \rho_0 + \delta\rho$. Then, the temporal evolution of the perturbation is governed by

$$\frac{\partial}{\partial t}\delta\rho = -\vec{\nabla}(\delta\rho)\vec{v}. \tag{B.22}$$

From Eq. (B.8), we know that

$$\int_0^{2\pi} \delta\rho(x,y,\theta,t)\mathrm{d}x\mathrm{d}y\mathrm{d}\theta = 0,$$

and to first order in $\delta\rho(x,\theta,t)$, we have that

$$S_\sigma^1 e^{\mathrm{i}\phi_\sigma} = \int_0^{2\pi} e^{\mathrm{i}\sigma}\delta\rho(x,y,\theta,t)\mathrm{d}x\mathrm{d}y\mathrm{d}\theta. \tag{B.23}$$

We expand $\delta\rho$ in Fourier series as

$$\delta\rho = \sum_{m,n,l} f_{m,n,l}(t)e^{\mathrm{i}(mx+ny+l\theta)}, \tag{B.24}$$

and we will solve equations of the type $f(t) = \bar{f}e^{\lambda t}$ to get the eigenvalues λ.

B.9.3.1   Distributed asynchronous

We consider the equilibrium ρ_0^A defined in Eqs. (B.12). Using Eqs. (B.22) and (B.23), we obtain the perturbation dynamics

$$
\begin{aligned}
\frac{d}{dt}\delta\rho = {} & \frac{J_A}{16\pi^3}\left[S_{(\theta+x)}^1\cos\left(\phi_{(\theta+x)} - \theta - x\right) + S_{(\theta+y)}^1\cos\left(\phi_{(\theta+y)} - \theta - y\right)\right] \\
& - \frac{J_R}{16\pi^3}\left[S_{(\theta-x)}^1\cos\left(\phi_{(\theta-x)} - \theta + x\right) + S_{(\theta-y)}^1\cos\left(\phi_{(\theta-y)} - \theta + y\right)\right] \\
& + \frac{K}{32\pi^3}\left[S_{(\theta+2x)}^1\cos\left(\phi_{(\theta+2x)} - \theta - 2x\right) + S_{(\theta-2x)}^1\cos\left(\phi_{(\theta-2x)} - \theta + 2x\right)\right. \\
& \qquad + S_{(\theta+2y)}^1\cos\left(\phi_{(\theta+2y)} - \theta - 2y\right) + S_{(\theta-2y)}^1\cos\left(\phi_{(\theta-2y)} - \theta + 2y\right) \\
& \qquad \left. + 4S_\theta^1\cos\left(\phi_\theta - \theta\right)\right].
\end{aligned}
\tag{B.25}
$$

We expand this equation following the form of Eq. (B.24) and we will see that the only relevant terms correspond to

$$
\begin{aligned}
\{(m,n,l)\} = {} & \{(-1,0,1);(0,-1,-1);(1,0,-1); \\
& (0,1,-1);(0,0,-1);(2,0,-1); \\
& (-2,0,-1);(0,2,-1);(0,-2,-1)\}.
\end{aligned}
\tag{B.26}
$$

Then, the solutions give us the eigenvalues shown in Eqs. (B.14).

B.9.3.2   Distributed synchronous

Given that in this state phases are synchronized and only positions are uniformly distributed, we uncouple the system's dynamics. The incoherence between phases and positions will lead to zeroing order parameters $S_{(\theta \pm 2x)}$ and $S_{(\theta \pm 2y)}$. That allows us to rewrite

$$v_\theta = K S_\theta \text{sen}(\phi_\theta - \theta),$$

which is exactly the mean-field description of the Kuramoto model without considering natural frequencies [21]. Then, the condition to reach synchronization is given by $(K > 0)$.

In the equilibrium, the synchronization of phases will lead to $\theta_i = \theta$. This condition allows for the equivalences

$$S_{(\theta \pm x)} e^{i\phi(\theta \pm x)} = S_x e^{i(\theta \pm \phi_x)},$$
$$S_{(\theta \pm y)} e^{i\phi(\theta \pm y)} = S_y e^{i(\theta \pm \phi_y)},$$

and therefore, the velocity field for this state is defined as

$$
\begin{aligned}
v_x &= \frac{J_A - J_R}{2} S_x \text{sen}\left(\phi_x - x\right), \\
v_y &= \frac{J_A - J_R}{2} S_y \text{sen}\left(\phi_y - y\right).
\end{aligned}
\tag{B.27}
$$

In this case we use the equilibrium ρ_0^S from Eqs. (B.12), and considering (B.23), the perturbation dynamics are governed by

$$\frac{d}{dt}\delta\rho = \frac{J_A - J_R}{8\pi^2}\left[S_x^1 \cos\left(\phi_x - x\right) + S_y^1 \cos\left(\phi_y - y\right)\right]. \tag{B.28}$$

Then, using Eq. (B.24) for this equation, we find the eigenvalue shown in Eq. (B.15).